



Politecnico di Torino

Corso di Laurea Magistrale in Ingegneria Energetica e Nucleare

TESI DI LAUREA

Target fragmentation in Hadrontherapy

Candidata:
Federica Gargano

Relatori:
Gianni Coppa
(Dipartimento di Elettronica e Telecomunicazioni)
Giuseppe Battistoni
(INFN-Sezione di Milano)

Anno Accademico 2017–2018

Oggi non è che un giorno qualunque di tutti i giorni che verranno. Ma quello che accadrà in tutti gli altri giorni che verranno può dipendere da quello che farai oggi.
— E. Hemingway (*Per chi suona la campana*)

Contents

| | |
|--|-----------|
| Introduction | i |
| 1 Medical application of ionizing radiation | 1 |
| 1.1 Introduction to Hadrontherapy | 1 |
| 1.2 Interaction of radiation with matter | 3 |
| 1.2.1 Photons Interactions | 3 |
| 1.2.2 Charged Particles Interaction Mechanisms | 4 |
| 1.2.3 Ionization and excitation: Stopping Power and Bragg Peak | 5 |
| 1.2.4 Particle Range and Stragglng | 8 |
| 1.2.5 Multiple Coulomb Scattering: Lateral Beam Spread | 10 |
| 1.2.6 Nuclear Interactions: the role of fragmentation | 11 |
| 1.3 Biological effects of radiation | 14 |
| 1.4 Biological and dosimetric parameters | 15 |
| 1.4.1 Absorbed dose | 15 |
| 1.4.2 Linear Energy Transfer, LET | 15 |
| 1.4.3 Relative Biological Effectiveness, RBE | 16 |
| 1.4.4 Oxygen Enhancement Ratio, OER | 17 |
| 1.5 Hadrontherapy technology | 18 |
| 1.5.1 Cyclotron and Synchrotron | 19 |
| 1.5.2 Beam Delivery | 20 |
| 1.6 Treatment Planning | 21 |
| 1.7 Future prospects | 22 |
| 2 The FOOT experiment | 25 |
| 2.1 Target fragmentation in proton therapy | 26 |
| 2.2 Projectile fragmentation in heavy ion therapy | 26 |
| 2.3 Experimental strategies | 27 |
| 2.4 The design criteria of FOOT apparatus | 27 |
| 2.5 The Electronic Detector Setup | 28 |
| 2.5.1 Pre-Target region | 29 |
| 2.5.2 Magnetic spectrometer region | 30 |
| 2.5.3 Scintillator and Calorimeter region | 30 |
| 2.6 Microstrip Silicon Detector | 31 |
| 2.6.1 Advantages in using semiconductors | 31 |
| 2.6.2 Signal formation and acquisition | 32 |
| 2.6.3 The ideal semiconductor detector: Signal-to-Noise Ratio | 33 |
| 2.6.4 Strip detectors: configuration and working principle | 36 |
| 2.6.5 The Microstrip Silicon Detector for FOOT | 37 |
| 2.7 Test Beam in Trento | 38 |
| 3 Simulation and reconstruction software | 45 |
| 3.1 FLUKA Monte Carlo simulation code | 45 |
| 3.2 FLUKA input | 46 |
| 3.3 FLUKA combinatorial geometry | 47 |

| | | |
|----------|--|-----------|
| 3.4 | Event Reconstruction | 49 |
| 4 | Simulation results | 51 |
| 4.1 | Microstrip Detector configurations | 51 |
| 4.2 | Energy loss analysis | 52 |
| 4.3 | Multiple Scattering analysis | 56 |
| 4.4 | Fragmentation analysis | 60 |
| | Bibliography | 67 |
| | Ringraziamenti | 71 |

Introduction

Following cardiovascular diseases, cancer is the major leading cause of mortality in the world, according to estimates given by the World Health Organization (WHO). Although surgery is considered the standard approach for the cure of solid tumors, most of cancer patients receive support treatments to surgical removal. One option, especially when dealing with localized tumors, is the radiotherapy, most of the time performed with photon or electron beams. In recent years, the development of new technologies and the evolution in radiation oncology techniques has led to the establishment of an alternative therapy, known as *Hadrontherapy* or *Charged Particle Therapy* (CPT), which make use of protons and fully ionized atomic nuclei that are subjected to strong nuclear forces (*hadrons*, from the Greek: *hadrós*=strong). Hadrontherapy shows many advantages with respect to the traditional radiotherapy, related to the peculiar energy loss mechanism that characterizes the interaction of protons and other ions with the matter. Indeed, when traversing tissues, these particles release a low dose at the beginning of their path, depositing almost all their energy at the end of the path, in correspondence of the so called Bragg Peak. This property allows to treat deep seated tumors with an higher precision with respect to the traditional radiotherapy, minimizing collateral effects on surrounding healthy tissues and organs at risk. A further advantage derived from the use of charged particles in radiotherapy, in particular in the case of ions with $Z>1$, is due to their enhanced biological effectiveness with respect to photons, which results in an higher capability of producing direct damages to the DNA of tumor cells, considerably increasing cell killing efficiency.

Clinical results obtained with hadrontherapy have been extremely positive for various types of tumor, with percentages of local tumor control equivalent or better than for conventional radiotherapy. Most clinical data obtained with charged particles are related to the proton therapy, but the use of carbon ions has demonstrated to be of great interest in the last decade. These results, accompanied by the new performances in accelerator technology and calculation systems of the delivered doses, have determined over the past years an increased interest for the development of hadrontherapy, with the construction of new centres provided with equipment entirely dedicated to clinical activity. Although protons and carbon ions are the most largely used particles, the interest is now being focused also on other type of ions, in order to optimize the clinical potential of CPT. Growing interest is dedicated to a possible use of light ions, such as Helium, in light of its improved lateral dose distribution compared with protons and due to its cost/benefit ratio of implementation more affordable if compared to carbon ions. For what concerns heavier ions, the Oxygen appears to be a good candidate against deep seated hypoxic tumors.

When using heavier ions, projectile fragmentation events occur inside the patient tissues. The projectile fragments are produced mostly in the forward direction with the same velocity, but lower mass, of the primary particle, resulting in a longer range than the projectile and therefore in an unwanted dose tail beyond

the Bragg peak. Recently it has been suggested that also in proton therapy, the nuclear inelastic interactions of the incident beam with the patient tissues might lead to the fragmentation of the target nuclei producing a non negligible amount of target fragments in the entry region, *i.e.* outside the planned treatment volume. Different studies have shown that such fragments have small ranges (of the order of μm), resulting in a local dose deposition. This effect could modify the expectations of low damage to healthy tissues. Notwithstanding the effectiveness of hadrontherapy and its increasing use in cancer treatment worldwide, there is a lack of experimental measurements of nuclear fragmentation cross sections, especially in the energy range of therapeutic applications (50-250 MeV for proton and 50-400 MeV/u for carbon ions). Only few experiments have been dedicated to the study of projectile fragmentation for carbon ions. These data are required to improve the algorithms currently used in the Treatment Planning Systems (TPS) for proton and heavy ion therapy. The measurements of the protons nuclear cross section is of particular interest since recent studies have shown a possible underestimation or overestimation of the proton biological effectiveness assumed in the current TPS.

The FOOT (FragmentatiOn Of Target) experiment aims to fill this gap, performing a set of measurements of nuclear fragmentation cross sections for proton and heavy ion therapy. Further interest in such measurements comes also from the issue of radioprotection in space missions. Indeed, there is a common ground between protecting astronauts from the effects of space radiation exposure and providing ions therapy: the particles species currently available in the hadrontherapy (protons and Carbon) or considered as alternatives (Helium, Oxygen) are among the most abundant in space. This will allow the interchange of cross sections data. For this purpose a dedicated experimental apparatus has been conceived. It consists of a high precision tracking system in a magnetic field, a time of flight measurement system and a calorimeter. The primary beam monitoring is accomplished by means of a plastic scintillator detector that measures the incoming rate of the ion beam and a drift chamber that measures the incident beam direction and position. The whole experimental setup will allow to measure the momentum, kinetic energy and time of flight of the fragments produced in the interaction between the incident beam and a specific target. Some components have been already produced and tested, while the configuration of the others is still under investigation. In order to find the optimal geometry, a series of simulations are performed by means of the FLUKA Monte Carlo code, developed by a INFN-CERN collaboration.

The aim of the present thesis is to analyse the performances of one of the tracking detectors of the experimental setup: Microstrip Silicon Detector, whose area is equal to $9\times 9\text{ cm}^2$. The use of this kind of detector is a recent modification of the first design of the experimental setup, that goes back to June 2017. The choice has been dictated by the need to provide a sufficient spatial resolution, minimizing the amount of material in order to reduce the impact of multiple scattering and secondary fragmentations. Also the redundant energy loss measurement provided by this detector could be useful to improve the reliability of the experiment. Considering the recent idea of introducing this type of detector in the FOOT experimental setup, there are not enough available data to estimate its performances. It is therefore necessary to rely upon simulations, in order to find which could be the best configuration that allow to reach the expected results. For this purpose different geometrical configurations have been analysed and compared. Particular interest has been posed to multiple scattering and secondary fragmentation events, that could affect the correct track reconstruction. Furthermore,

the positive contribution in energy loss measurements has been proven. The work described in this thesis will give some preliminary results on the strip detector performances, allowing to optimize its design and to find the optimal configuration that satisfies the requirements of the experiment.

This thesis is divided in four chapters. In Chapter 1, the basics of radiation interaction with matter will be introduced, followed by a description of the relevant radiobiological parameters for particle therapy and by an overview of the current adopted technologies in hadrontherapy. In Chapter 2 experimental strategies and the FOOT experimental setup will be shown, focusing on the MSD and on the advantages in using semiconductor detectors. The software used in the FOOT experiment for simulations and data reconstruction are briefly described in Chapter 3. Finally, in Chapter 4 the details of the different analysed configurations of such detector and the obtained results will be shown, followed by the presentation of the performances of a strip detector used during a test beam carried out on December 2017 in the Trento Proton Therapy Centre (Italy).

Chapter 1

Medical application of ionizing radiation

1.1 Introduction to Hadrontherapy

In medicine, ionizing radiation is used to provide information about the functioning of specific organs (diagnosis) or to treat diseases and tumors (therapy). Radiation therapy plays an important role in the treatment of cancer pathologies, after surgery it is the most frequently applied form of therapy. When treating patients, different clinical approaches can be also combined simultaneously, in order to increase the chance of success: for example chemotherapy can be used to treat tumors with which radiation can't deal alone. Unfortunately, the treatments are not always successful. The main reason for these failures is the difficulty to a local control of the tumor, especially when tumor is localized close to organs at risk.

In radiotherapy the key problem is to irradiate the whole target volume in order to kill all cancer cells, minimizing the dose deliver to the surrounding healthy tissues. For therapy using photons as incident particles, this cannot be achieved because the dose deposition is spread out over all the particle trajectories. As shown in Fig.1.1, which shows the dose deposition induced by different projectiles with respect to the penetration depth in liquid water, the maximum of the deposition for X -rays is located at a small penetration depth. It is therefore difficult to accurately treat tumors deeply located in the body while preserving simultaneously the surrounding tissues. Nowadays, radiation therapy exploits the use of mega-volt photons. The dose profile for such photons is characterized by an initial dose buildup with respect conventional X -rays, mainly caused by forward scattered Compton electrons, that shifts the peak dose by a few centimeters away from the surface of the patient's body, thereby improving the target-to-entrance dose [16].

During last decades much progress has been made to improve the dose delivery towards the ideal situation and to thereby increase the tumor cure rate. *Intensity Modulated Radio Therapy* (IMRT) is one of the most important recent developments in radiation therapy. It is a technology that exploits the use of multiple beams of X -rays of varying intensity directed towards the cancer, angled from various directions around the patient. Therefore, it is possible to concentrate the delivered dose on the tumor volume [2]. These achievements would not have been possible without the interdisciplinary collaboration of scientists in the fields of oncology and radiation medicine as well as accelerator technology and engineering.

As soon as particle accelerators were available, the charged particle therapy has been tested. Robert R. Wilson was the first to investigate the depth-dose

characteristics of proton beams [15]. In 1954, at Lawrence Berkeley Laboratory, first patient treatments with protons started. The use of other ions, such as carbon, has spread out only very recently. The leading country in the world is Japan, where the first treatment center in Chiba was build in 1994. At the same time, new technical solutions were developed at GSI in Germany: the built of an active beam scanning, as shown in Section 1.5.2, resulted in the achievement of a high degree of conformation [16]. Nowadays, the hadrontherapy is widely spread all around the world and more than 100000 patients have already taken advantage of its benefits.

Hadrons present different advantages for the treatment of deep-seated local tumors in comparison to conventional radiotherapy, deriving from their physical behavior when penetrating tissues. As shown in Fig.1.1, the depth-dose profile distributions of protons and carbon ions are characterized by a small entrance dose and a distinct narrow peak near the end of their path, the so called *Bragg Peak*. This allows to maximize the destruction of cancerous cells while minimizing collateral effects on healthy tissues, increasing the probability of success when treating tumors located near to organs at risk [2],[7],[4].

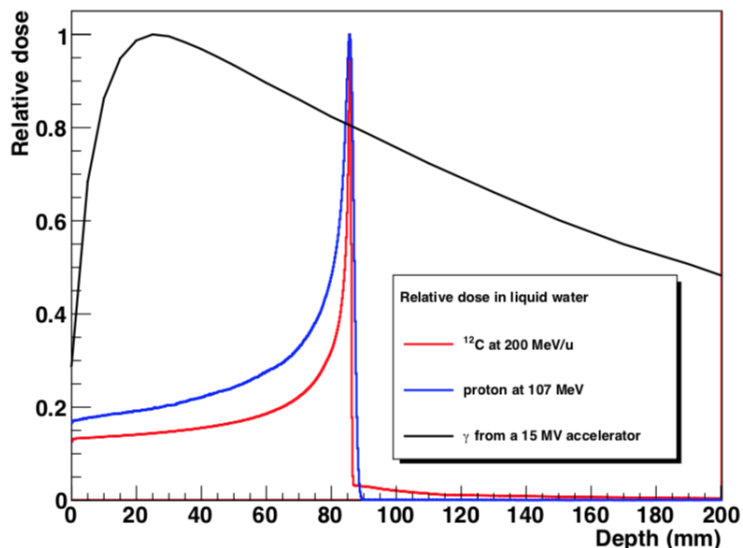


Figure 1.1: Depth-dose profiles for different particles in water [2].

In general the aim of cancer therapy is to deliver enough radiation to the tumor to destroy it without irradiating normal tissues with a dose that will lead to serious complications. As shown in Fig.1.2, the principle is usually illustrated by plotting two curves: the Tumor Control Probability (TCP), that represents the local tumor control when a certain dose is delivered, and the Normal Tissue Complication Probability (NTCP), that, on the other hand, gives info on normal tissue injury under the same conditions.

The aim of radiation therapy is to maximize the TCP and simultaneously minimizes the NTCP: it is easier to achieve the therapeutic goal if the TCP and the NTCP are well separated. As TCP and NTCP increase with the dose there is a dose range, the so called *therapeutic windows*, where the probability of controlling the tumor without complications reaches a maximum. Biological models in oncological therapy aim to predict these TCP and NTCP values to optimize the treatment for each patient [14],[18].

The rationale to use hadrons for radiotherapy is precisely to achieve this goal, delivering the dose on the target volume with a much better localization and biological efficiency with respect to the conventional therapy.

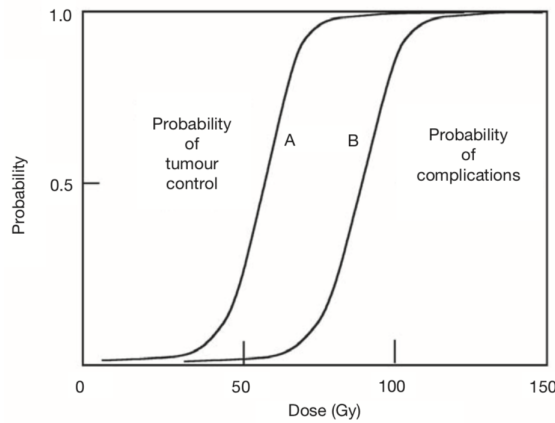


Figure 1.2: The principle of therapeutic ratio. Curve A represents the Tumor Control Probability (TCP) and curve B the Normal Tissues Complication Probability (NTCP) [14].

Before the definition of all the quantities and physical processes relevant for such therapy, it is important to understand how radiation interacts with the matter. In Section 1.2 the interaction mechanisms for different type of particles are therefore analysed, giving a short overview on photons interaction and then focusing on charged particles. To better understand the benefits deriving from the use of hadrons, the biological effects of radiations are described in Section 1.3, followed by the introduction of biological and dosimetric quantities of interest. In Section 1.5, a brief description of current adopted technologies for hadrontherapy follows, showing how, from the source, the beam arrives to treatment rooms. Finally, in the last two Sections, the methodologies adopted for treatment plans conception are introduced, focusing on the open issues and highlighting in this sense the goals that the FOOT experiment aims to reach.

1.2 Interaction of radiation with matter

Particles emitted from a source with a certain energy interact with the environment into which they are released in different ways. Depending on the particle type and energy, as well as on the medium properties, some processes dominate, other do not occur, defining in this way the characteristic properties of the propagation and the detection of a specific particle as well as its biological effects. The study of these interaction mechanisms constitutes the guideline for the improvement of many science fields: from the design of radiation detection systems to the optimization of radiation shielding materials, as well as the implementation of new radiation techniques for tumor treatments [10],[12].

In the following, the main physical processes deriving from interactions that are relevant for therapeutic applications are described.

1.2.1 Photons Interactions

Photons interact with either orbital electrons or nuclei in passing through matter. In general three main effects can be observed when photons traverse a medium (Fig.1.3):

- Photoelectric Effect
- Compton Effect
- Pair Production

The first effect takes place when the photon energy is comparable to the binding energy of the electrons in the outer shell of the atoms composing the traversed medium. The energy of the incident photon is completely absorbed by the orbital electron, which is ejected from its atom of origin. The incident photon thus completely disappears and all of its energy is carried off by the photoelectron. This one can ionize and excite other atoms until all of its energy is dissipated. When a photon of higher energy interacts with an orbital electron losing only part of its initial energy we speak about Compton scattering : the photon scatters off the orbital electron and a new photon of lower energy appears, traveling in a new direction. Finally, if the photon energy exceeds 1022 keV, it can interact with an atomic nucleus and being converted in a electron-positron pair [10].

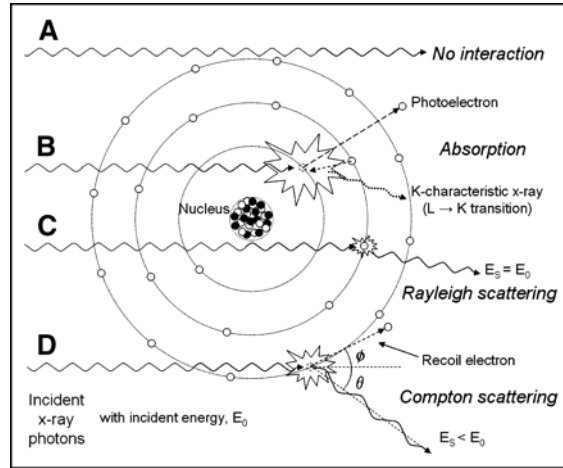


Figure 1.3: Fig.(a) Illustrative summary of X-ray and γ -ray interactions: (A) Primary, unattenuated beam does not interact with material. (B) Photoelectric effect : the incident photon releases all of its energy to the photoelectron. (C) Rayleigh scattering is an interaction with electrons (or whole atom) in which no energy is exchanged and incident X-ray energy equals scattered X-ray energy with small angular change in direction.(D) Compton scattering interaction: the new photon travels with an energy E_s lower than that one of the incident radiation [17].

The predominance of a certain interaction mechanism with respect to the others depends on the energy of the incident photon as well as on the atomic number of the traversed medium. In Fig.1.4 contributions to the photon cross section in carbon is shown.

1.2.2 Charged Particles Interaction Mechanisms

Charged particles interact with matter primarily through the Coulomb forces between their positive charge and the negative charge of the orbital electrons of the atoms composing the traversed medium. Although interactions with nuclei occur only rarely, they play a crucial role in the optimization of charged particle therapy, as will be presented in this Section. In the following the primary ways through which charged particles interact with matter are listed:

- Ionization and excitation
- Multiple Coulomb scattering
- Bremsstrahlung Radiation
- Cherenkov Radiation
- Nuclear interactions

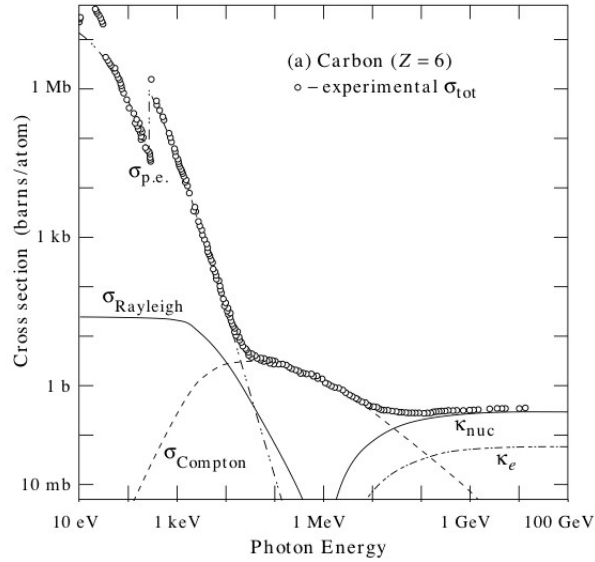


Figure 1.4: Photon total cross section as a function of energy in carbon target, showing the contribution of different processes: $\sigma_{p.e.}$ =photoelectric effect, $\sigma_{Compton}$ =Compton scattering, k_{nuc} =pair production(nuclear field), k_e =pair production(electron field). At low energies the photoelectric effect dominates. With increasing energy the Compton scattering also becomes relevant, while for values larger than 1 MeV it starts becoming less probable if compared to pair production phenomena [25].

In this thesis we will not discuss in detail Bremsstrahlung and Cherenkov Radiation, since their effects are not relevant for therapeutic applications, for a more complete treatment of these topics the reader should refer to specialized texts.

1.2.3 Ionization and excitation: Stopping Power and Bragg Peak

In the ionization phenomena, the incident charged particle loses its energy removing an outer shell electron from an atom of the medium, creating an *ion pair*. The ion will attract a free electron from somewhere in the medium and return to its neutral state.

Excitation is due to the motion of an electron from its original orbit into an higher energy state as a result of an absorption of energy coming from the charged particle. This electron may eventually fall back to its original state with the emission of a photon whose frequency is proportional to the difference in energy between the two orbits. The key parameter is the average energy loss per unit length, known as *Stopping Power*, where E indicates the incident particle energy and x is the traveled distance from such particle in the medium.

In 1913, Niels Bohr derived an explicit formula for the stopping power, calculating the energy loss of a heavy ¹ charged particle in a collision with a target electron of the material [19]:

$$-\frac{dE}{dx} = \frac{4\pi z^2 e^4}{m_e v^2} Z N_0 \ln \left(\frac{\gamma^2 m_e v^3}{z e^2 w} \right) \quad (1.1)$$

where m_e is the electron mass, z is the charge number of the incident particle, w is the orbital frequency, $Z N_0$ is the electron density and is equal to $Z N_A \rho / A$, with ρ , Z , A respectively the density, atomic and mass number of the medium and N_A the Avogadro number. The term $\gamma = (\sqrt{1 - \beta^2})^{-1}$ is the Lorentz factor, in which β is the ratio between the particle velocity and the speed of light in vacuum.

¹A charged particle of rest mass significantly larger than that of an electron is considered to be a "heavy" charged particle [20]

This evaluation of the stopping power well describes the behavior of heavier charged particles at not too high speed [19], while shows some limitations when dealing with lighter nuclei at larger speed. Indeed, at higher projectile velocities, the projectile behaves quantum mechanically, or wave-like. Equation (1.1) can be rewritten in a form that follows Hans Bethe's and Felix Bloch's derivation using quantum perturbation theory [25]:

$$-\frac{dE}{dx} = K\rho z^2 \frac{Z}{A} \frac{1}{\beta^2} \left[\frac{1}{2} \ln \frac{2m_e c^2 \beta^2 \gamma^2 W_{max}}{I^2} - \beta^2 - \frac{\delta(\beta\gamma)}{2} - \frac{C}{Z} \right] \quad (1.2)$$

where $K = 4\pi N_A r_e^2 m_e c^2$, r_e is the classical electron radius, ρ is the density of the medium, I the mean excitation energy of the medium, W_{max} is the maximum kinetic energy which can be imparted to a free electron in a single collision, $\delta(\beta\gamma)$ is the density effect correction and C/Z is the shell correction. The introduction of the density correction factor takes into account the reduction of the stopping power due to the polarization of the medium caused by the electric field originated by the incident charged particle. In Fig.1.5 is shown how the stopping power behavior changes when density correction is not applied. The shell correction, instead, arises for low energies of the incident particles, to correct for atomic binding neglected in calculating some of contributions in Eq.(1.2). At very low energies ($E < 10$ keV/u) the so called *Barkas-effect* has to be taken into account, introducing the Z_{eff} factor as a function of β and Z of the incident particle [2]:

$$Z_{eff} = Z \left[1 - \exp \left(-125\beta Z^2/3 \right) \right] \quad (1.3)$$

This parameter highlights that projectiles of opposite charge lose energy at different rates while traversing matter [23].

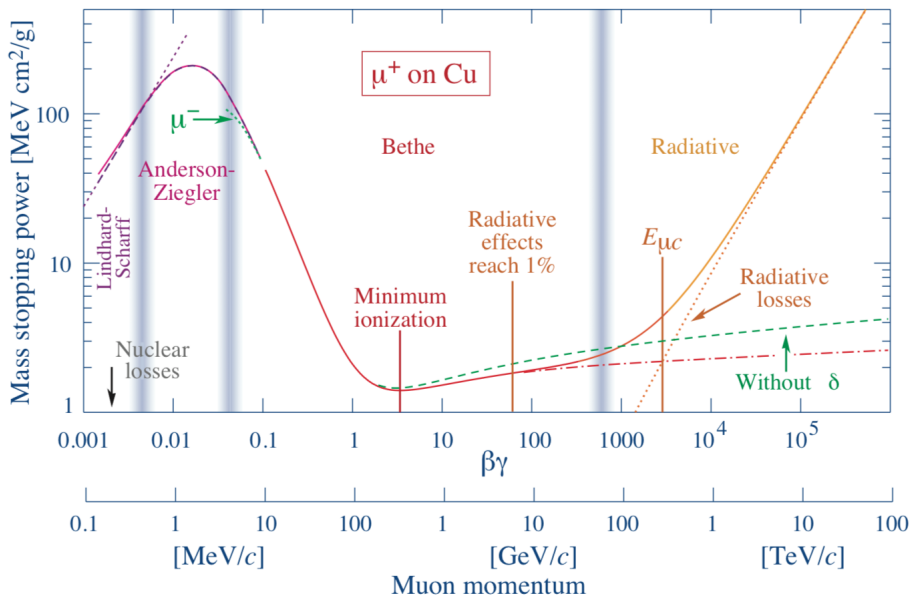


Figure 1.5: Example of stopping power as a function of $\beta\gamma$. Vertical bands indicate different approximations discussed in this Section. The short green dotted line on the left of the graph represents the Barkas effect (the correction decreases very rapidly with increasing energy). On the right one can see the difference of the Bethe-Bloch equation when density correction factor is introduced (red dashed line) [25].

Under these conditions, Eq.(1.2) describes the mean rate of energy loss in the region $0.1 < \beta\gamma < 1000$ for intermediate- Z materials. At the lower limit the projectile velocity becomes comparable to atomic electron velocity and at the upper limit radiative effects begin to be important (Fig.1.5). In general the Eq.(1.2) shows

an energy loss proportional to $1/\beta^2$ at low energies, until a minimum is reached. After this minimum, for $\beta\gamma > 1$ (see Fig.1.5) a logarithmic rise follows [25]. Energy loss as a function of the penetration depth describes the Bragg Curve: due to the energy loss along the path, the projectile slows down and, remembering the $1/\beta^2$ dependence, the largest amount of energy is therefore deposited near the end of the track, as shown in Fig.1.6.

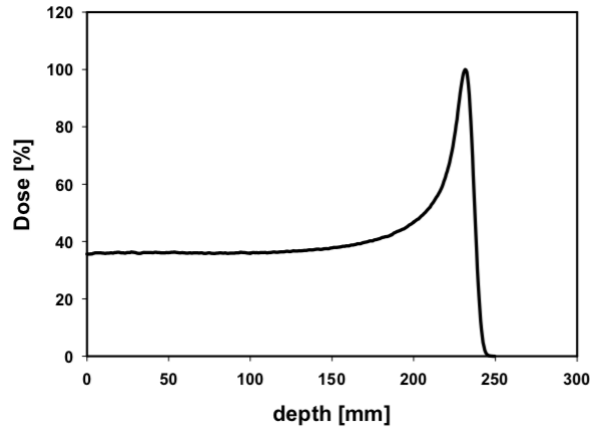


Figure 1.6: Typical depth-dose profile for protons [8].

Because of this behavior, protons and heavier charged particle beams provide a sought-after advantage in cancer therapies: the ability to concentrate dose inside the target volume and minimize dose to surrounding normal tissues.

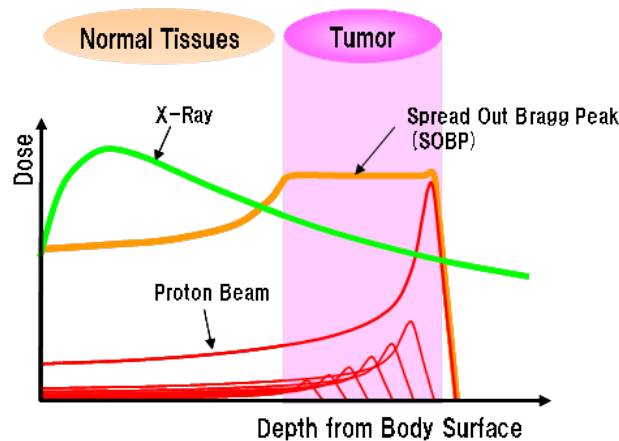


Figure 1.7: Superimposition of different Bragg peaks in a proto-therapeutic treatment. The convolution of the dose allows to irradiate the whole tumor region [9].

This allows to accurately irradiate the tumor with a low dose deposition on the surrounding tissues. Since the location of the Bragg Peak depends on the incident particle energy, varying the energy during the irradiation in a controlled way, one can superimpose many narrow Bragg peaks and obtain a *Spread-Out Bragg Peak* (SOBP), as shown in Fig.1.7, to better adapt the delivered dose to the shape of the tumor volume. This can be achieved in two ways : the first one is based on the interposition of an absorbing material of variable thickness on the beam path; the second one is based on the modulation of the beam energy during the irradiation. This modulation is feasible in some accelerators as synchrotrons, but it is more difficult with cyclotrons [4]. A more detailed description on these two technologies is presented in Section 1.5.1.

1.2.4 Particle Range and Straggling

The quality of hadrontherapy treatments is closely connected with the ability to predict the penetration length of particles when traversing the patient's body. Much research is therefore aimed at developing methods that allow to precisely measure the beam *range*, defined as the depth at which primary particles have stopped [22]. In order to quantify the definition of particle range, we refer to a conceptual experiment in which mono energetic particles generated by a collimated source are counted by a detector after passing through an absorber of defined thickness. In this case the range can be determined as the ratio between the transmitted particles and the incident one (I/I_0) [12]. In Fig.1.8 is plotted the variation of this ratio as a function of the absorber thickness. The relative count rate is very flat as more and more absorber is added, until near the end of the curve it drops sharply to zero due to the stochastic nature of the energy loss. This behavior, known as *Range Straggling*, leads to a Gaussian like distribution of the range and it is also responsible for the longitudinal widening of the Bragg Peak and for the reduction of its height, as shown in Fig.1.9.

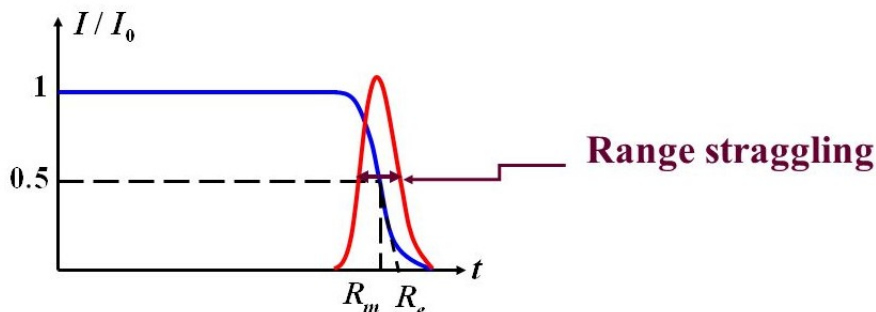


Figure 1.8: Behavior of the ratio I/I_0 as a function of the absorber thickness. R_m and R_e are respectively the mean range and the extrapolated range. The range straggling is also shown [11].

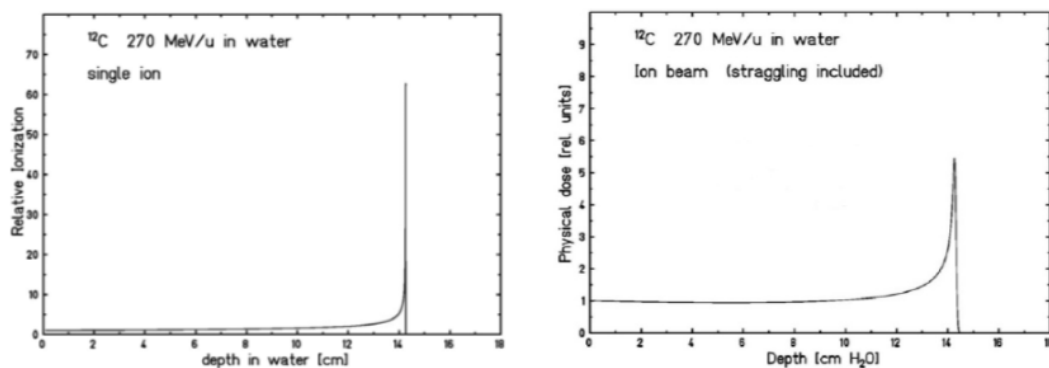


Figure 1.9: Left: Depth-dose profile for a ^{12}C ion without straggling. Right: Depth-dose profile for a ^{12}C ion of the same energy considering straggling [6].

The main problem in the use of Eq.(1.2) is that the mean is weighted by very rare events with large single-collision energy depositions and it does not contain information about the statistical fluctuations in the energy lost by the incident particles. Far better and more easily measured is the most probable energy loss, that in a detector is considerably below the mean given by the Bethe-Bloch equation. The distribution of the energy loss is thus a Gaussian with thick absorbers, due to the large number of collisions, but becomes asymmetrical in thin absorbers, where it is described by the *Landau-Vavilov distribution*. The effect is known as *Energy Straggling*. As shown in Fig.1.10, the energy loss distribution

is characterized by a narrow peak followed by a long tail for higher values of the deposited energy. This tail originates from the small number of individual collisions, each with a small probability of transferring large amounts of energy. The most probable energy loss is then given by the Landau-Vavilov formulation [25]:

$$\Delta_p = \xi \left[\ln \frac{2mc^2\beta^2\gamma^2}{I} + \ln \frac{\xi}{I} + j - \beta^2 - \delta(\beta\gamma) \right] \quad (1.4)$$

where $\xi = (K/2)(Z/A)z^2(x/\beta^2)$ MeV is known as the scale for the Landau distribution, and $j=0.2$. While dE/dx is independent of thickness, Δ_p/x scales as "a $\ln x + b$ ". The effect of the thickness on the energy loss distribution is shown in Fig.1.10. So, in the limit of many collisions the Landau-Vavilov distribution

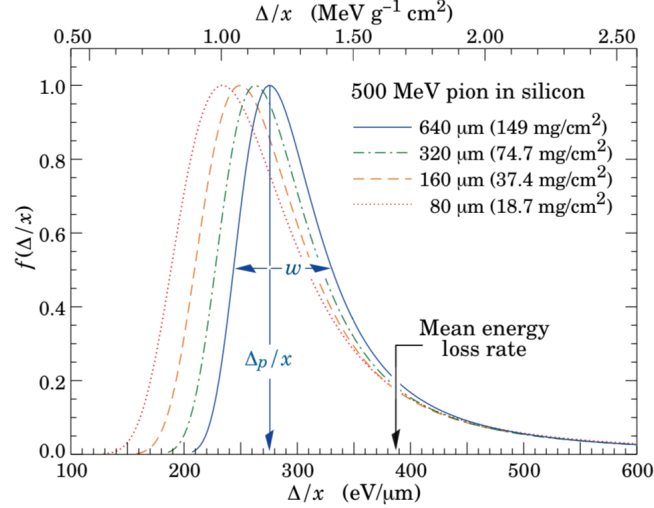


Figure 1.10: Example of Landau distribution for 500 MeV pions incident a thin Silicon detector for different values of thickness [25].

becomes Gaussian and the energy straggling can be parametrized in the following way [2]:

$$f(\Delta E) = \frac{1}{\sqrt{2\pi}\sigma} \exp \left[-\frac{(\Delta E - \overline{\Delta E})^2}{2\sigma_E^2} \right] \quad (1.5)$$

where ΔE is the energy lost by the incident particle, $\overline{\Delta E}$ is the mean energy loss and σ_E has the following expression [2]:

$$\sigma_E^2 = 4\pi Z_{eff} Z_t e^2 n \Delta x \left[\frac{1 - \beta^2/2}{1 - \beta^2} \right] \quad (1.6)$$

where Z_t is the target particles charge, n the number of electrons per unit volume and Δx the traversed thickness. The variance σ_R^2 of the range straggling is related to the variance σ_E^2 of the energy straggling and it is given by [2]:

$$\sigma_R^2 = \int_0^{E_i} \left(\frac{d\sigma_E^2}{dx} \right) \left(\frac{dE}{dx} \right)^{-3} dE \quad (1.7)$$

where E_i is the particle initial energy and σ_E has the expression given in (1.6). The ratio of the straggling width, σ_R and the mean range R is nearly constant and can be described as [16]:

$$\frac{\sigma_R}{R} = \frac{1}{\sqrt{M}} f \left(\frac{E}{Mc^2} \right) \quad (1.8)$$

where f is a slowly varying function depending on the absorber and M is the projectile mass. Because of the $1/\sqrt{M}$ dependence, the relative straggling σ_R/R is smaller for heavier ions than for protons (Fig.1.11).

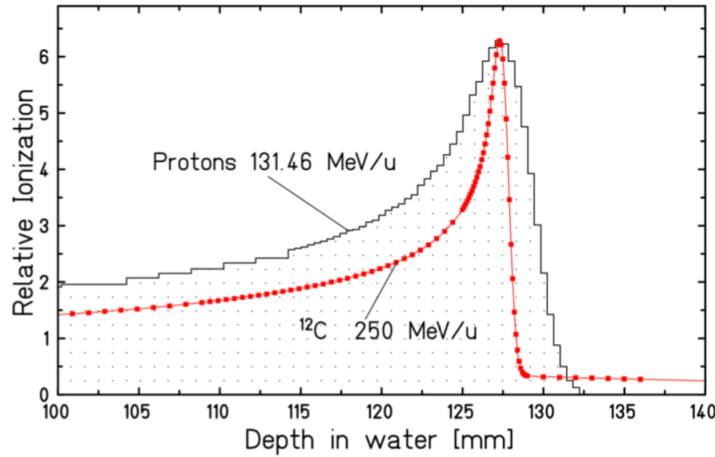


Figure 1.11: Measured Bragg peaks of proton and ^{12}C ions having the same range in water [16].

1.2.5 Multiple Coulomb Scattering: Lateral Beam Spread

In addition to losing energy by ionization or excitation mechanisms, a charged particle may undergo elastic Coulomb scattering events with target nuclei. These collisions are mediated by the Coulomb forces between the electric field of the traveling particle and electric fields of the target nuclei of atoms of the material. The quantity that well describes this kind of events is the Rutherford differential cross section [24]:

$$\frac{d\sigma}{d\Omega} \propto \frac{Z_p^2 Z_t^2}{E^2} \frac{1}{\sin^4(\theta/2)} \quad (1.9)$$

The quantities Z_p and Z_t represent respectively the charge number of the projectile and the target nuclei, E is the projectile energy and θ is the deflection angle from the original direction. It is noticeable that projectiles characterized by an high value of the energy have a lower probability to be deflected and high values of the charge of both, projectile and target, enhance the interaction between them. Each scattering event adds a small deviation to the incoming particle trajectory, due to the $\sin^4(\theta/2)$ dependence. Even if this deflection is small, the cumulative effect of these small angle scatterings is a net deflection from the original particle direction. When the traversed thickness is extremely small, the probability

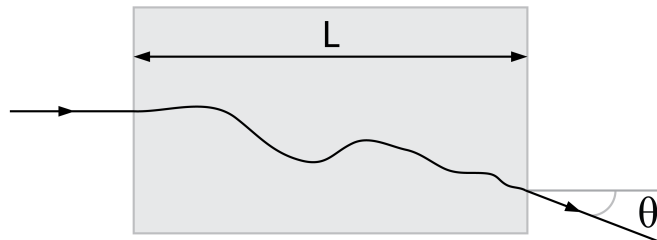


Figure 1.12: Multiple Scattering: the particle, interacting with target nuclei, undergoes elastic scatterings and deviates from its original direction by an angle θ [26].

to have more than one interaction is negligible. Whereas, for sufficiently thick materials, the number of interactions becomes high and the particle undergoes a series of scattering events. In this last case, the statistical distribution function $F(\theta, d)$ for the resulting scattering angle θ when traversing a thickness d of material has been provided by Molière. In this formulation the angular distribution is expressed as a series. For small angles the higher-order terms of this series can be neglected and the angular distribution can be approximated by a Gaussian with

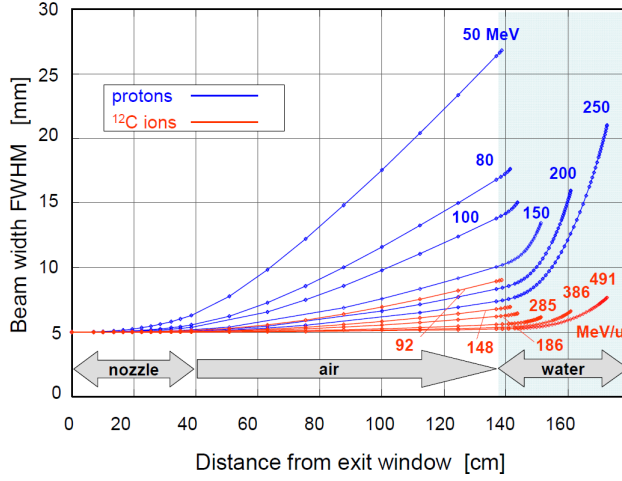


Figure 1.13: Calculated beam spread for ^{12}C ions and protons for an initially parallel particle beam passing through the nozzle and entering a water absorber. Carbon ions show a much smaller spread than protons at the same penetration depth [16].

a standard deviation given by Highland [25]:

$$\sigma_{\theta}[\text{rad}] = \frac{13.6\text{MeV}}{\beta cp} Z_p \sqrt{\frac{d}{L_{\text{rad}}}} \left[1 + 0.038 \ln \left(\frac{d}{L_{\text{rad}}} \right) \right] \quad (1.10)$$

where p is the projectile momentum and L_{rad} is the radiation length typical of the medium.

The multiple scattering is the responsible for the lateral spreading of the beam, leading to a dose release in an extended region. The angular spread for heavy charged particle is small, but increases significantly towards low energies due to the βcp term in the denominator of the Eq.(1.10). Comparing beams with the same range in water, it has been shown that the angular spread σ_{θ} is larger for protons than for heavier ions, as shown Fig.1.13. This smaller lateral deflection of heavy ions represents an important advantage, especially for treatments of tumors located near organs at risk (OAR). However, it should be underlined that in the irradiation of tissues with large density inhomogeneities even a small lateral spread may translate into a considerable range broadening.

1.2.6 Nuclear Interactions: the role of fragmentation

Even if the probability of nuclear reactions is much smaller than the probability of interaction with atomic electrons, the nuclear interactions lead to significant effects at large penetration depths, that are relevant in hadrotherapeutic applications. Contrary to electromagnetic interactions, a comprehensive and analytical model of nuclear interactions does not exist yet. However, the use of numerical models, which can be exploited for Monte Carlo simulations, is the unique method to deal with nuclear interactions.

In this kind of interactions, projectile particles directly interact with the atomic nuclei of the target. Three qualitatively different type of collisions can be distinguished:

- Elastic collisions
- Quasi-Elastic collisions
- Inelastic collisions

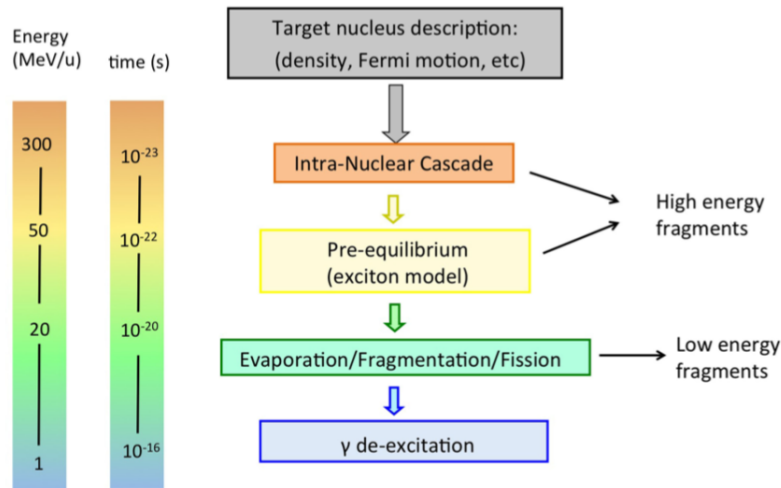


Figure 1.14: Schematic representation of nucleons-nucleus interaction sequence. The time scale and energy of each phase are highlighted [53].

The first phenomenon is substantially the analog of the Coulomb diffusion, but in this case the event is mediated by the strong nuclear force instead of the electromagnetic repulsion. In the elastic nuclear interaction the kinetic energy is conserved and the nucleus stays intact. The second one is similar to the previous one, the quasi elasticity is due to the fact that the kinetic energy of the system is not conserved. The projectile gives only a small fraction of its energy to the target that reaches an excited state becoming unstable, then it falls back to its original state by a series of mechanisms that depend on the mass of the target nucleus and on the energy left. In inelastic collisions, instead, a more violent reaction occurs, leading to the partial fragmentation or the complete disintegration of both projectile and target nuclei. Since there are relevant differences in modeling nuclear interactions for proton and heavier ions, it is useful discuss their behavior in nuclear reactions separately.

It is usually assumed that a **proton** hitting an atomic nucleus undergoes a series of nucleon-nucleon collisions that can be described as a sequence of three stages, schematically displayed in Fig.1.14 [53]:

- (Generalized) Intra-Nuclear Cascade (INC). This model is commonly used to describe nuclear interactions of nucleons in an energy range between 50 MeV and hundreds of GeV. The basic idea is that the incident particle interacts with quasi-free nucleons in the target nuclei. The target nucleus is modeled as a Fermi gas of cold and free nucleons. This “free” nucleon approach is valid as long as the wavelength of the incident particle is much smaller than the average distance between nucleons and also much smaller than the mean free path inside the target nucleus. Another requirement for this approach is that collisions must take place independently, meaning that the time in which a collision happens must be smaller than the time between collisions. Once a nuclear interaction happens, the produced secondary particles, having high energy, can scatter again in the same nucleus or escape, through a process known as intra-nuclear cascade.
- Pre-equilibrium. In this stage, the particles energy in the cascade reaches values of the order of few tens of MeV. Even if the INC terminates, the thermal equilibrium is not already reached. The stage is considered as a chain of events in which successive nucleon-nucleon collisions occur within a *particle-hole*. In this formalism, the residual excitation energy is partitioned among the nucleons, which are then excited from within the Fermi sea,

leaving a hole. Protons, neutrons and light fragments are therefore emitted until the excitation energy decreases below any emission threshold.

- De-excitation. When equilibrium is reached, the nucleus can dissipate its remaining energy in different ways, depending on the mass of the target nucleus and on the energy:
 - Nuclear evaporation: it is the emission of light fragments, with kinetic energies of a few MeV.
 - Fission: breakage of high Z nuclei ($Z > 64$) into two fragments. Such nuclei are not found in human body apart from implants.
 - Fermi-breakup: this mechanism applies to light nuclei ($10 \leq A \leq 20$), if the excitation energy of the nucleus is larger than the binding energy of some fragmentation channels. In such conditions the nucleus disassembles into smaller fragments.
 - γ emission: finally, the residual nucleus may de-excite through the emission of γ rays.

The first two steps are identified as “dynamic” stages of the process, since they are characterized by a time scale of the order of $\approx 10^{-22}$ s, while the last step, having a time scale that varies from $\approx 10^{-8}$ s to 10^{-6} s, is therefore pointed as “slow” stage.

When dealing with **heavy ions**, the main difference in treating nuclear interactions is that the incoming nucleons are not free. In this case, nuclear interactions are usually modeled considering two phases [16]: *abrasion* and *ablation*. The abrasion is a thermalization, or excitation, process in which the energy is directly transferred to the nucleons involved in the collision. An excited quasi-projectile, a quasi-target fragment at rest and excited light fragments are formed (*fireball*). The ablation is the de-excitation of the three objects (projectile fragment, target fragment and fireball) through the same processes described for protons. Some

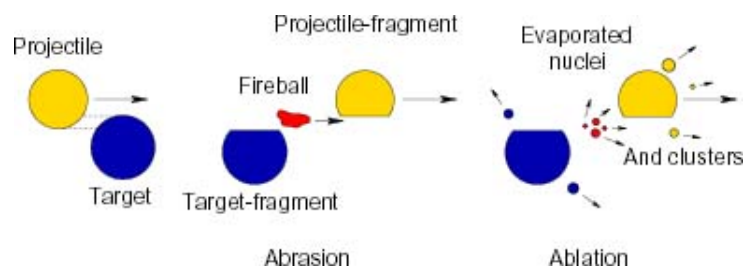


Figure 1.15: Abrasion-ablation model for heavy ions nuclear reactions [27].

important conclusions can be drawn for the effects of fragmentation relevant for charged particle therapy: the first one is the “disappearance” of the projectile in its original configuration, since the collision changes its nature and fragments are produced. As a consequence, the projectile does not deposit its energy up to the desired Bragg peak position. The second effect is the secondary particles production. These fragments have a smaller size but a velocity close to the velocity of the primary ions. Because of the A/Z^2 scaling of the range, these fragments can deposit their energy at penetration depths beyond the projectile Bragg Peak [25],[16].

The impact of nuclear fragmentation on the depth-dose profile is shown in Fig.1.16 : with increasing penetration depth, the peak-to-entrance ratio becomes gradually smaller, mainly caused by the exponentially diminishing flux of primary ions. The buildup of lower- Z fragments is clearly visible in the dose tail behind

the Bragg Peak (BP) at larger depths. Additionally, the BP are increasingly broadened by straggling.

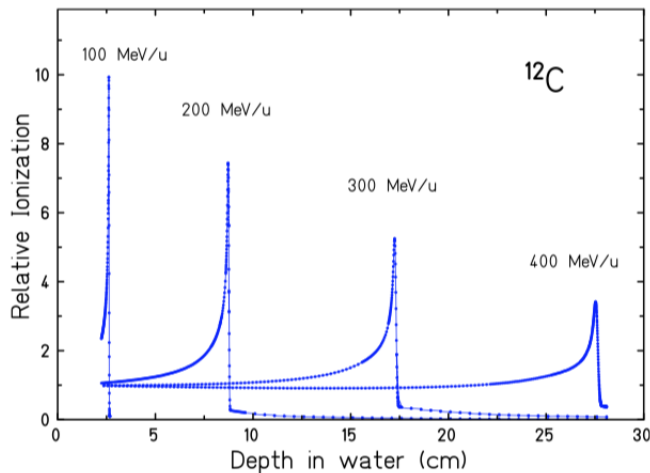


Figure 1.16: Measured Bragg curves of ^{12}C ions stopping in water [16].

1.3 Biological effects of radiation

The capability of radiation to destroy a tumor depends on the induced biological damage in cancer cells. It is therefore important to introduce some basic concepts about radiobiology.

When cells are exposed to ionizing radiation, the biological damage occurs due to the chemical changes caused by ionization at cellular level. The DNA is the primary target for radiation induced cell killing, due to its central role in all cellular functions. When ionizing radiation is absorbed in biological materials, the damage to the cell may occur through direct or indirect action, as schematically shown in Fig.1.17. In direct action the radiation interacts directly with the critical target (the DNA) in the cell. The atoms of the target itself may be ionized or excited through Coulomb interactions, leading to the chain of physical and chemical events that eventually produce the biological damage. In indirect action the radiation interacts with other molecules and atoms within the cell (mainly water) to produce free radicals, which can, through diffusion in the cell, damage the DNA. In interactions of radiation with water for example, extremely reactive radicals such as H_2O^+ and OH^- are produced [14].

Various phenomena can take place when a cell is irradiated [30]. The radiation may pass through the cell without any damage: ionization may form chemically active substances which can alter the structure of the cells, but these alterations may be no different as those that naturally occur and may have no negative effects. The radiation may damage the cell, but the cell repairs the damage: the organisms develops a series of processes for which the DNA is able to self-repair. When a Single-Strand Breaks occurs, most DNA is repaired with no long-term effects. In case of a Double-Strand Break, the repair is difficult to achieve. If a damaged cell needs to perform a function before it has had the time to repair itself, it could replicate in the damaged form. These altered cells may reproduce themselves at an uncontrolled rate. Finally, if the cell is extensively damaged by radiation it may die. As will be discussed in the Section 1.4.2, heavy ions are characterized by an enhanced biological effectiveness in cell killing compared to photon, due to their higher ionization density.

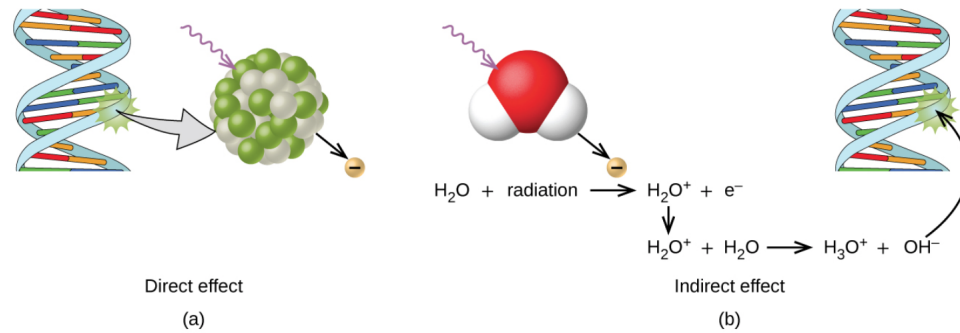


Figure 1.17: Direct and indirect radiation-induced damage to the DNA [34].

1.4 Biological and dosimetric parameters

Radiation dosimetry deals with methods for a quantitative determination of energy deposited in a given medium by directly or indirectly ionizing radiations. The most commonly used dosimetric quantities and their units are defined in the following.

1.4.1 Absorbed dose

Biological effects in radiation therapy as well as in proton and heavy particles treatments, are related to the *absorbed dose*. It is defined by the *International Commission of Radiation Units, ICRU*, as the average energy E released by the ionizing radiation per unit mass m of material [32]:

$$D = \frac{dE}{dm} \quad (1.11)$$

The unit measure is Gray (1Gy=J/kg).

For several decades the quantity has been shown to be useful in radiation therapy, as well as in radiation protection and radiobiology. However, the absorbed dose is not enough to determine the biological effects of different radiation qualities. A physical quantity which better describes the radiobiological consequences originated from different types of radiation is the Linear Energy Transfer, described in the following.

1.4.2 Linear Energy Transfer, LET

The severity and permanence of the chemical alterations of the biological molecules are directly related to the local rate of energy deposition along the particle track. When we focus on the medium rather than the particle, we can introduce the *Linear Energy Transfer*(LET). It is defined as the amount of energy E released per unit length by the ionizing radiation traversing the material:

$$LET_{\Delta} = \frac{dE_{\Delta}}{dx} \quad (1.12)$$

where x is the path length. The units of LET are often given as keV/ μ m.

The LET is nearly identical to the *Stopping Power*. The differences arise when a portion of the radiation energy is liberated in such a way to produce energy deposition at a substantial distance from the original particle track. While the specific energy loss includes such releases of energy as part of the energy loss of the particle, the LET counts only the energy deposited along the track. The LET is thus used to quantify just releases coming from the incident particles, all that releases induced by secondary particles are not taken into account [10],[12].

Those radiations with large values of LET, such as heavy charged particles, tend to result in a greater biological damage than those with lower LET, even though the total energy deposited per unit mass is the same. This is due the presence of secondary electrons (δ -rays) produced in the Coulomb interaction of heavy ions with the target. These electrons can generate further excitations and ionizations. Most of them deposit their dose in the center of the primary ion tracks, whose typical diameter is of the order of nanometers. As a consequence, the probability of damaging the DNA increases, inducing the enhanced heavy ion cell killing capability.

1.4.3 Relative Biological Effectiveness, RBE

As previously seen, radiations of different quality produce different levels of biological and clinical effects. Radiation quality is related to the type of particles and their energy spectrum. In radiobiology, it has become customary to use the *Relative Biological Effectiveness* to quantify differences in biological effectiveness of different radiation qualities.

It is defined as the ratio between two absorbed doses delivered with two radiation qualities, one of which is a "reference radiation" (predominately, ^{60}Co γ rays), that result in the same effect in a given biological system under identical conditions:

$$RBE = \left(\frac{D_{ref}}{D_{ion}} \right)_{isoeffect} \quad (1.13)$$

where D_{ref} is the reference dose and D_{ion} is the delivered dose of the radiation of interest. A common way to analyse the different effects of photons and charged particles on the RBE is by means of the so called *cell survival curves*.

A cell survival curve describes the surviving fraction of cells as a function of the radiation dose. Survival curves are usually represented by plotting the surviving fraction on a logarithmic scale on the ordinate against dose on a linear scale on the abscissa, as shown in Fig.1.18 (a). Each type of radiation is characterized by a proper shape. Being fixed a certain "survival level", Fig.1.18 shows how the RBE is determined, for a specific type of radiation. It has been demonstrated that in the case of charged particles, the RBE is dependent on radiation LET. The variation of the RBE with the LET is shown in Fig.1.18(b). The general trend is the following: an increase from low LET up to 100-200 keV/ μm and then a decrease at very high LET caused by overkilling effect. In ion treatment planning the RBE compares the heavy ion or proton radiation biological effect with the conventional radiation results. By multiplying the RBE with the physical absorbed dose, it is possible to determine the photon-equivalent dose, which quantifies the conventional radiation dose that would lead to the same biological effect as tested radiation. Protons used in clinical practice generally have an entrance energy between 150 MeV and 250 MeV corresponding to a low-LET in water around 1 keV/ μm . The LET on the SOBP increases with depth in a range of 2-6 keV/ μm . This modest LET increase does not considerably affect the RBE, that is why protons for therapy are normally considered to have an RBE of 1.1 throughout the entire radiation field. However, recent experiments [7] has shown that the RBE in proton therapy significantly overcomes the current adopted value of 1.1, leading to an increase in the of biological damage to the entrance channel, *i.e.* in the region of healthy tissues. Using a constant RBE=1.1 can therefore lead to an underestimation or overestimation of the deposited dose in the healthy tissues. The situation in heavy-ion therapy is more complex because of the large variations of the LET, that reaches a maximum whose value and position depend on the particle type. Light particles are generally more effective than heavier particles at the same LET, because they are slower and therefore have a narrow track width.

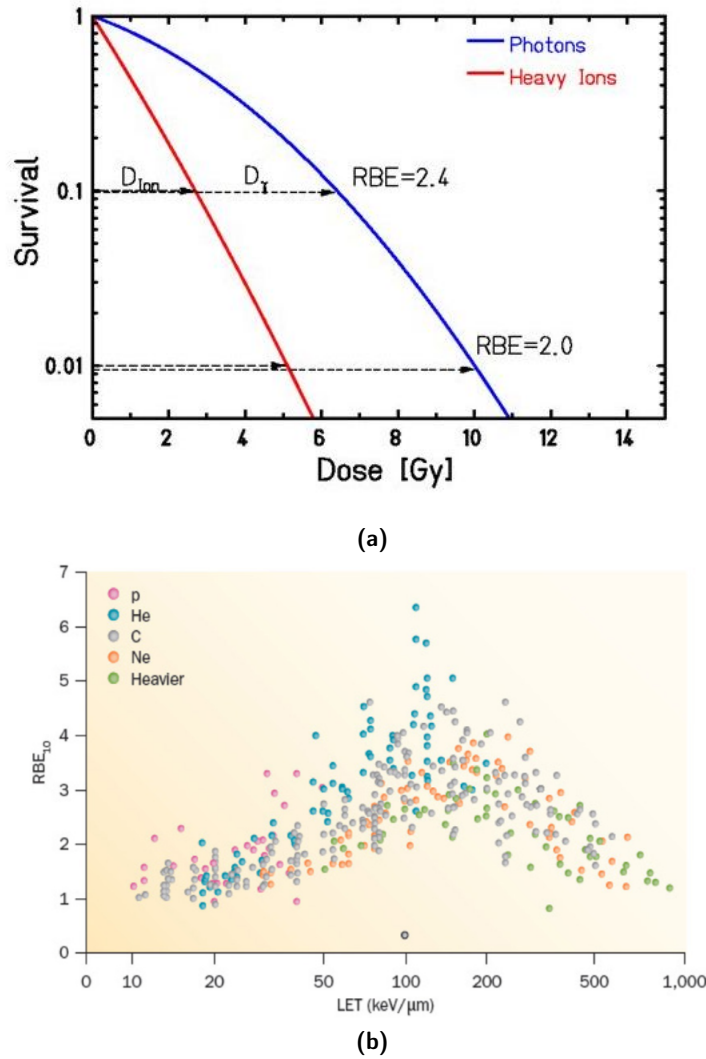


Figure 1.18: (a) Survival curves and RBE evaluation for survived fractions equal to 10% and 1%. It is immediately noticeable that the RBE of a certain radiation is not constant with the survival levels [33]. (b) RBE calculated at 10% survival against LET: different colors indicate different ions, from protons to heavy ions [7].

When deciding on a dose prescription for a new ion beam, it is necessary to weigh a variety of factors considering the dependence of the RBE not only on the radiation type and on the dose but also on the biological system. The beam characteristics change during tissue penetration, therefore delivering a constant physical dose does not lead to a uniform biological effect. In Fig.1.19 is shown an example of calculation and optimization of biological effective dose [37]. The RBE must be computed in order to obtain a uniform biological effective dose over the target.

1.4.4 Oxygen Enhancement Ratio, OER

Another factor affecting the shape of the dose-response is the concentration of oxygen in tissue that leads to a different response to the irradiation. Hypoxic cells have been shown to be considerably more radio-resistant (Fig.1.20 (a)). Unfortunately, the multiplication of neoplastic cells is so rapid that the blood supply is not sufficient to guarantee the same oxygenation as the healthy cells, so that *hypoxic* regions may arise. Therapies of different nature react in a different way to the presence of oxygen. To quantify the effectiveness of different radiations against hypoxic zones the *Oxygen Enhancement Ratio* parameter has been introduced. It is the ratio of the doses of radiation required to produce a the same

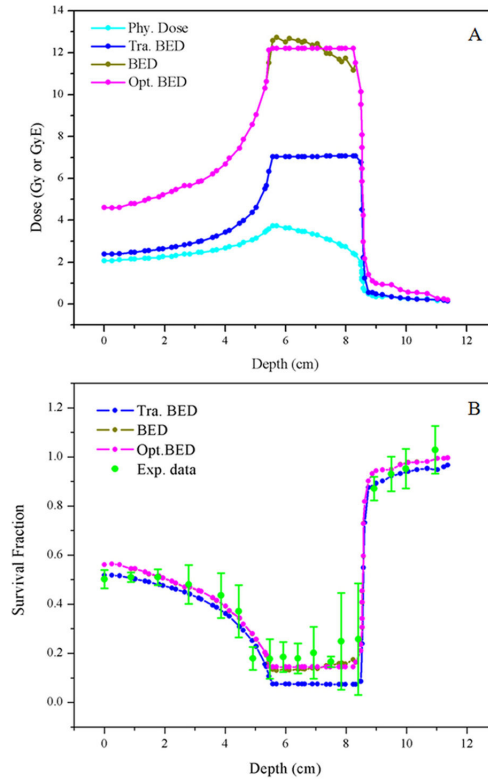


Figure 1.19: (A) Optimization of Biological Effective Dose (BED) and (B) the corresponding cell survival fraction for a 200 MeV/u ^{12}C ion beam. The terms *Phy.*, *Tra.* and *Opt.* in the figures represent physical dose, BED calculated and BED optimized, respectively. Experimental data from [30].

level of cell killing when delivered to anoxic (D_{anoxic}) or oxygenated ($D_{oxygenated}$) tissues:

$$OER = \left(\frac{D_{Hypoxic}}{D_{Oxygenated}} \right)_{iso} \quad (1.14)$$

Typical values of the OER vary from 1 (the damage produced by the radiation does not depend on the presence of oxygen) to 3 (the radiation is considerably affected by the presence of oxygen) [10],[31].

The study of this parameter is very important in hadrotherapeutic treatments, it has been observed that high-LET ions are characterized by a value of the OER much lower than that one of X-rays. In general, the higher the LET is, the more the OER tends to 1 (Fig.1.20 (b)).

1.5 Hadrontherapy technology

The use of hadrons for cancer therapy as an alternative to conventional radiation has led to significant improvements in treatment techniques. The need of making available particles at energies of several hundred MeV, which are required for these therapies, led to the development of new accelerators technology. The best candidates for medical applications are the *cyclotron* and the *synchrotron*.

The choice of the accelerator type plays a fundamental role in the design of a hadrontherapy facility. Several factors must be taken into account: cost, reliability as well as the advantages deriving from a simplified design. On one hand, cyclotrons offer stable and adjustable beam intensities, but they work at fixed energy (*i.e.*, fixed frequency and fixed field). In this case the energy modulation is made by means of degraders placed along the beam line. Synchrotrons, on the other hand, offer fast energy variations: the energy of the beam can be varied from one cycle to the next in steps as small as 1 MeV. The main drawback in

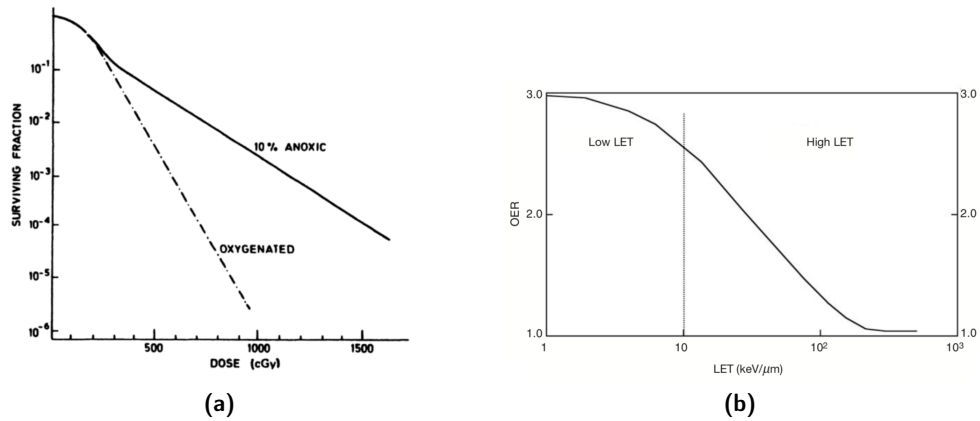


Figure 1.20: (a) Schematic cell survival curve of a tumor cell population with a portion of anoxic cells that produce the radio-resistant tail at higher dose levels [31]. (b) OER plotted against LET. The vertical dashed line separates the low LET region from the high LET region [14].

this case is the huge size of such accelerators due to the more complexity of the design.

In the following Section a description of the accelerators is presented, highlighting their advantages and disadvantages.

1.5.1 Cyclotron and Synchrotron

All accelerators are based on the same principle: a charged particle is accelerated through a gap between two electrodes when a potential difference is applied. A schematic representation of both technologies is shown in Fig.1.21.

A **cyclotron** consists of two D-shaped electrodes, known also as “*dees*”, placed face to face in a vacuum chamber. This vacuum chamber is placed between the two poles of a large magnet which creates a uniform perpendicular magnetic field. Charged particles are then injected into the centre of the chamber, in a narrow gap led between the two D electrodes (orange spot in Fig.1.21 (a)). A high frequency alternating voltage is applied across the dees. This voltage alternately attracts and repels the charged particles causing them to accelerate when crossing the gap. The constant magnetic field causes the particle to move in a circular path and, as they gain more energy from the accelerating voltage, they spiral outwards until they reach the outer edge of the chamber in order to be extracted and addressed to the target. The size of the vacuum chamber determines the length of the spiral path and hence the amount of energy gained by the particle [14]. In this way higher energies can be achieved using the same voltage and, at the same time, metal dees do not need to be of great length. Ernest Lawrence, inventor of this technology, achieved a proton energy of 80 keV using a cyclotron with a diameter of just 11 cm. As previously introduced, the extraction energy of a cyclotron is fixed, so that energy variation at a patient must be achieved by means of absorbers. So, if from the point of view of the simplicity of the design, cyclotrons offer numerous advantages on the other hand, these degrader have the undesirable effect of introducing an increased beam emittance from scattering and an increased energy spread from straggling. Furthermore, the nuclear inelastic scattering of the projectiles on the absorber material produces different particles that can reach the patient.

Whereas in a cyclotron the particle beam moves along a spiral trajectory starting from the centre of the machine, in a **synchrotron** the beam circulates along a fixed orbit and the magnetic field varies according to the acceleration

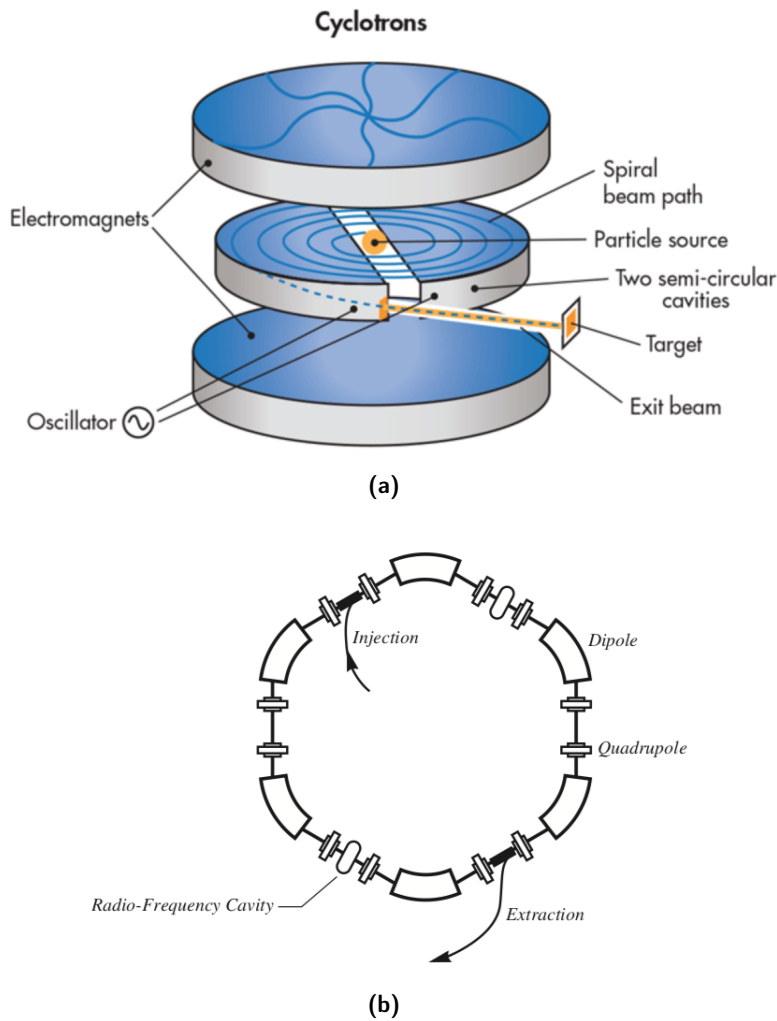


Figure 1.21: Schematic representation of Cyclotron (a) and Synchrotron (b) functioning [39].

process. The acceleration is usually achieved using radio frequency cavities placed along the beam line, as shown in Fig.1.21 (b). In addition, in order to create an appropriate focusing channel and to bend the particles, *dipole* and *quadrupole* magnets are interposed in the ring [39]. The particles enter the ring only after they have been accelerated by a linear accelerator (*LINAC*). The main advantage offered by a synchrotron is its energy variability, so that the modulation of the Bragg Peak can be achieved without the use of absorbers, thus preserving beam quality. On the other hand the accelerator design is more complex than a cyclotron working at fixed frequency and magnetic field [38]. As an example one can mention the synchrotron used at the CNAO (Pavia, Italy) (Fig.1.22).

1.5.2 Beam Delivery

As largely discussed, one of the main advantages in hadrontherapy is the precise coverage of the tumor volume with respect to conventional radiation therapy. However, it is still clinically advantageous to be able of varying the orientation of the incident particles. While a single field direction may be preferred for some treatments, such as ocular cancers, in many cases it should be preferable irradiated the tumor volume from different angles. This is done by coupling the accelerator, via a beam transfer line, with a movable mechanism, known as *gantry*, whose functioning principle is shown in Fig. 1.23. In typical particle therapy installations a single accelerator source delivers the beam to more than one treatment room, each of which may be equipped with a gantry or with a fixed beam line

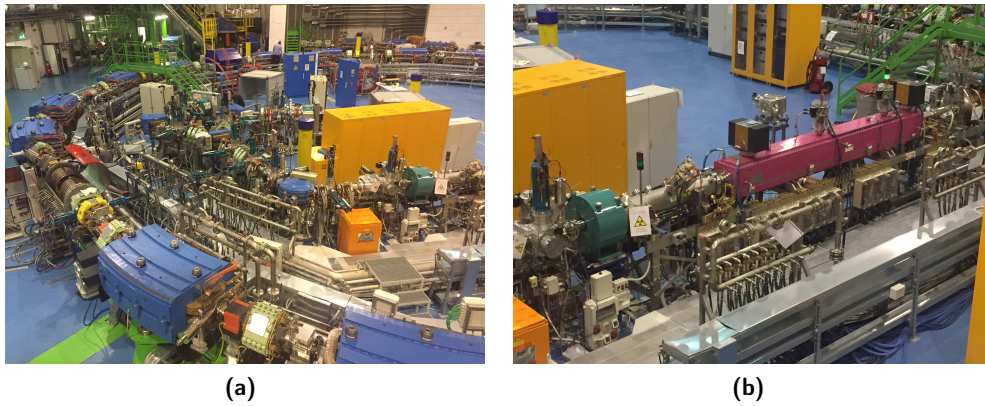


Figure 1.22: (a) Overview of the synchrotron room at CNAO (Pavia, Italy). (b) Details of the linear accelerator.

[39]. Most gantries are *isocentric*: the patient is in a fixed position and receives the required dose while the gantry rotates around him. As shown in Fig.1.23, isocentric gantries comprise a number of dipole and quadrupole, to correctly address the beam from the source to the patient, as well as monitors to measure beam position and profile.

Depending on the adopted accelerator, the achievement of a conformal irradiation of the target volume can be done with *active* (synchrotron) or *passive* (cyclotron) methods. The **passive** method consists of interposing specific pieces of matter and mechanical devices on the beam trajectory, in order to match at the best the distal shape of the tumor, as shown on Fig.1.24. The required SOBP is generated using a range modulator, that is constituted by rotating absorbers of variable thickness placed on the beam path, and by means of additional pieces of plastic that constitute the so called range shifter. Finally, longitudinal compensators, specifically conceived for each patient, allow to achieve the last conformal shaping of the beam just before the skin of the patient [3]. The main advantage of this method is its simplicity, since the treatment can be performed without changing the accelerator parameters. Its main drawback is the production of unwanted secondary particles, especially when using ion beams. Better results can be achieved by **active** methods (Fig.1.25). One of these techniques consists in painting in three dimensions the tumor by deviating a pencil beam with magnets. The tumor is divided in planes, each of them corresponding to a given beam energy. The main advantages consist in a better conformity of the dose distribution to the target and the absence of patient-specific accessories. On the other hand, it requires an excellent beam control and is hence very difficult to achieve.

1.6 Treatment Planning

To develop a treatment planning it is necessary to simulate the dose distribution to the tumor and the surrounding normal tissue and organ at risk which would result from a treatment. In this way, parameters of interest can be extracted in order to correctly predict at the best the treatment outcome. These simulations are performed by means of dedicated *Treatment Planning Software* (TPS).

The treatment planning consists of several steps. In the first step the patient undergoes cross-sectional imaging in order to reconstruct the 3D tumor anatomy. At present, Computer Tomography (CT) is the basic imaging technique that serves treatment planning. Because of the high precision in striking the target achieved in hadron therapy, the correct positioning of the patient is of paramount importance. CT is therefore performed with the patient immobilized

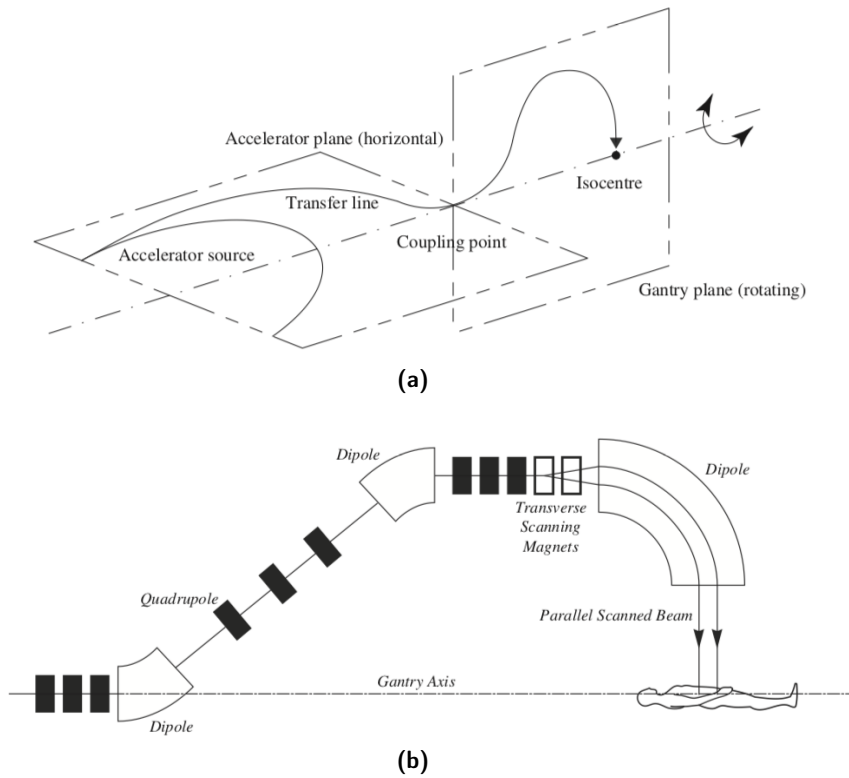


Figure 1.23: (a) Illustration of the functioning principle of isocentric gantries: the gantry plane rotates around an axis that is horizontal and passes through an isocentre that lies within the patient. (b) Schematic representation of a treatment room equipped with a gantry [39].

in the treatment position, so that potential attenuation effects on the beam can be accounted when performing dose calculations with the TPS. In some cases, when the soft tissue contrast of CT is not sufficient, additional imaging is performed by means of Magnetic Resonance (MR) imaging. After the image acquisition, the so-called *structure segmentation* follows. In this phase the volume to be irradiated and organs at risk are defined. At this point, combining the information coming from the imaging and medical advice, the treatment plan can be computed by TPS. Once the treatment plan is accepted, the beam parameters and treatment geometry parameters are transferred to a database in order to be applied [3].

1.7 Future prospects

Charged Particle Therapy has already evolved from physics research laboratories to clinical practice. There is clear evidence that dose distributions deriving from the use of charged particles are more favorable compared to photon therapy. A further advantage lies in the biological effects induced by charged particles. The increase in LET at the BP region produces an enhanced biological effectiveness in cell killing compared to conventional photon radiation therapy.

Some of the uncertainties in the Tumor Control Probability for these therapies are related to the lack of knowledge in particle interactions with tissues, especially for nuclear interaction cross sections at required therapeutic energies [7]. In the case of proton beams, target fragmentation can occur, generating a spectrum of low energy heavy recoils that depends on beam energy and target materials. These secondary particles are characterized by a very high LET and then high RBE, affecting the outcome of treatment plans. The overall biological effect arising from the mixed radiation field in a tissue voxel is strictly dependent on the components of the beam. Each fragment gives a different contribution

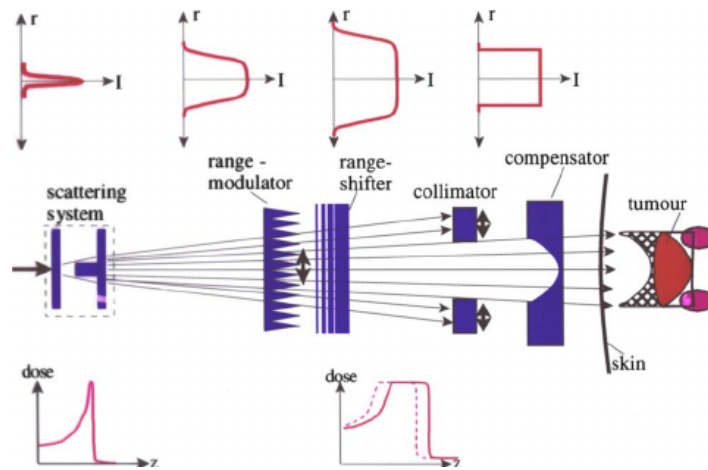


Figure 1.24: Sketch of a fully passive beam shaping system. The initially narrow beam is broadened by a scattering system and adapted to the target volume by various passive beam shaping devices. Adaptation of the dose field to the distal contour of the target volume is achieved by a compensator [2].

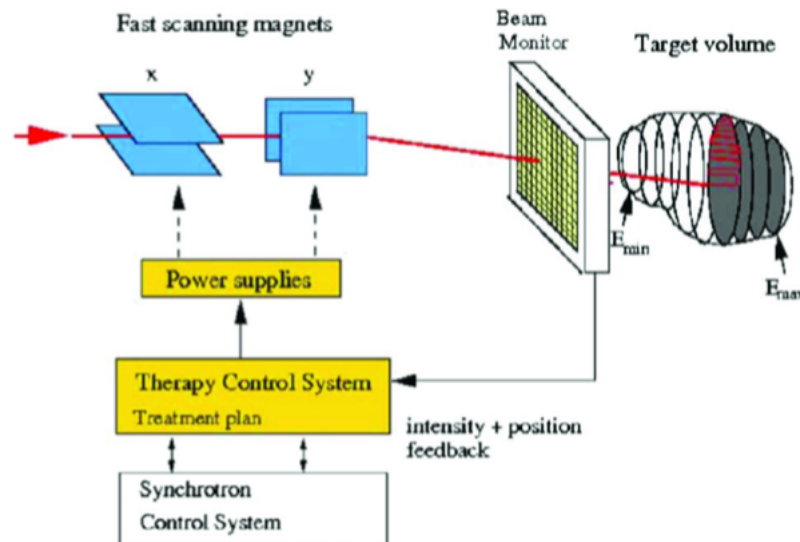


Figure 1.25: Principle of the active beam modulation. The target volume is irradiated by moving with magnets a pencil-like ion beam [2].

when interacting with the cells. In recent years some experiments have been also dedicated to the study of projectile fragmentation for ^{12}C ion beams, however this program was carried out only for a few energies [28],[29]. The accurate measurement of nuclear fragment spectra in an ion beam induced radiation field is in general of paramount importance for particle therapy, in order to provide reliable models that are needed in treatment planning algorithms. This is one of the goals of the FOOT (FragmentatiON Of Target) experiment, whose research program is described in the next Chapter.

Chapter 2

The FOOT experiment

One of the open issues in hadrontherapy is the lack of experimental measurements of the nuclear reaction cross sections for the fragments produced by protons and carbon ions in the energy range of therapeutic applications (50-200 MeV for and 50-400 MeV/u respectively). Treatment Planning Systems therefore rely upon simulation models, that suffer from many uncertainties since there is no exact calculable theory of these nuclear processes.

In recent years some experiments have been dedicated to the study of projectile fragmentation of ^{12}C ions. The experiment carried out on May 2011 at GANIL (Grand Accélérateur National d'Ions Lourds) in France, allowed the measurement of the double-differential cross sections of secondary particles produced in the ^{12}C fragmentation at 95 MeV/u [28]. Another example comes from the FIRST (Fragmentation of Ions Relevant for Space and Therapy) experiment, in which the double-differential cross sections of carbon ions fragmentations at 400 MeV/u have been provided [29]. However, these programs have been carried out only for a few energies.

The FOOT (FragmentatiOn Of Target) experiment has therefore been conceived to fill the energy gap in the available data of ^{12}C ion fragmentation cross sections, in order to include the effect of the fragmentation in the current Treatment Planning Systems. The other goals of the FOOT project are the characterization of target fragment production cross sections for proton beams and projectile fragment production cross sections for new, high-LET ions, like oxygen beams, in view of its potential against hypoxic tumors, as will be shown in Section 2.2. Further interest for a program of cross section measurements is also coming from the issue of radioprotection in space missions. Beyond many important risks of other nature, several radiation sources in space have to be considered. The design and optimization of the spacecraft shielding requires therefore a detailed knowledge of the fragmentation processes.

In Sections 2.1 and 2.2 a comparison between the proton and heavy ion therapy is introduced, focusing on the RBE and the fragmentation effects. In Section 2.3 and 2.4, the adopted experimental strategies and the criteria that are at the basis of the FOOT apparatus design are shown, followed by the presentation of the experimental setup and in particular on the detector that is the object of study of this thesis (Microstrip Silicon Detector). Finally, in Section 2.7 an example of a Silicon strip detector is introduced, showing the configuration used during a test beam carried out at the Trento Proton Therapy Centre (Italy) on December 2017.

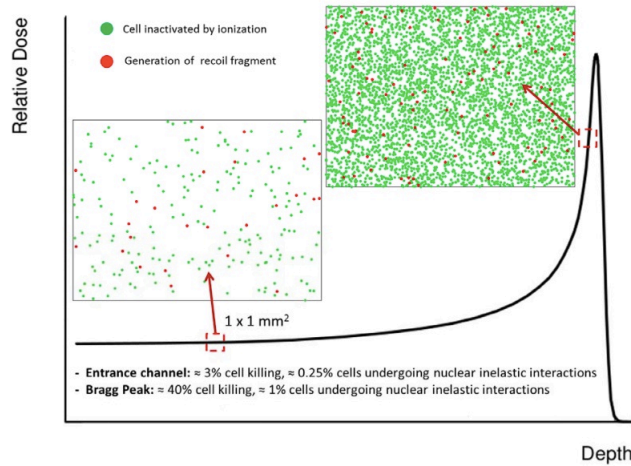


Figure 2.1: Illustrative image of the expected relative impact of target fragments in the entrance and in the peak regions as compared to the effect of inactivation by ionization. To estimate cell survival probability the LEM model has been used [7].

2.1 Target fragmentation in proton therapy

TPS for protons is a highly debated issue, recently appeared in a new attention as a possible explanation of patient toxicity data described by a Normal Tissue Complication Probability (NTCP). The commonly used constant factor of 1.1 for the RBE has been challenged, triggering large research efforts worldwide. As can be seen in Fig.2.1, the target fragmentation in proton beam is more relevant in the entrance channel region, where the impact of nuclear fragmentation, as compared to ionization induced cell killing, is less overwhelmed than in the peak region. Since the target fragment spectra are characterized by very low energies, this will prevent the particles traveling distances larger than few microns, resulting in a local dose deposition before the Bragg peak and furthermore making their experimental detection extremely difficult [41]. With the FOOT experiment it is planned to overcome this difficulty, by making use of the inverse kinematic approach, whose description is remanded to Section 2.3, opening in this way for the first time the possibility to investigate the target fragments effect on a biological level.

2.2 Projectile fragmentation in heavy ion therapy

When using heavy ions ($Z > 1$), projectile fragmentation events occur inside the patient tissues. The projectile fragments are produced mostly in the forward direction and have the same velocity, but lower mass, of the primary particle, resulting in a longer range than the projectile and therefore in an unwanted dose tail beyond the Bragg peak. In this case FOOT will be able to provide the fragmentation cross sections measurement from direct kinematics. In view of its potential against hypoxic tumors, Oxygen beams are increasingly considered as a valid alternative to carbon ions.

Since it has been shown that OER decreases substantially with higher LET, the rationale for using Oxygen beams is basically driven by their similar characteristics as compared to Carbon, but with a larger LET distribution able to be effective in contrasting to hypoxia. However, in normal (aerobic) conditions, the larger fragmentation of Oxygen beams in the target and in the entrance channel, makes their use less convenient as compared to lower Z ions (such as Carbon). The challenge in using this kind of beams is then a trade-off between the LET advantage and the worse fragmentation in normal tissues. The correct assessment

of the potential use of this new beam is strictly related to a very accurate description of its fragmentation cascade, for a large range of initial energies and in the complete range of its propagation [41].

All the above mentioned issues are the core of the MoVe IT (MOdeling and VERification in Ion beam Treatment planning) project. Indeed, the data provided by the FOOT experiment will be used in the MoVe IT project, to realize comparative TPS studies for all the most relevant ions available, which could be able to provide indications for different patient cases.

2.3 Experimental strategies

The main challenge of the FOOT experiment is the detection of very short range (order of microns) and very low energy (few MeV) fragments produced by the target fragmentation when proton beams are used. This makes their experimental detection extremely difficult. It is planned to overcome this difficulty with the use of an **inverse kinematic** approach, studying the fragmentation of different ion beams onto a target. Ion beams are chosen according to the principal constituent of the human body (H,C,O,Ca,etc.). By applying the Lorentz transformation one can then switch from the laboratory frame to the “patient frame”. For what concerns the **target**, the inverse kinematic approach implies the management of a pure gaseous Hydrogen target, leading to some technological challenges. For this reason one can think of using two different targets: an hydrogen enriched target, such as polyethylene (C_2H_4) and a pure graphite (C) target, which are easy to produce and manage. The fragmentation cross sections on H can then be then extracted by the subtraction of the cross sections of C and C_2H_4 [28]:

$$\frac{d\sigma}{d\Omega}(H) = \frac{1}{4} \times \left(\frac{d\sigma}{d\Omega}(C_2H_4) - 2\frac{d\sigma}{d\Omega}(C) \right) \quad (2.1)$$

This approach has been already validated in the experiment at GANIL [28] (Fig.2.2). With this approach produced fragments will have higher energy and a much longer range, making their detection easier.

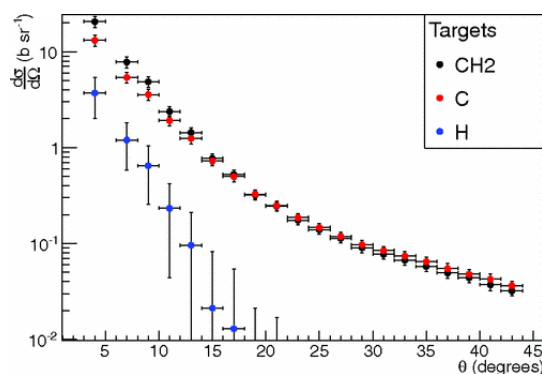


Figure 2.2: Carbon ions beam @95MeV on C and CH_2 targets: the fragmentation cross section on H is obtained by subtracting the cross sections of C and CH_2 [28].

2.4 The design criteria of FOOT apparatus

The basic idea is to realize an experimental setup which can be easily transportable, in such a way particle beams at different therapeutic centers can be exploited. As a consequence the overall experimental setup should lie within the 1.5-2 meters range. Furthermore, the characteristics of the detectors adopted for

the estimation of the above mentioned cross sections, must be properly chosen on the basis of the expected physical properties of the outgoing fragments. For example, it has to be taken into account the emission angle of the produced particles. Fragments heavier than Helium, are emitted with angles whose value can reach at the maximum $10^\circ \div 20^\circ$. On the other hand, the emission angle of light fragments can also assume values of the order of 70° . Thanks to Monte Carlo simulations, it is possible to analyse fragments characteristics and thus correctly plan experimental strategies.

The study of the physical processes by means of MC simulations shows that it is hard to achieve the desired angular acceptance for all secondary fragments with a setup of limited size. Since lower mass fragments can be emitted within a wider angular aperture with respect to heavier nuclei, the necessary size of the experimental apparatus would become too big in view of a table top setup design.

For these reasons in the FOOT experiment two different setups will be implemented:

- a setup based on electronic detectors and magnetic spectrometer concept, aiming to the identification and measurement of fragments heavier than ${}^4\text{He}$, covering an angular acceptance up to $10^\circ \div 20^\circ$ with respect to the beam axis;
- a setup exploiting the emulsion chamber capabilities that supplies complementary measurements for light fragments ($Z \leq 2$) extending the angular acceptance up to 70 degrees.

In this thesis we will not discuss in detail the emulsion setup. For a more complete knowledge of this apparatus the reader should refer to [41].

2.5 The Electronic Detector Setup

Object of the analysis are the fragments with $Z \geq 2$ and the measurement of the relative energy spectra. The driving criterion of the detector design is the need for a robust charge and isotopic identification of the produced fragments. For this purpose, the setup will aim to measure momentum, kinetic energy and Time Of Flight (TOF) of the produced fragments. The fragments dE/dx is measured through the energy release in a thin slab of material (ΔE).

The detector performances to be achieved are the following:

- momentum resolution $\sigma(p)/p$ at the level of 5%;
- TOF resolution at the level of 100 ps;
- energy resolution $\sigma(E_k)/(E_k)$ at the level of 2%;
- $\sigma(\Delta E)/(\Delta E)$ at level of 2%.

The charge can be identified by crossing the ΔE measurement with TOF or kinetic energy. The mass can be then extracted by momentum and kinetic measurements through the following relations:

$$p = mc\beta\gamma \quad (2.2)$$

$$E_k = mc^2(\gamma - 1) \quad (2.3)$$

$$E_k = \sqrt{p^2c^2 + m^2c^4} - mc^2 \quad (2.4)$$

where $\beta = \frac{v}{c}$ and $\gamma = \frac{1}{\sqrt{1-\beta^2}}$ are derived from the fragment TOF. In the calculation, it must be taken into account the fragmentation contribution due to detector

materials that must be kept as low as possible and eventually subtracted.

In the detector layout different regions can be individuated: the pre-target region (Start Counter+Beam Monitor), the magnetic tracking region and the scintillator and calorimeter region. A schematic view of the experimental setup is shown in Fig.2.3.

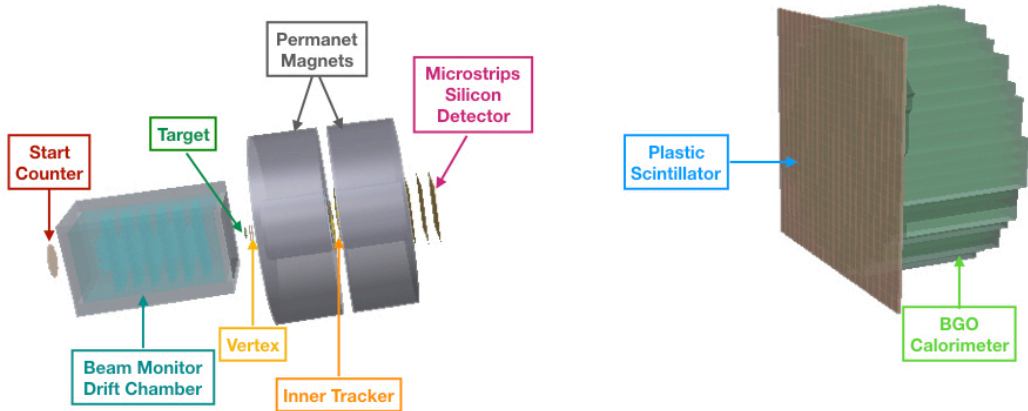


Figure 2.3: Schematic view of the FOOT apparatus and its components [FLAIR geoviewer].

2.5.1 Pre-Target region

The **Start Counter** (SC), placed 20-30 cm upstream of the target, provides the trigger signal to the whole experiment and the measurement of incoming ion flux to be used for the cross section measurement, providing the reference time for all the other detectors and allowing the TOF measurement in combination with the ΔE scintillator detector. Details of the detector are shown in Fig.2.4 (a).

The **Beam Monitor** (BM) is a drift chamber consisting of twelve consecutive layers of wires, with three rectangular drift cells per layer. Planes with wires oriented along x and y axes are alternated to better reconstruct the beam profile. This component will be placed between the SC and the target and it will be used to measure the direction and impinging point of the ion beam on the target, providing the primary particles position and direction. The BM read-out time is fast enough (of the order of 1 μs or less) to ensure that tracks belonging to different events cannot be mixed.

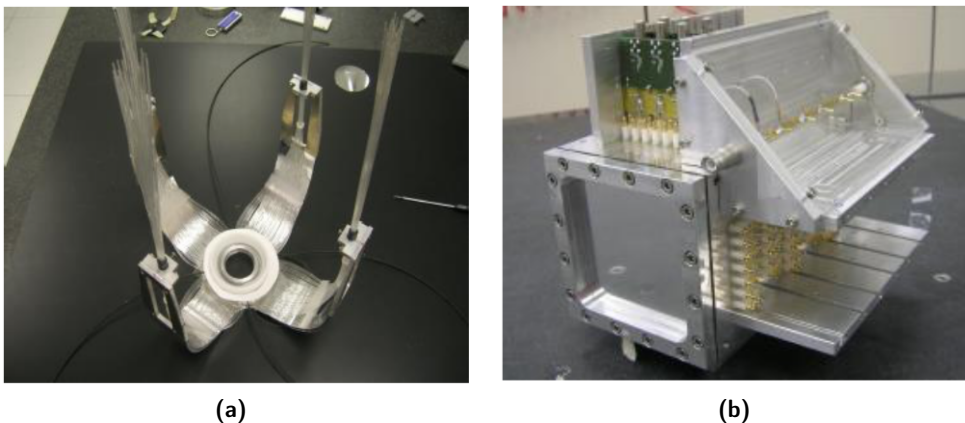


Figure 2.4: (a): Details of the Start Counter: optical fibers are grouped in four different arms. (b): Beam Monitor [41].

2.5.2 Magnetic spectrometer region

The overall tracking system of FOOT is conceived as a magnetic spectrometer consisting of three measuring stations. In between the three stations two permanent magnets provide the required magnetic field. The **Vertex** detector (VTX) consists of four pixeled Silicon detector layers, opportunely disposed (Fig.2.5), that will use as sensing element the M28 chip [42],[43] (from the family of the CMOS Monolithic Active Pixel Sensors, widely used in optical and X-ray imaging). The **Inner Tracking** station foresees two planes of pixeled Silicon sensors to measure both the position of the track in the plane orthogonal to the beam axis and the direction of the track itself. Also in this case M28 sensors will be used, simplifying the need for specific know-how as well as the procurement of the sensors themselves. To minimize the multiple scattering and nucleus re-fragmentation, M28 sensors will be thinned to around $50\ \mu\text{m}$.

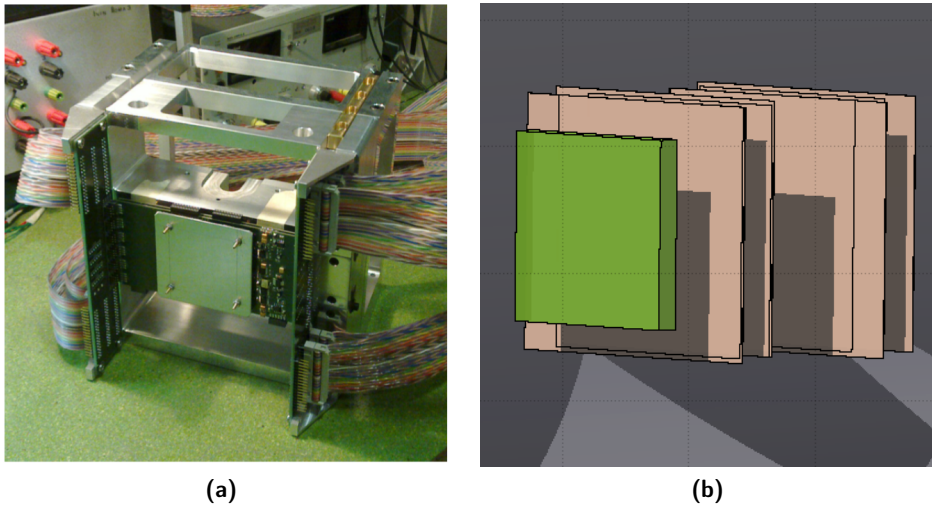


Figure 2.5: Target and Vertex tracker geometrical scheme [41].

The downstream tracking is then carried out by the **Microstrips Silicon Detector**, whose characteristic will be discussed in detail in the Section 2.6.

2.5.3 Scintillator and Calorimeter region

The plastic **Scintillator** will provide the stop to the TOF measurement and the measurement of the energy release ΔE in a thin slab of material to identify the charge of the crossing fragments. It is made of two orthogonal layers, each one made of 20 plastic scintillator rods, to reconstruct the two-dimensional interaction position of the particle in the detector. The total surface of the detector is $40 \times 40\ \text{cm}^2$ which matches the fragments aperture at 1 m distance from the target. The thickness chosen (6 mm) is a trade-off between two opposite trends: a thicker rod will integrate more energy release and more emitted light, so improving the resolution on both ΔE and TOF, but on the other hand a re-fragmentation inside the thicker plastic rod would spoil the dE/dx measurement. The spatial resolution in the two directions is given by the bar section, *i.e.* 20 mm, which matches the calorimeter pixel size. The dE/dx detector prototype (Fig.2.6), currently under investigation, foresees the coupling at both ends of the bars with silicon photomultipliers (SiPM) via optical glue. The number of photo-detectors coupled to each end will be optimized according to the expected performances of the final detector. A preliminary test beam was performed at the Proton Therapy Centre of Trento (Italy) to measure the time and the energy resolution of the scintillator. It has been shown that the energy resolution ranges from 10 to 25%, while a time resolution of 170-180 ns was measured.

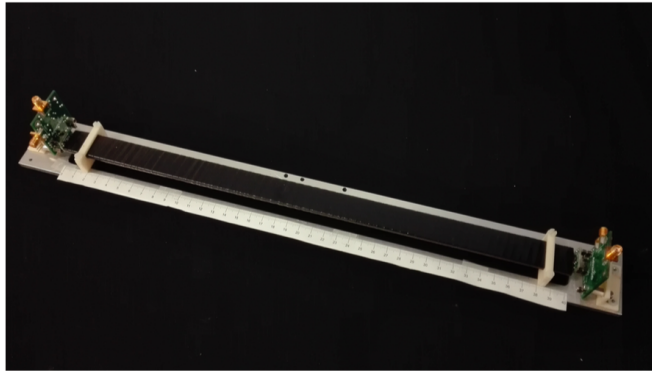


Figure 2.6: Picture of the dE/dx detector prototype [41].

The FOOT **Calorimeter** is the most downstream detector. It is designed to measure the energy of projectile fragments produced in the target. Since FOOT will work at a relatively low beam intensity, the ideal material for a calorimeter is a dense crystal, with high light yield. For these reasons, it has been decided to use BGO crystals. The calorimeter will cover a circular surface of about 20 cm radius.

2.6 Microstrip Silicon Detector

Tracking of fragments downstream the magnetic volumes is essential for the measurement of the momentum and to match the reconstructed tracks with the hits in the TOF scintillator and calorimeter. Also the redundant measurement of dE/dx could be useful to improve the reliability of the experiment. The choice of a Microstrip Silicon Detector (MSD) has been dictated by the need to:

- work as close as possible to the last magnet;
- provide a sufficient spatial resolution for at least 3 (x,y) points;
- minimize the amount of material to reduce the impact of multiple scattering and reduce secondary fragmentations;
- provide precise dE/dx measurements for heavy ions up to 200 MeV/u;
- provide the capability for dE/dx measurements up to 1 GeV/u in order to extend the physics potential of the experiment in the astrophysical domain.

Before the description of the specific Silicon detector geometry conceived for the FOOT setup, a few basic concepts on how a semiconductor detector works will be shown in the following.

2.6.1 Advantages in using semiconductors

In many radiation detection applications, the use of a solid detection medium is of great advantage. Scintillators offer one possibility of providing a solid detection medium, but one of the major limitations of scintillation counters is their relatively poor energy resolution. The energy required to produce one information carrier (a photoelectron) is of the order of 100 eV or more and the number of carriers created in a typical radiation interaction is usually no more than a few thousand. The statistical fluctuations in so small numbers lead to a limitation in the energy resolution. The only way to reduce the statistical limit on energy resolution is to increase the number of information carriers per pulse. In this sense, the use of semiconductor materials as radiation detectors can result in a much larger number of carriers for a given incident radiation.

In addition to a better energy resolution, solid-state detectors offer other desirable features: compact size, the detector dimensions can in fact be kept much smaller than an equivalent gas-filled detector because of the larger densities of solids compared to that one of gaseous substances, relatively fast timing characteristics and an effective thickness that can be varied to match the requirements of the application [44].

2.6.2 Signal formation and acquisition

The above mentioned characteristics that make semiconductors so attractive in radiation detection originate from the properties of the crystalline structure typical of these materials.

While electrons in an isolated atom can only have discrete energy levels, when combined in a lattice, the discrete energy states of the atomic shell broaden to form bands, as shown in Fig.2.7. The *valence band*, corresponds to those outer shell electrons bound to specific lattice sites within the crystal. If excited, these electrons can gain sufficiently energy to move in the *conduction band*, in which they can move freely. These two bands are separated by a region which designates energies that electrons cannot possess. This region is known as *forbidden gap* or *bandgap*, E_g and it is given by the energy difference between the maximum valence band energy, E_v , and the minimum conduction band energy, E_c . For

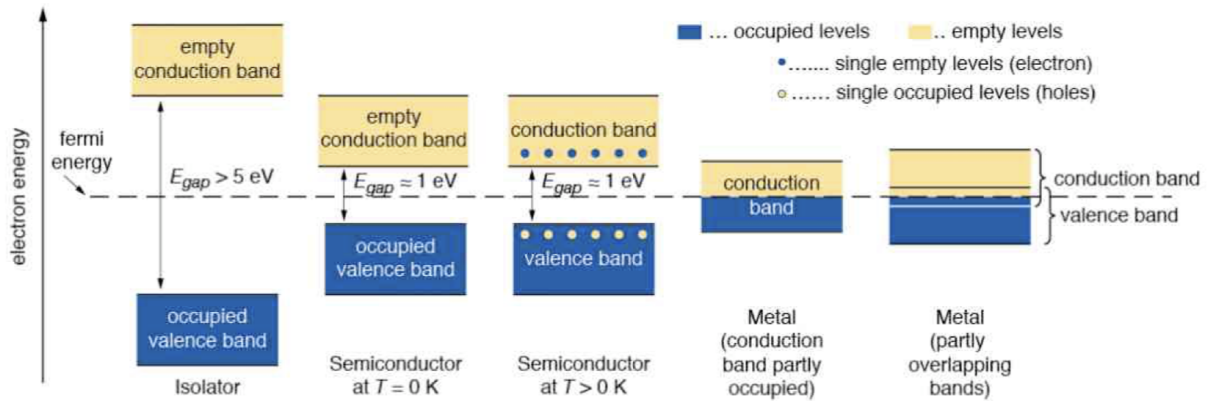


Figure 2.7: Bands structure in insulators, semiconductors and conductors [46].

insulators the valence electrons form strong bonds between neighbouring atoms. These bonds are difficult to break and, consequently, there are no free electrons to participate in current conduction. As can be seen in Fig.2.7, insulators are in fact characterized by a big forbidden energy gap, whereas for conductors the valence and the conduction bands are overlapped. In a semiconductor, bonds between neighbouring atoms are only moderately strong and the bandgap, whose value ranges around 1 eV, is much smaller than that one of insulators in which the forbidden gap can assume values larger than 5 eV.

If enough energy is imparted to a bond by incident radiation, this excites an electron into the conduction band and leaves back a vacant state in the valence band (*hole*). Although the hole appears in the valence band, it can also move by indirect mechanisms. An hole can in fact be filled by an electron from a nearby atom, thereby moving to another position (Fig.2.8).

The motion of electrons and holes can be directed by an electric field. In this sense, holes can be treated as positive charge carriers, just like the electrons are the negative one. Holes tend to move more slowly, since hole transport involves sequential transition probabilities. The semiconductor volume thus acts as an ionization chamber: particles deposit energy in the detection volume, forming

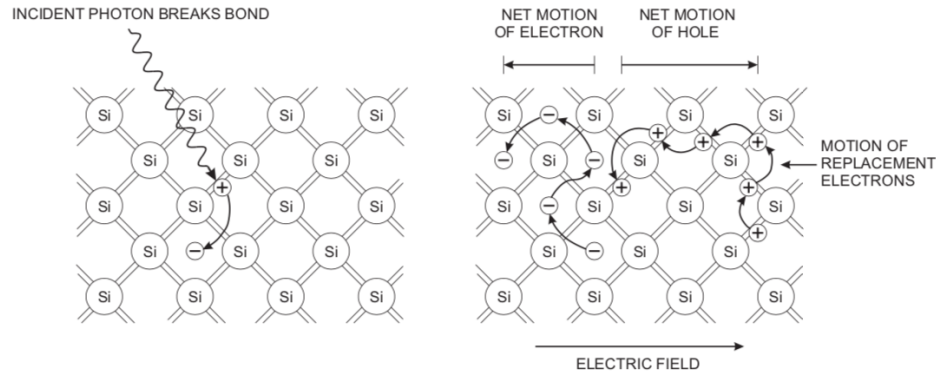


Figure 2.8: Schematic representation of the *electron-hole* pairs motion. An incident particle can break a bond, promoting an electron into the conduction band. The vacant bond with positive net charge can also move due to the presence of neighbouring electrons that will occupy this hole [44].

positive and negative charge carriers; under an applied electric field the charge carriers move and induce a change in induced charge on the electrodes.

The average signal charge is given by [44]:

$$Q_s = \frac{E}{E_i} e \quad (2.5)$$

where E is the absorbed energy, E_i the energy required to form a charge pair and e the electronic elementary charge. The absorbed energy must exceed the band gap to form mobile charge carriers (in Si the gap is equal to 1.12 eV). When all signal charges have reached their respective electrodes, the change in induced charge, *i.e.* the integrated signal current, is Q_s .

The minimum detectable quantum of energy is set by the band gap. In a pure semiconductor, due to the small band gap and due to the thermal excitation, electrons already occupy the conduction band at room temperature. The electrons from the conduction band may also recombine with holes. The thermal equilibrium is then reached between excitation and recombination. When the concentration of electrons and holes (*intrinsic carrier concentration*). From this, one can distinguish insulators from semiconductors: at a temperature of 0 K semiconductors are insulators, but at higher temperatures they have substantial conductivity, depending on the magnitude of the band gap. While the insulators have sufficiently large band gaps so that the concentration of carriers in the conduction band is negligible at all temperatures of interest [12],[44].

2.6.3 The ideal semiconductor detector: Signal-to-Noise Ratio

One of the most important parameter of a detector is the Signal-to-Noise Ratio (SNR). The signal generated in a silicon detector depends essentially only on the thickness of the depletion zone and on the dE/dx of the incident particle. The noise is strictly related to various parameters such as the geometry of the detector and the readout electronics. A good detector should have high SNR. However, this leads to two contradictory requirements:

- Large signal: low ionization energy, that means small band gap;
- Low noise: very few intrinsic charge carriers and so large band gap.

Such conditions can be established by using a reverse-biased *pn* junction. The key to this technology is the introduction of impurities to control the conductivity (*doping*). As we will discuss in the following, in semiconductors the conductivity can be provided by either electrons (*n*-type) or holes (*p*-type).

n-type doping

To illustrate the effect of doping on semiconductor properties, we consider crystalline Silicon as an example. Replacing a Si atom (group 4 in the periodic table, *i.e.* 4 valence electrons) by an atom with five valence electrons, such as a Phosphorus (P) atom, leaves one valence electron without a partner. Since the impurity contributes an excess electron to the lattice, it is called *donor*. This extra electron remains only very lightly bound to the original impurity site and it will move to the conduction band without a corresponding hole (Fig.2.9). The energy spacing between these donor levels and the conduction band is sufficiently small (0.0005 eV) so that the probability of thermal excitation is high enough to ensure that a large fraction of the donor impurities are ionized.

The net effect in *n*-type material is therefore to create a situation in which the number of conduction electrons is much greater than the number of holes and the number of holes much smaller than in the pure material. As a result, at room temperature most electrons are raised to the conduction band and the probability of ionization is high (Fig.2.9).

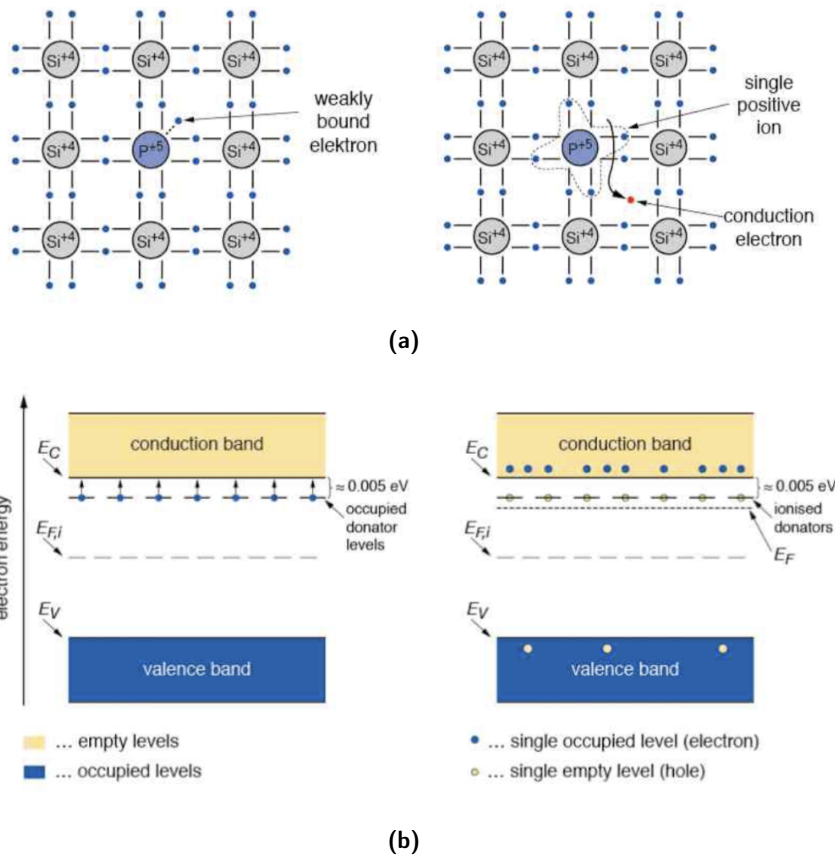


Figure 2.9: *n*-type doping in a crystalline silicon [46].

p-type doping

Consider again the crystalline Silicon. Introducing a trivalent impurity, such as Boron (B), into a lattice site provides bonds for 3 Si valence electrons, but leaves one impurity valence electron without a partner (Fig.2.10). This vacancy represents a hole similar to that left behind when a normal valence electron is excited to the conduction band, but its energy characteristics are slightly different. If an electron is captured to fill this vacancy, it participates in a covalent bond that is not identical to the bulk of the crystal because one of the two participating atoms is a trivalent impurity. An electron filling this hole, although it is still bound

to a specific location, is slightly less firmly attached than a typical valence electron. These *acceptor* impurities create electron sites within the normally forbidden gap, introducing a bound state close to the valence band (Fig.2.10).

As a result, the electron missing to the valence band, form mobile positive charge states which behave similarly to an electron in the conduction band, *i.e.* they can move freely throughout the crystal.

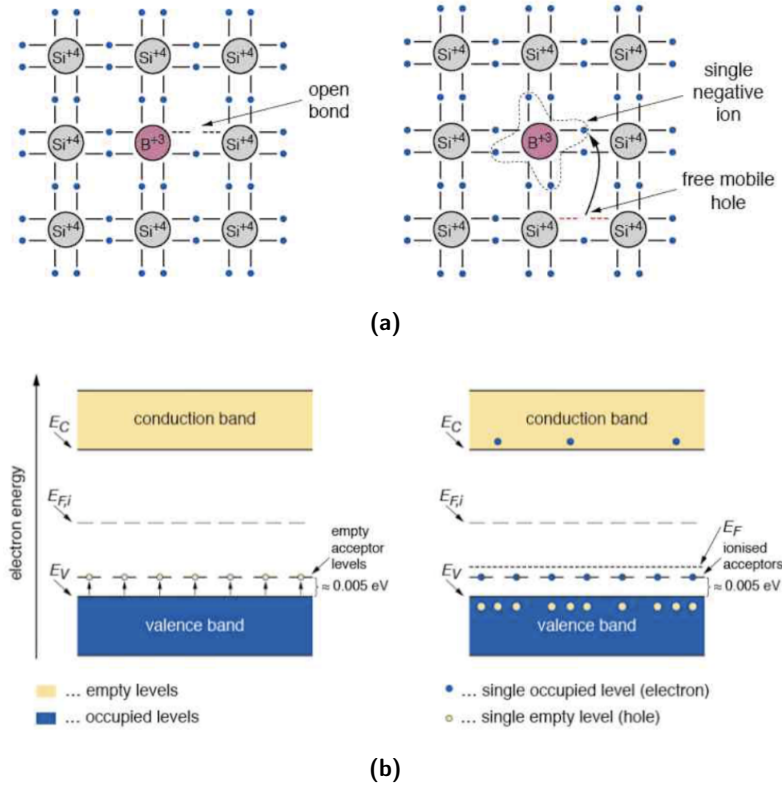


Figure 2.10: *p*-type doping in a crystalline silicon [46].

p-n junction and reverse biasing

When *p*-type and *n*-type materials are placed in contact with each other, the junction behaves very differently than either type of material alone. The *n*-type material electrons diffuse across the junction combining with holes in *p*-type material. Filling a hole makes a negative ion and leaves behind a positive ion on the *n*-side. A space charge builds up, creating a *depletion region* with a contact potential. Since the depletion region is a volume devoid of mobile carriers, it forms a capacitor, where the undepleted *p* and *n* regions are the electrodes and the depletion region is the dielectric. An applied voltage V , with the indicated polarity in Fig.2.11 further prevents electrons to flow across the junction. A reverse voltage therefore drives the electrons away from the junction suppressing the diffusion effect. The depletion zone becomes in this way larger and its width is given by [45]:

$$w_{depl} = \sqrt{2r\epsilon\mu r V_{bias}} \quad (2.6)$$

where μ is the mobility of the majority carriers (electrons in case of *n*-type bulk), r the resistivity of the bulk material and V_{bias} the bias voltage. Increasing V_{bias} will increase the depleted volume in the bulk and therefore the region in which a particle might be detected.

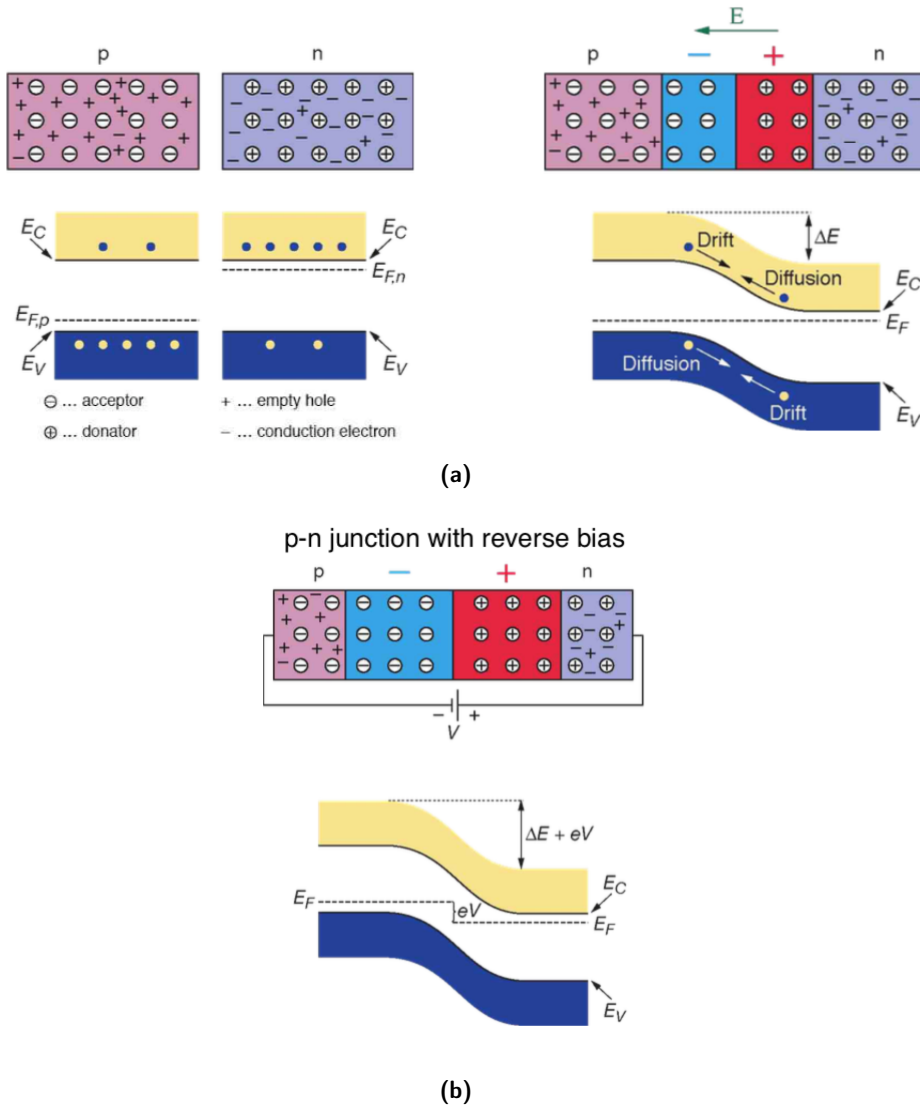


Figure 2.11: (a) p - n junction [46]. (b) Reverse biasing [46].

2.6.4 Strip detectors: configuration and working principle

The detector electrodes can be then segmented to form strips or pixels. A strip detector is an arrangement of strips acting as charge collecting electrodes. Placed on a low doped fully depleted silicon wafer, these implants form a one-dimensional array of diodes. By connecting each of the metalized strips to a charge amplifier, a position sensitive detector is built. Two dimensional position measurements can be achieved by applying an additional strip like doping on the wafer backside by use of a double sided technology. The principle of operation of a silicon strip detector is shown Fig.2.12.

The Si bulk is lightly n -doped and the junction is formed by highly doped p^+ strips and the n^+ backplane. Each strip forms a pn -diode. The backplane is highly doped in the same manner as the bulk (n^+ type in this case). In the bulk between the two electrodes an electric field is present due to the applied voltage. If an ionizing particle traverses the detector, an equal number of free electrons and holes is produced. The electric field causes the charges to travel towards the respective electrodes. A signal is induced on the electrodes as soon as the charges start to move and it is then amplified by an amplifier connected to each strip [45].

The position of the strip that collects the charge determines the position of the incident particle. The capability to distinguish particles that are very close

to each other depends on the strip pitch. the resolution is therefore given by [44]:

$$\sigma^2 = \int_{-p/2}^{p/2} \frac{x^2}{p} dx = \frac{p^2}{12} \quad (2.7)$$

where p is the strip pitch. The root mean square resolution is therefore the strip pitch divided by $\sqrt{12}$.

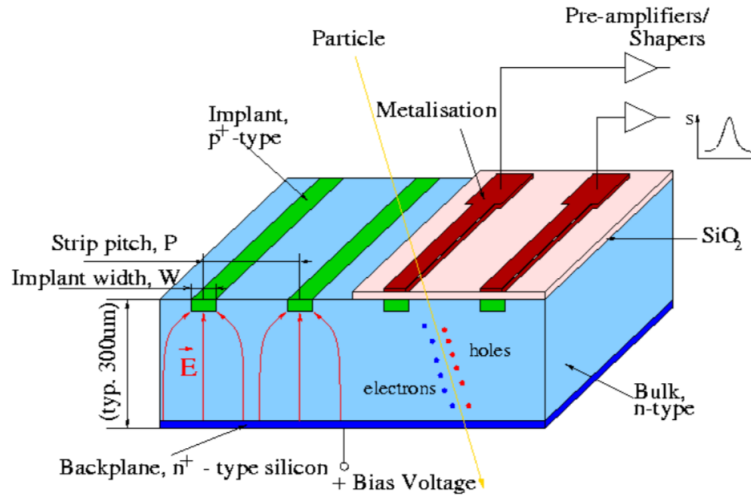


Figure 2.12: Schematic configuration of a Silicon strip detector [45].

2.6.5 The Microstrip Silicon Detector for FOOT

The use of a Silicon detector is a recent modification of the first design of the experimental setup, that goes back to June 2017. The Microstrips Silicon Detector (MSD) of the FOOT apparatus will be placed just after the second magnet. It will consist of a series of Silicon planes disposed along the beam line. Each plane is made by strips for each view oriented perpendicularly with respect to the beam direction. The details of each plane are still under investigation, in order to individuate an appropriate layout that ensures the required spatial resolution, minimizing multiple scattering and fragmentation events.

As a first proposal, it has been foreseen the use of two Silicon layers thinned down to $70 \mu\text{m}$ each one, glued together using a $30 \mu\text{m}$ thick bi-adhesive kapton foil, giving an equivalent thickness of around $155 \mu\text{m}$. At the present another solution that foresees a single $150 \mu\text{m}$ thick Si layer has been proposed. The two independent layers solution with respect to the one with a single layer will ensure two independent dE/dx measurements and more rigid mechanical behavior. The front-end hybrids, hosting the readout chips, will be glued at one side of each silicon module (Fig.2.13) minimizing the dead space in the beam region. In this case, the use of two thin Si layers leads to a smaller signal production with respect to the case in which a single thicker Si layer is adopted. To compensate for this smaller signal, the on strip amplification mechanism guaranteed by the Low Gain Avalanche Diode (LGAD) mechanism will be implemented.

The Low Gain Avalanche Diode working principle lies in the Avalanche Photo Diodes, where a region with high electric fields ($>200 \text{ kV/cm}$) provides the charge multiplication mechanism. LGAD are produced using a p-type multiplication layer, with an n^+ type electrode. The p diffusion under the cathode enhance the electric field, as shown in Fig.2.13. Typical structure is shown in Fig. 2.13, it is composed by the n^+ electrode, the p multiplication layer, that represents the avalanche region, and the p^+ electrode. The signal is due electron and holes drifting from creation point to collecting electrodes: electrons travel a short path to

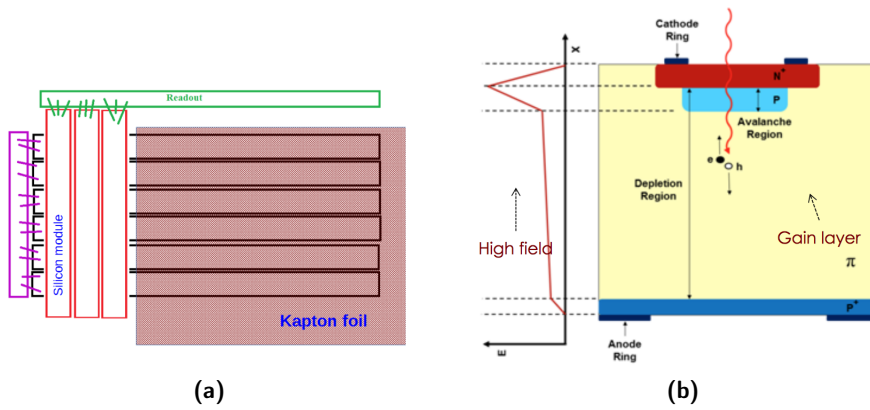


Figure 2.13: (a) Conceptual sketch of x-y plane: $70\ \mu\text{m}$ planes glued a $30\ \mu\text{m}$ kapton foil. Electronic front-end is at the periphery of the planes. (b) LGAD working principle: $n^+/p/p^+$ doping structure is shown. Main signal is due to holes moving towards p^+ electrode [41].

reach the n^+ electrode, while holes traverse the entire device thickness to reach the p^+ electrode and they give the main contribution to the signal. A scientific collaboration with N. Cartiglia research group (Torino) has been already established to study the behavior of thinned silicon sensors with LGAD amplification mechanism when traversed by heavy fragments. However, up to now the prototypes with LGAD mechanism have been produced by FBK (Trento).

2.7 Test Beam in Trento

On December 2017, a test beam has been carried out in the Trento Proton Therapy Centre. The experimental devices used for such test included a model of strip detector. In this section, after a brief description of the Trento facility, the characteristics of this specific detector and its performances will be presented.

The Trento Proton Therapy Centre, which is part of the Trentino Healthcare Agency, started clinical operations in October 2014. As shown in Fig.2.14, a cyclotron serves two medical treatment rooms both equipped with rotating gantries. The centre is also equipped with an experimental area, where the beam line is split in two branches, both dedicated to scientific applications, including medical physics and detector testing.

The beam is available in the experimental room outside clinical hours and all activities are supervised by the Trento Institute for Fundamental Physics and Applications (TIFPA), which is part of the Italian National Institute for Nuclear Physics (INFN). The cyclotron accelerates the beam up to a maximum of 228 MeV. After the cyclotron exit, a rotating degrader of different thicknesses and materials allows to reduce the beam energy down to its minimum value of 70 MeV. The beam cannot be shared simultaneously among the different rooms (treatment rooms or experimental room) and can only be requested alternatively [48]. The experimental area consists of two different spaces: a preparation room and the irradiation cave. This last one is equipped with a control station, in order to monitor via remote control cameras the activities inside the room. The connection between the two rooms is made possible by a patch panel that allows the electronics installation for the data acquisition.

The two branches of the main beam line have different characteristics, according to the specific needs of the experiment. In particular, the branch on the right in Fig.2.15, is characterized by a narrow spot. At this line, a pencil beam is available with the possibility of a further energy reduction (below 70 MeV)

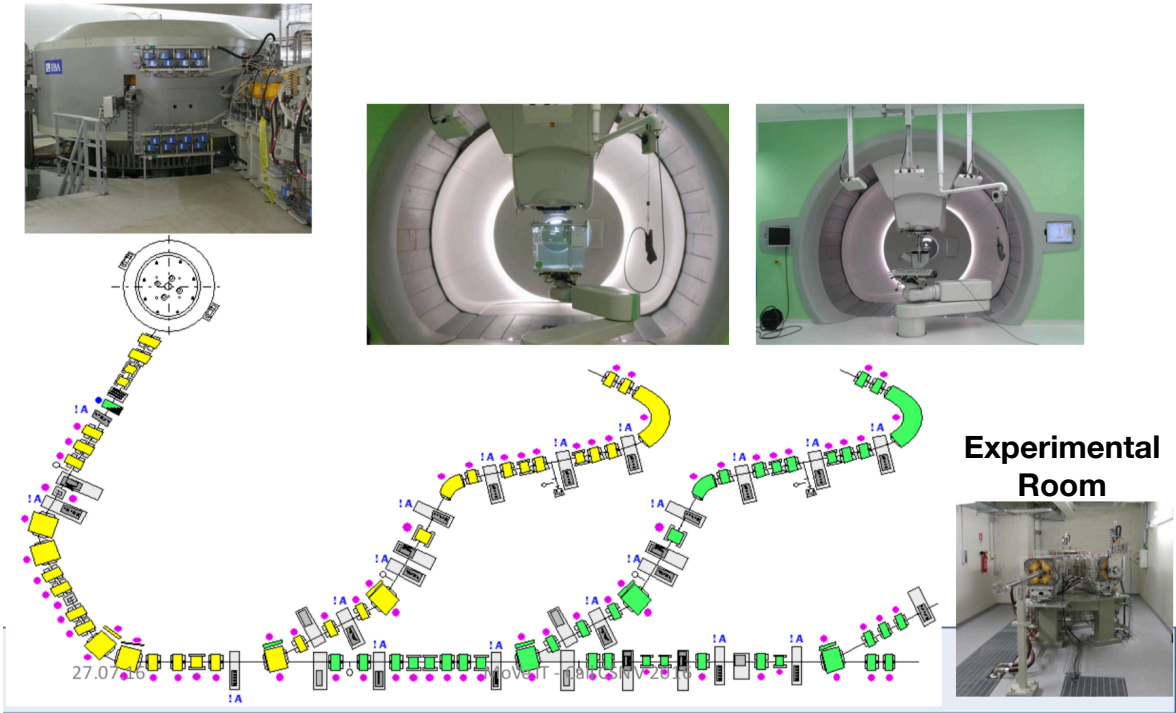


Figure 2.14: Trento Proton Therapy Centre layout [49].



Figure 2.15: Experimental room at Trento Proton Therapy Centre [49].

thanks to the use of dedicated in-air degraders. Lasers are also available for the target alignment at 1.25 m from the exit window, which is defined as the isocenter, in analogy to the treatment rooms. As shown in Fig.2.16, the test beam of December 2017 has been carried out exploiting properties of this beam sub-line.

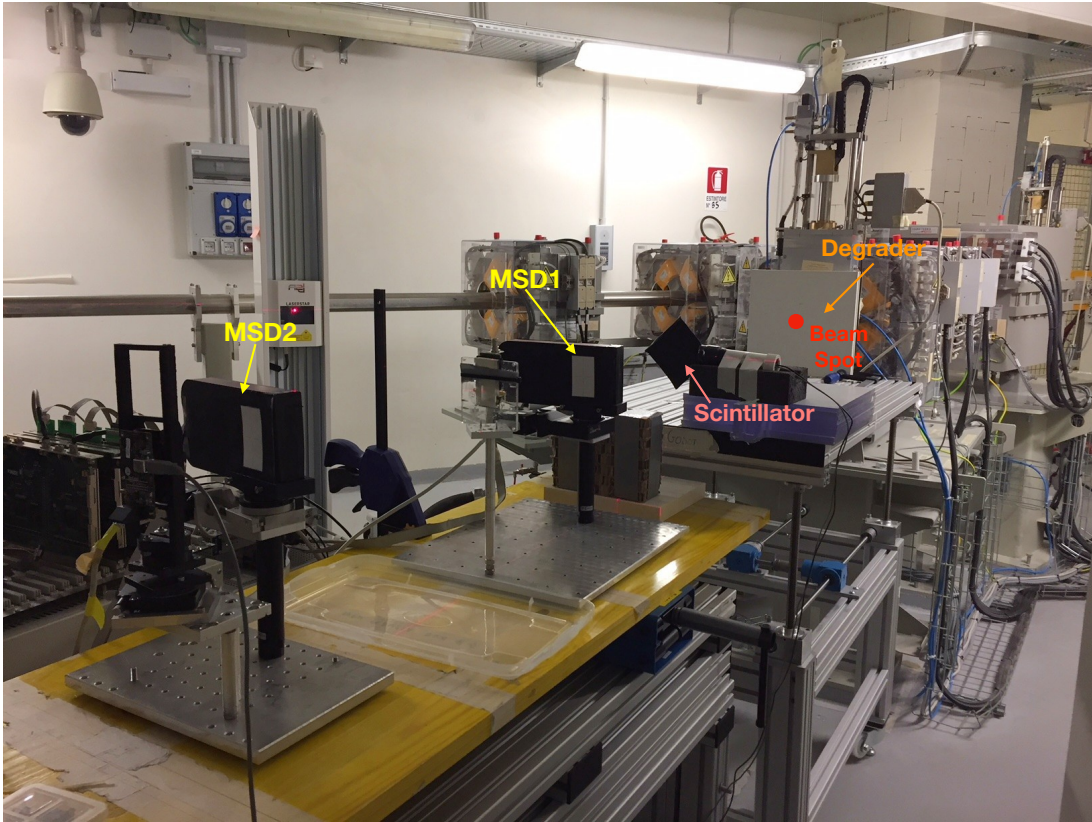


Figure 2.16: Experimental setup in the irradiation room of the Trento Proton Therapy Centre. Test beam of December 2017.

Table 2.1: Strip detector characteristics.

| Detector Characteristics | |
|-----------------------------|-----------------------------|
| Surface | $4 \times 7 \text{ cm}^2$ |
| Thickness | $300 \text{ } \mu\text{m}$ |
| No. strips (S side) | 2568 |
| Strip pitch (S side) | $27.5 \text{ } \mu\text{m}$ |
| No. readout strips (S side) | 640 |
| Readout pitch (S side) | $110 \text{ } \mu\text{m}$ |
| No. strips (K side) | 384 |
| Strip pitch (K side) | $104 \text{ } \mu\text{m}$ |
| No. readout strips (K side) | 384 |

Two Silicon strip detectors, with identical characteristics, have been used. They have been displaced at two different positions: one detector has been placed at the isocentre (MSD1 in Fig.2.16) and the other one 50 cm beyond the isocentre (MSD2 in Fig.2.16). The used Silicon sensors have different characteristics with respect to the configurations foreseen for the FOOT setup. However, it is useful to show their performances to better understand the potential of this kind of detectors. In Fig.2.17 a schematic representation of the detector configuration is shown. In particular, it is illustrated the tracker detector used for the AMS-02 experiment [47], that differs from that one used in the test beam just in the num-

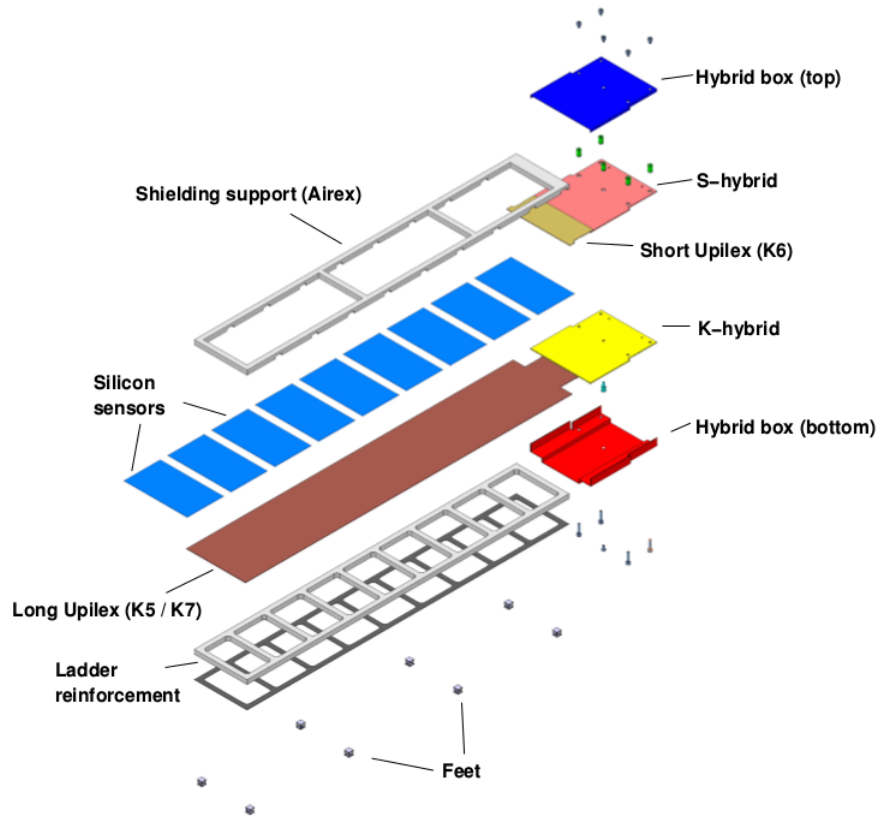


Figure 2.17: Schematic representation of the adopted strip detector for the test beam in Trento [47].

ber of sensors. In Trento just one Silicon sensor has been used (Fig.2.18 (b)). The characteristics of the detector are resumed in Tab.2.1. The data has been taken for different energies of the beam (70 MeV, 112 MeV, 159 MeV, 228 MeV). An example of the reconstructed beam profile is shown in Fig.2.19 and Fig.2.20. Position A indicates the isocentre, while the detector placed 50 cm beyond the isocentre is identified with Position B. As shown, the detector allows to reconstruct both X and Y coordinates of the beam, allowing a precise beam profile reconstruction.

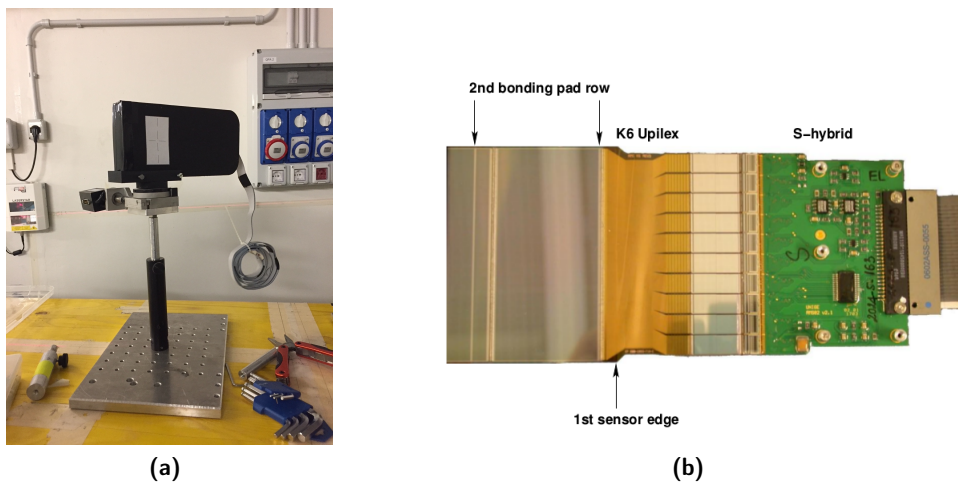
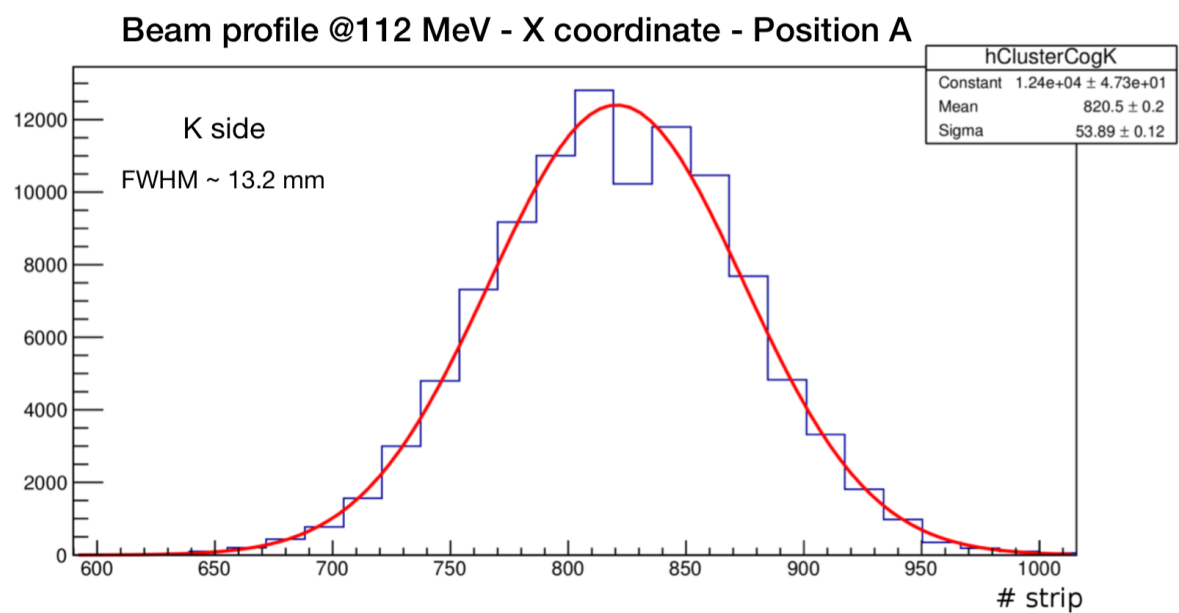
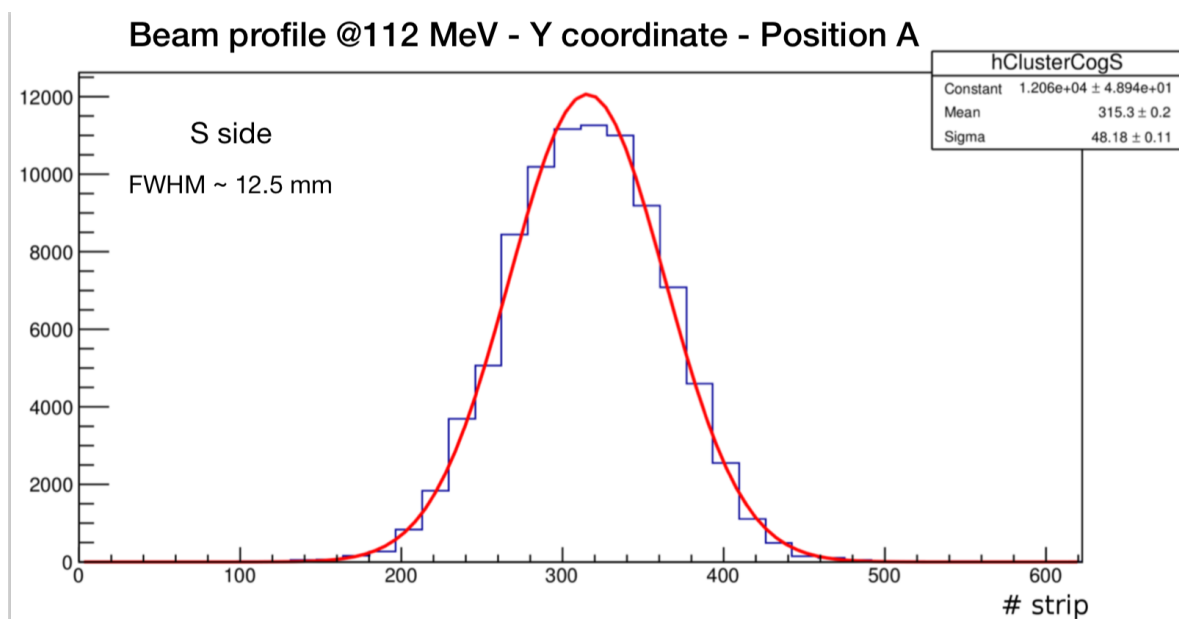


Figure 2.18: Details of strip detector used in the test beam in Trento facility. (a): the support structure of the Silicon sensor. It is able to rotate, allowing measurements from different angles. (b) [47] Details of the Silicon sensor and of the electronic readout.

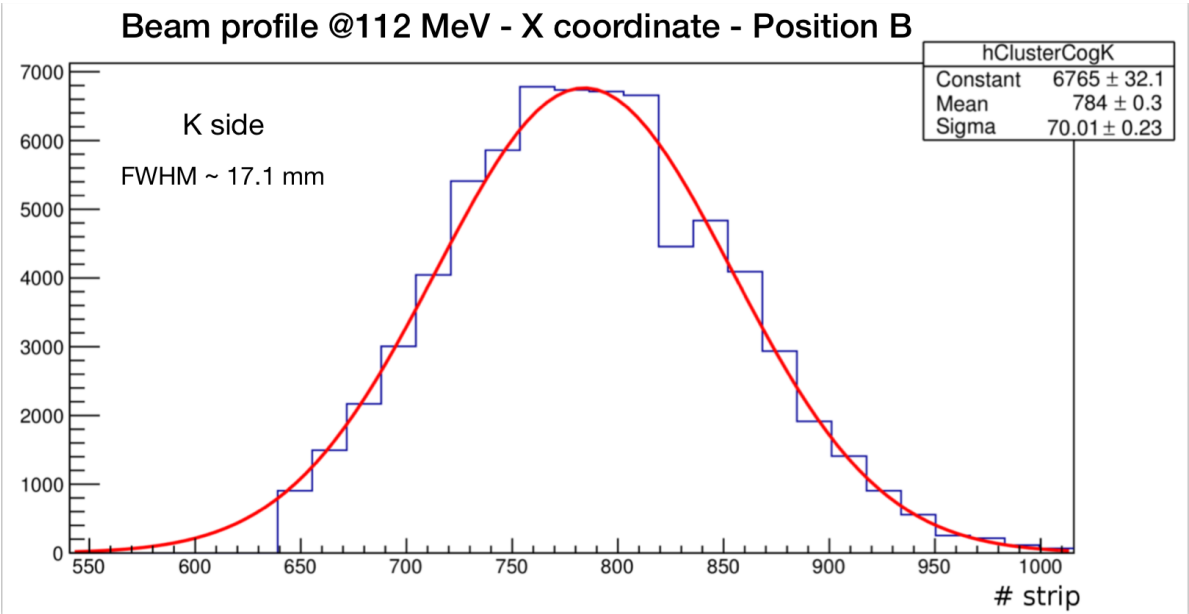


(a)

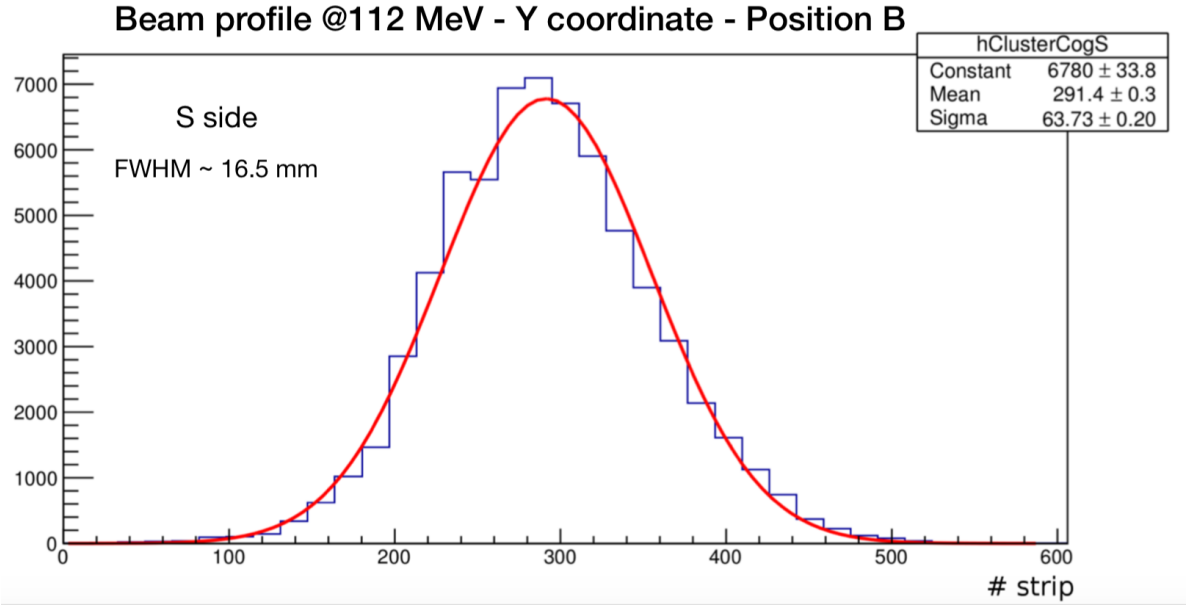


(b)

Figure 2.19: Reconstructed beam profile at the isocentre by means of Silicon strip detector (MSD1).



(a)



(b)

Figure 2.20: Reconstructed beam profile 50 cm beyond the isocentre by means of Silicon strip detector (MSD2).

Chapter 3

Simulation and reconstruction software

Software plays a fundamental role in the FOOT experiment. At present, the most important software components are those concerning the simulation of the experiment and the data analysis. In Section 3.1 an overview of the FLUKA Monte Carlo simulation package is introduced, describing the physical models that are adopted in the codes. A brief description of the basic input required from the software is presented in Section 3.2, followed by a presentation about its capability of building very complex geometries by means of a Combinatorial Geometry package (Section 3.3). The software framework for the FOOT experiment data reconstruction is finally described in Section 3.4.

3.1 FLUKA Monte Carlo simulation code

FLUKA is an advanced Monte Carlo simulation package for the calculation of particle transport and interactions with matter, developed from the collaboration of INFN and CERN [54],[43],[51]. The code has been robustly tested through comparison with many experimental data and now it covers a wide range of applications, from high energy experimental physics to detector design as well as medical physics. It is able to simulate with high accuracy the interaction and propagation in matter of about 60 different particles, covering an energy range that goes from keV to TeV.

The history of FLUKA spans more than 40 years, from the first version, whose origin goes back to '70s, up to the current version, whose main authors are A. Ferrari, A. Fassò, J. Ranft and P. R. Sala [41]. Each new version represented not only an improvement of the existing program, but rather a “jump” in the code physics, design and goals. The recent addition of the simulation of heavy ion interactions, allowed to extend the application of such tool also to hadrontherapy studies.

Charged particle transport is modeled in FLUKA through a multiple Coulomb scattering algorithm [54] based on Molière theory and supplemented by an optional single scattering method. Ionization energy losses are based on statistical approach, including δ ray emission and energy straggling. Hadron-nucleus interactions are modeled by means of the PENAUT (Pre-Equilibrium Approach to NUClear Thermalization) model, which simulate the two first stages of nuclear interactions described in Section 1.2.6. On the other hand, nucleus-nucleus reactions are modeled through interfaces to event generators, which simulate the dynamic stages of the nucleus-nucleus interaction as a function of the energy range [50]. For initial ion energies up to 100 MeV/u, the Boltzmann Master Equation

(BME) approach is followed, while up to 5 GeV/u fragmentation events are described by the relativistic Quantum Molecular Dynamics (rQDM) theory [53] and at higher energies a Dual Parton Model [55] developed by FLUKA authors is used. However, these last two models deal with energies that are not relevant for hadrontherapy application.

The BME model is based on a set of time-dependent transport equations that aims to describe the evolution of the system towards the equilibrium state, through a sequence of two-body interactions and emission of unbounded particles (neutrons and protons) and clusters (heavy/light nuclei).

The rQDM model describes the interaction of two nuclei starting from their initial state, following the propagation of each nucleon in the potential generated by all other nucleons according to a quantum mechanical formalism.

These models are then coupled to the internal FLUKA models for the de-excitation phase of the interaction (evaporation, fission, Fermi breakup, γ emission).

3.2 FLUKA input

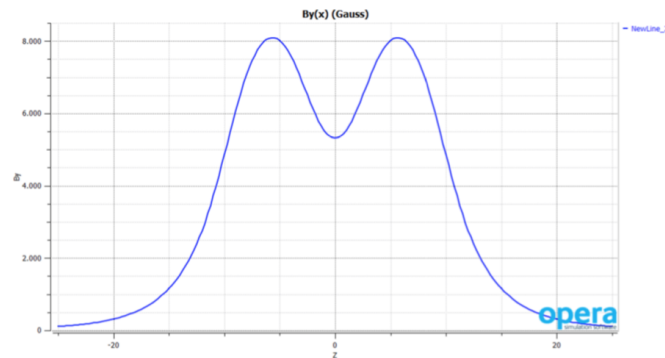
The starting point for the development of a simulation is the definition of all the information required from the software for the data processing (*input*). A FLUKA input consists of a series of standard commands or *cards*, each one with a specific function. The main cards that compose a basic input are listed in the following:

- **DEFAULTS**: selects predefined physics settings, for example transport thresholds.
- **BEAM** and **BEAMPOS**: define beam properties and beam position and direction.
- **GEOMETRY**: defines the geometry.
- **MATERIAL** and **ASSIGNMA**: define the materials and their assignment to the different regions. FLUKA handles different materials and compounds, that can also be defined by the user.
- **RANDOMIZ**, **START** and **STOP**: initialize the *seed* for the generation of random numbers and the number of primaries, and declares the end of the program.

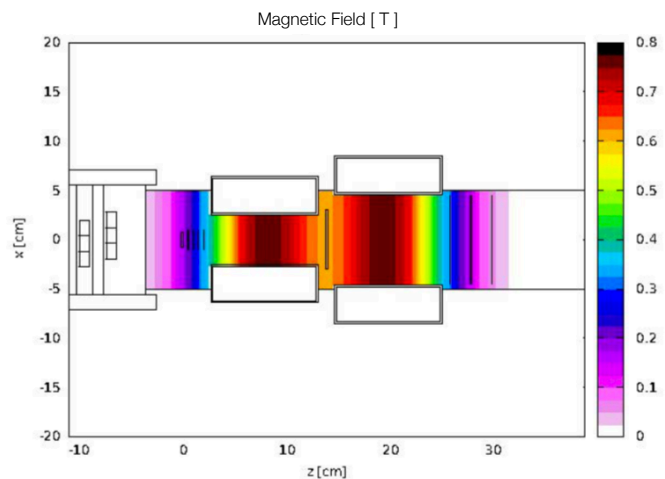
As previously discussed, FLUKA physical models are fully integrated in the code and they are not modifiable. However, a set of user interface routines, written in Fortran77, can be used to customize the software, in order to overcome the limitations given by the use of the standard cards and score other quantities of interest. As an example, the user routine adopted to integrate a 3D magnetic field map in the FOOT electronic detector setup can be mentioned. The map is stored in an ASCII file containing the three magnetic field components correspondent to a grid of 3D points. At present, an approximated field map with B along the y direction has been adopted (B_x and B_z null). The engineers responsible for the construction of the magnets, provided a magnetic field map for one single magnet. According to the Gaussian shape of the magnetic field derived from this map, B_y is calculated as a sum of two Gaussian functions, as shown in Fig.3.1(a). In order to include the effect of the magnetic field on the evaluation of the particle trajectory, a “magnetic region” has been defined in the setup geometry, as shown in Fig.3.2 (b). Thanks to the above mentioned routine it has been possible to combine the magnetic map and the geometry layout (Fig.3.1(b)).

For a simplified management of the different cards, the FLuka Advanced Interface (FLAIR) can be used. It is a graphical interface that allows the interactive

visualization of the geometry as well as the compilation, running and plotting of the results. In Fig.3.2 (a) a typical input visualization with FLAIR is shown, Fig.3.2 (b) and (c) shows the geometry visualization and the run panel respectively.



(a)



(b)

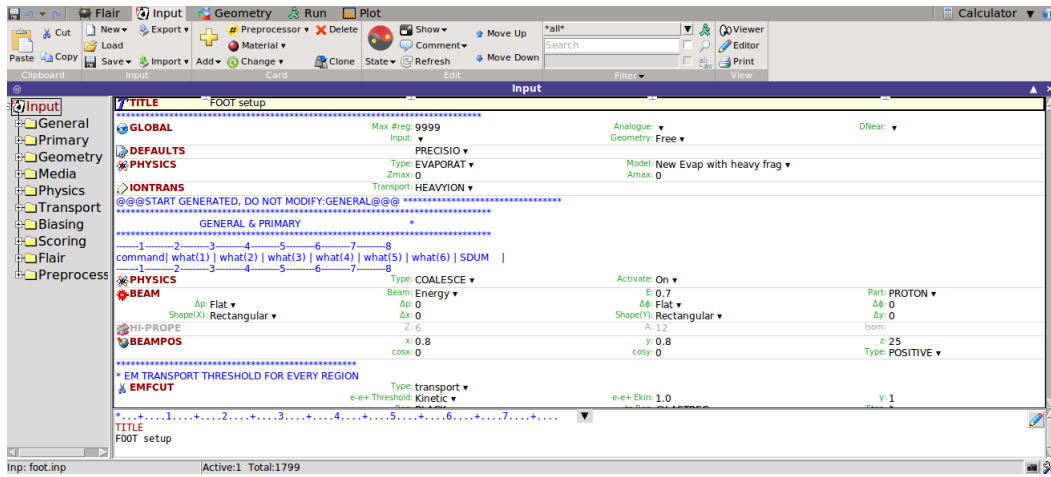
Figure 3.1: Example of *ad hoc* user routine for FOOT electronic setup. (a) Adopted magnetic field component B_y ; the mean coincides with the magnets center. (b) Example of how FLUKA integrates the field map in the simulation: the picture shows the magnetic field intensity [41].

3.3 FLUKA combinatorial geometry

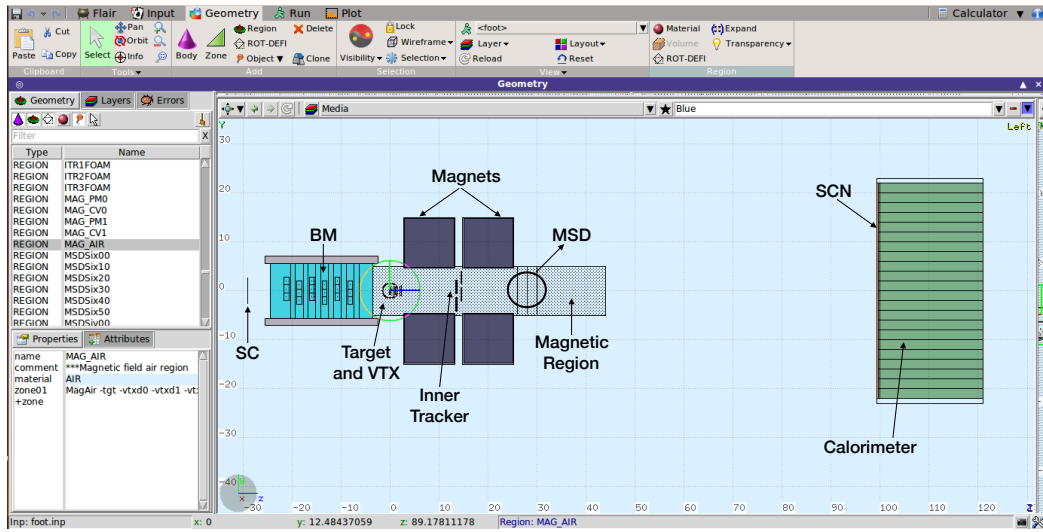
The FLUKA geometry is a part of the code where accuracy and flexibility are combined to give very effective results. To construct a new geometry, the input sequence must be contained between a `GEOBEGIN` and a `GEOEND` card.

The fundamental concept that characterizes the Combinatorial Geometry in FLUKA is the definition of *bodies* and *regions*. Bodies are defined either as finite portions of space (spheres, cubes, etc.) or as infinite planes and cylinders. The use of such infinite bodies makes the geometry construction much easier and less error-prone. Regions are then defined as combinations of bodies obtained by boolean operation: union, subtraction and intersection (Tab.3.1). Once the region volume has been defined, it is possible assign the material of interest choosing from pre-defined materials available in the software or defining new compounds by means of the `MATERIAL` and the `COMPOUND` cards. An example of bodies and region definitions is shown in Fig.3.3.

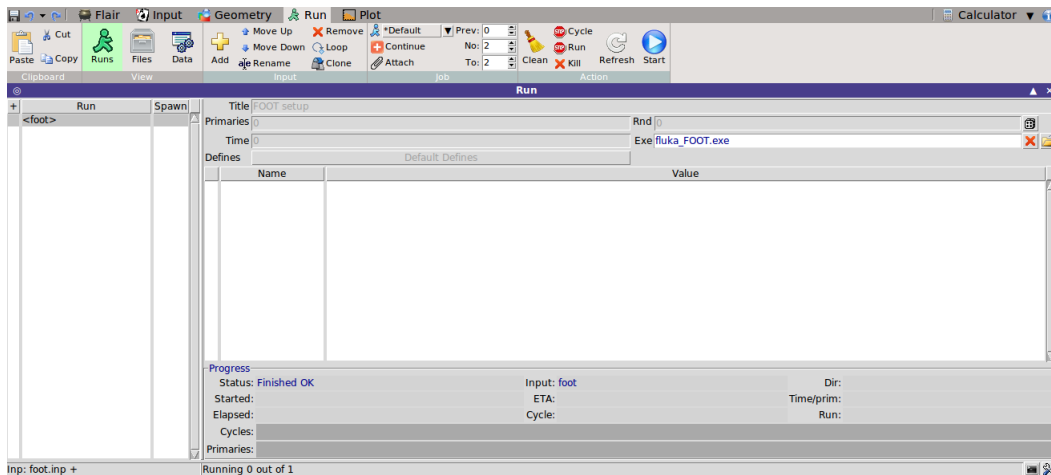
Because the tracing routines cannot track across the outermost boundary, all the regions must be contained within a surrounding “blackhole”, which is an



(a)



(b)



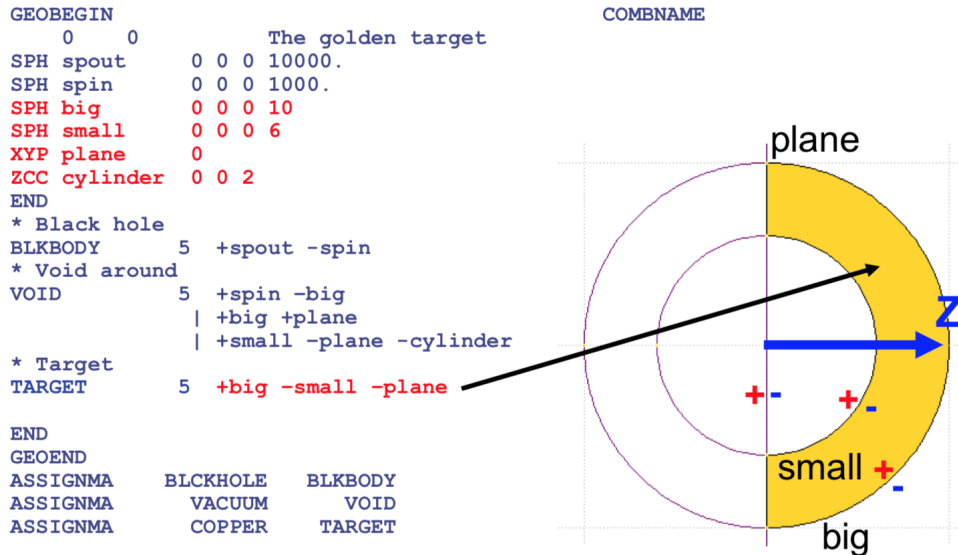
(c)

Figure 3.2: Typical FLAIR interface. (a): a FLUKA input, visualized with the graphical interface; the various cards are distinguishable. (b): FLAIR visualization of the FOOT geometry. (c): typical run panel in the FLAIR interface.

imaginary infinitely absorbing material. Thus, all particles escaping from the defined geometry are absorbed and their simulation stop [50].

Table 3.1: Boolean operations for FLUKA combinatorial geometry.

| Math | Operation | FLUKA |
|--------|--------------|-------|
| \cup | Union | |
| \cap | Intersection | + |
| - | Subtraction | - |

**Figure 3.3:** Example of FLUKA combinatorial geometry: regions are defined as combination of bodies by means of boolean operators [50].

In FLUKA each primary particle and its subsequent history constitutes an *event*. Once all the required input parameters are set, the MC code starts to simulate event per event the evolution of the primary particle and the other eventually produced particles. At the end of the simulation the output file is provided.

The FOOT simulation output is an ASCII file which stores event by event information about all the generated particles and their interactions with the detectors. This ASCII file is then converted into a ROOT file by a portable code, in order to store the information in a way that can be easily read by the reconstruction algorithm. In particular, data are stored in a Tree structure that includes three main blocks of information:

- Particle block: it stores the kinematic information for every produced particle (e.g. charge, mass)
- Detector block: it stores information about the specific detector (e.g. energy release in the detector, TOF)
- Crossing block: it stores information about the particles when they cross the different regions defined in the FLUKA geometry card (e.g. particle momentum at the crossing position)

3.4 Event Reconstruction

In the FOOT experiment, the full reconstruction chain, for both data and simulated events, is performed by a dedicated software called SHOE (Software for

Hadrontherapy Optimization Experiment). It is a ROOT based framework, developed in the GSI laboratory (Germany). Since the event reconstruction involves the handling of the input and output data from different detectors, SHOE builds in two main steps all the necessary input information to perform the event reconstruction:

- **Level 0**

The first step of the reconstruction code consists in reading, interpreting and converting in a single software-object form both data and simulation events provided in different output formats. The signals collected during the data acquisition runs are decoded, the detector dependent calibration constants are applied and the output of each detector is organized in *Hit*, *Cluster* and *Track* objects, whose definition and additional information will depend on the detector type. The track reconstruction allows to obtain the required information about the momentum, the energy as well as the time of flight of the particles.

- **High Level**

In the second step the data obtained from the different sub-detector units (*e.g.* Beam Monitor, Tracking System, Scintillator and Calorimeter) are combined, achieving the final global event reconstruction. The different fragments, together with the incoming beam particle, will be identified providing all the necessary input for the cross section calculation.

Details of the structure of the reconstruction code are illustrated in Fig.3.4.

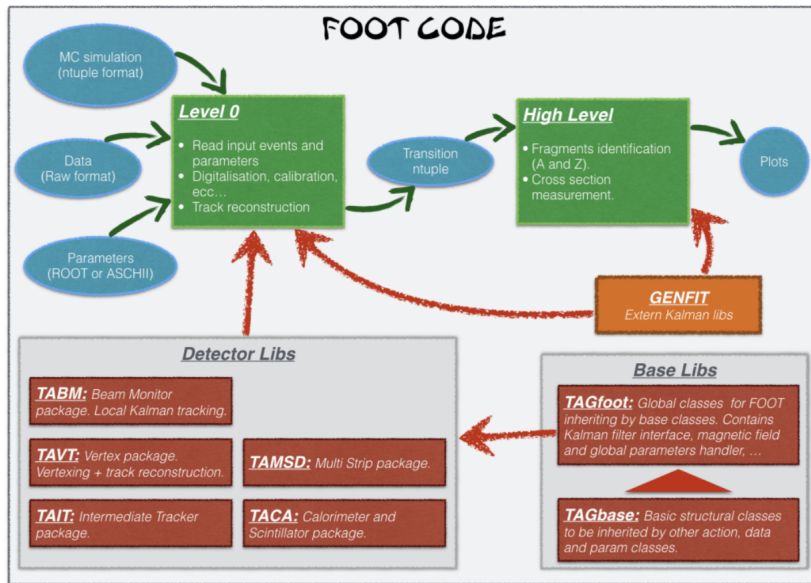


Figure 3.4: SHOE code structure [41].

The SHOE code is fully interfaced with GENFIT software, which is an experiment. independent framework for particle track reconstruction and nuclear physics [52]. GENFIT is based on a kalman filter algorithm and it is included in the SHOE code in order to provide two different track reconstructions. A projectile reconstruction is performed using the Beam Monitor hits alone. A global track reconstruction of fragments is done combining hits from Vertex, Inner Tracker and Microstrip Detectors. The matching with the hits detected in the scintillator and the clusters in the calorimeter will be made on the basis of the extrapolation performed using the track information at the exit point from the Microstrip Detector. The information about the incoming beam direction will be instead provided by the beam monitor detector and will be used for the inverse kinematic calculations.

Chapter 4

Simulation results

In this Chapter, the results obtained from the analysis of the Microstrip Silicon Detector (MSD) simulated data will be described. Firstly, the details of the four detector configurations will be introduced in Section 4.1, showing all the chosen parameters for the FLUKA Monte Carlo simulations. The Section 4.2 shows the study about the energy loss measurement performance of the MSD, which is performed comparing the energy distributions of different particles that hit the detector. Then, the effect of multiple scattering phenomenon has been analysed in Section 4.3, evaluating the deflection angle and showing its role in the track reconstruction phase. A comparison between the investigated configurations follows. Finally, a fragmentation analysis it is also required. For this purpose, as will be shown in Section 4.4, the fragmentation probability in each single plane has been evaluated.

4.1 Microstrip Detector configurations

Although the first results have already show the efficiency of the strip detector, many other parameters have to be investigated. Considering then the introduction of this type of detector in the FOOT experimental setup is a recent modification, there are not enough available data to estimate its performances. It is therefore necessary to rely upon simulations, in order to find to find an appropriate MSD layout that satisfies the discussed experimental requirements (Section 2.6). The analysis has been implemented with Monte Carlo (MC) simulations and in particular the FLUKA MC code has been chosen, as it is widely used in hadrontherapy (and in particular at CNAO ed Heidelberg therapy centers) since it is considered of high reliability in this kind of application.

Four different configurations have been analysed and compared, varying in particular the following parameters:

- composition of each plane, in terms of used materials;
- thickness of each plane;
- number of planes to displace along the beam line.

Common to all four geometries is the size of each plane surface and the distance between the planes, that at the present is fixed at 2 cm. According to the 10° opening angle of the fragmented ions with $Z > 2$, the surface value has been fixed at $9 \times 9 \text{ cm}^2$.

From the point of view of the choice of **materials** and plane **thickness**, it has been already introduced in Chapter 2 that one configuration foresees the use of a single $150 \mu\text{m}$ thick Silicon layers for each plane, while the other solution exploits two Silicon layers thinned down to $50 \div 70 \mu\text{m}$ each one, glued together using

a 30 μm thick bi-adhesive kapton¹foil. The two layers of this last configuration are orthogonally disposed: one layer has the strips oriented along x direction, the other one has the strips disposed following y direction, while the incoming particles are along the z direction.

For what concerns the **number of planes**, for each solution above described, it has been investigated the possibility of adopting 3 or 4 planes, uniformly spaced along the beam line. On one hand, the addition of a fourth plane guarantees a better track reconstruction and dE/dx measurement accuracy, but, on the other hand, it increases the probability of secondary fragmentations caused by the detector itself as well as multiple scattering effects.

The choice of the **strip pitch** is a compromise between the physics requirements and the maximum number of allowed readout channels. At present a strip pitch of 125 μm has been chosen for all four configurations. With this choice, the maximum number of strips in 9 cm is 720 and each x-y plane have therefore 2x720 channels. Considering 3 planes, $3 \times 2 \times 720 = 4320$ electronic readout channels are needed. Finally, concerning the adoption of the LGAD amplification mechanism, already introduced in Chapter 2, this one will be implemented for the configuration that exploits the use of the two Silicon layers, because of the smaller signal produced with respect to the case in which only one thicker Si layer is adopted. In this case, dead spaces have been taken into account adding Silicon inactive regions in the configuration geometry, as schematically shown in Fig.4.2.

For a better understanding, the characteristics of each layout are resumed in Tab.4.1 and a schematic representation is shown in Fig.4.1. Note that all configurations are named "V13", due simply to the fact that the current version of the simulated FOOT experimental setup is the number 13. The first number right after the point indicates the composition of each plane: V13.0 indicates the layout that foresees the presence of a kapton foil between the two Si layers, whereas V13.1 is the version in which one single Si layer is used. The second identification number has been introduced to give information on the number of planes: V13.0.0, as well as V13.1.0, are those configurations characterized by 3 planes, while versions V13.0.1 and V13.1.1 foresee the addition of the fourth plane.

Once the different geometries have been fixed, the simulated data of the different versions are provided by means of the FLUKA Monte Carlo tool. The details of simulations and the obtained results are listed in the following Sections.

Table 4.1: Possible configurations and geometrical data for the MSD analysis.

| Versions | V13.0.0 | V13.0.1 | V13.1.0 | V13.1.1 |
|---|---------|---------|---------|---------|
| No. planes | 3 | 4 | 3 | 4 |
| No. layers | 2 | 2 | 1 | 1 |
| Plane thickness [μm] | 130 | 130 | 150 | 150 |
| Kapton foil | Y | Y | N | N |
| Strip pitch [μm] | 125 | 125 | 125 | 125 |
| LGAD | Y | Y | N | N |

4.2 Energy loss analysis

The aim of this analysis is to evaluate the strip detector particle identification performance by means of the particle energy deposition. The simulations are

¹Kapton is a compound of Hydrogen, Nitrogen, Carbon and Oxygen(Mass composition: H=2.636%, N=7.327%,C=69.113% O=20.924%.)

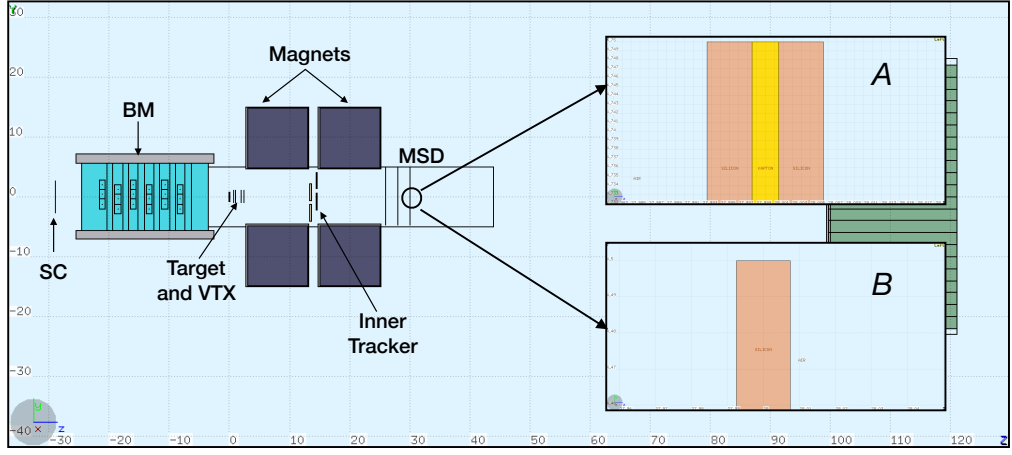


Figure 4.1: Schematic representation of two possible configurations of the MSD planes. A: versions V13.0.0, where two Si layers are glued together with a Kapton foil (the yellow thickness in the picture) are used. B: versions V13.1.0 with a single Si layer [FLAIR geoviewer].

performed with two different values of the beam energy and for different ion species, from the Lithium up to the Oxygen, as resumed in Tab.4.2. The beam source is placed right in front of the detector, at a few mm from the surface of the first plane (Fig.4.2). Note that for the V13.0.0 and the V13.0.1 simulations, since the adoption of a LGAD amplification mechanism leads to the presence of dead spaces, the beam source position has been shifted at (0.8 cm, 0.8 cm), in order to avoid the Silicon inactive regions. The beam has been considered as a forward directed ($z > 0$) pencil beam with FWHM=0.

Table 4.2: Beam properties for the performed simulations. The simulations have been carried out for different type of particles: ^{16}O , ^{14}N , ^{12}C , ^{10}B , ^9Be , ^7Li .

| Configurations | Beam energy [MeV/u] | Beam position (x,y,z) [cm] | Beam Direction | No. Primary Particles |
|-------------------|---------------------|----------------------------|----------------|-----------------------|
| V13.0.0 - V13.0.1 | 200-700 | (0.8,0.8,25) | $z > 0$ | 20,000 |
| V13.1.0 - V13.1.1 | 200-700 | (0,0,25) | $z > 0$ | 20,000 |

As already discussed in the first Chapter, the energy loss in thin materials follows the Landau distribution. In Fig.4.3 the energy distributions for different particles at 200 MeV/u and 700 MeV/u are shown. It is clearly visible the typical asymmetric behavior of such distribution with a tail for high energy depositions. Furthermore, it can be noticed that the distributions are partially superimposed. The overlapping probability determines the detector particle identification inaccuracy. Such probability has been evaluated as the overlapping area individuated when comparing the different energy distributions of each ion species, as shown in Fig.4.3.

For a beam energy of 200 MeV/u the misidentification probability for the Lithium is $\approx 11\%$, as shown in Fig.4.3, while reaches $\approx 18\%$ for the Oxygen ion. When the beam energy is 700 MeV/u, the overlap among adjacent ions is increased up to $\approx 30\%$ for Nitrogen and Oxygen ions. In this case, the use of the LGAD device would help in a better separation of ion species and this will be fundamental to measure the dE/dx for the energies of interest in the astrophysical sector (100 MeV/u - 1 GeV/u). These results are related to the versions V13.0.0

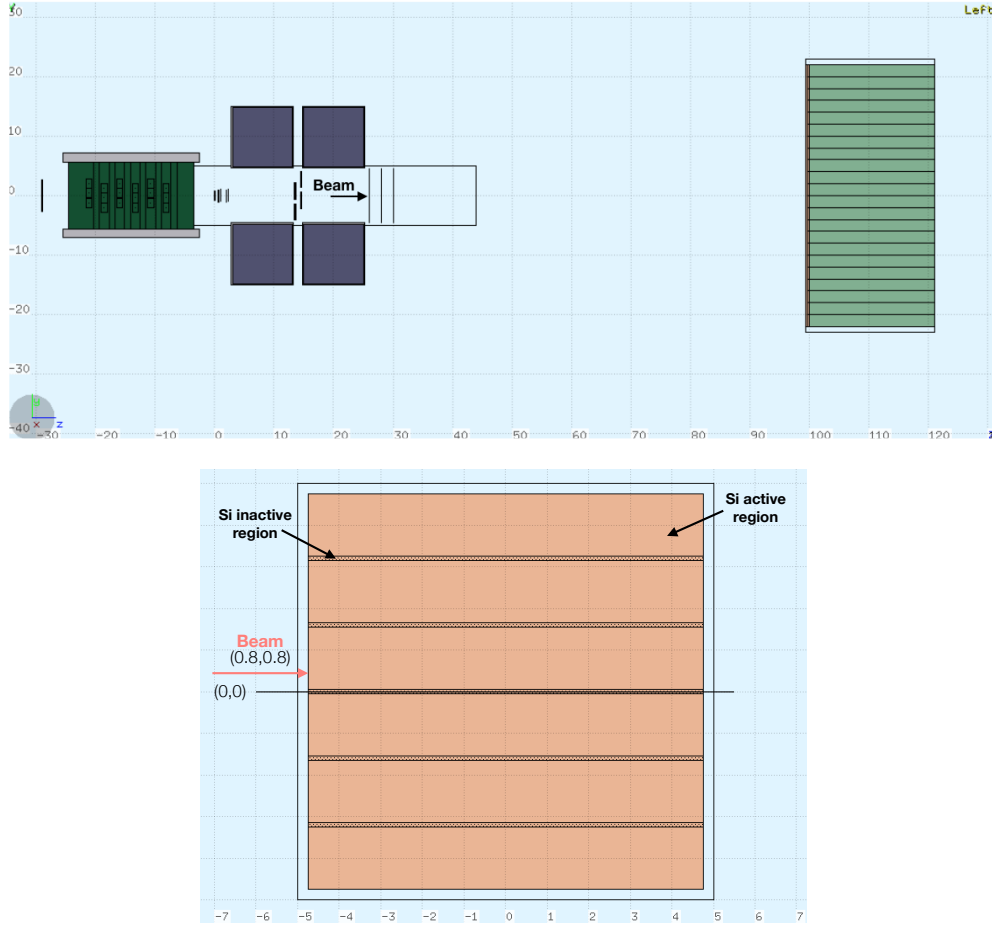


Figure 4.2: Beam position for MC simulations. On the left: a y-z view of the overall FOOT experimental setup. On the right: a x-y view of the Si planes of versions V13.0: the presence of dead spaces (thinner layers in the Figure) leads to the necessity of displacing the beam in a different position with respect to the origin of the coordinate system [FLAIR geoviewer].

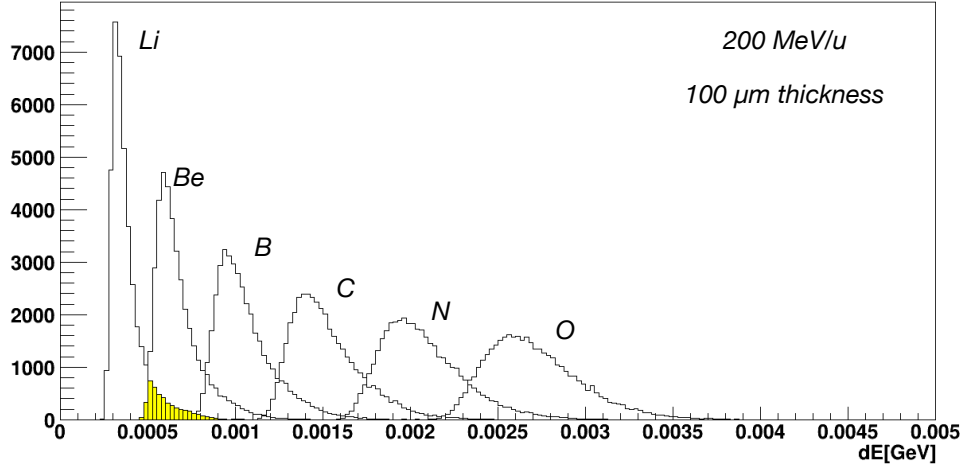
and V13.0.1, averaging the deposited energy on the two Silicon layers, with a resulting Silicon thickness of $100 \mu\text{m}$.

The simulation results show that the particle identification is not so precise. However, since the dE/dx measurement is mainly given by the scintillator, the obtained misidentification probabilities are acceptable for this component, confirming that a strip detector can contribute to the redundant dE/dx measurement of single ions.

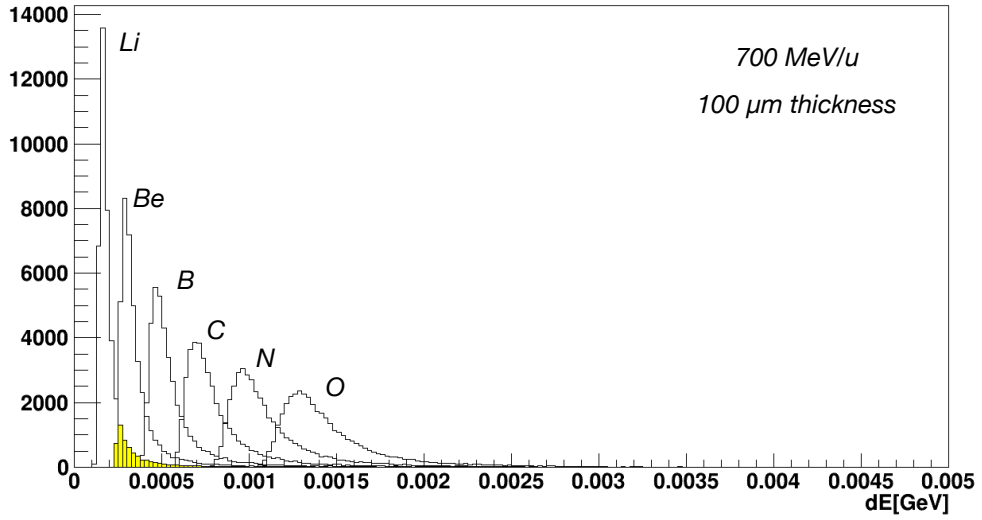
A further proof of the positive contribution of the Silicon detector in dE/dx measurements comes from the analysis of the energy loss in the Scintillator Detector (SCN) when coupled with the microstrip detector. To perform this study each particle has been followed, from the entrance in the MSD to the exit from the Scintillator, evaluating the average energy deposition as follows:

- evaluation of the average energy deposition in the whole MSD, dE_{MSD} ;
- evaluation of the average energy deposition in the two layers of Scintillator Detector, dE_{SCN} ;
- definition of a new variable that accounts for the coupling of the two detectors and that is given by the sum of the energy deposition in both the MSD and the SCN: $dE_{MSD/SCN}$

The goal is verify that with the coupling of the two detectors, the energy loss measurement in the scintillator gains in terms of resolution. In order to perform



(a)



(b)

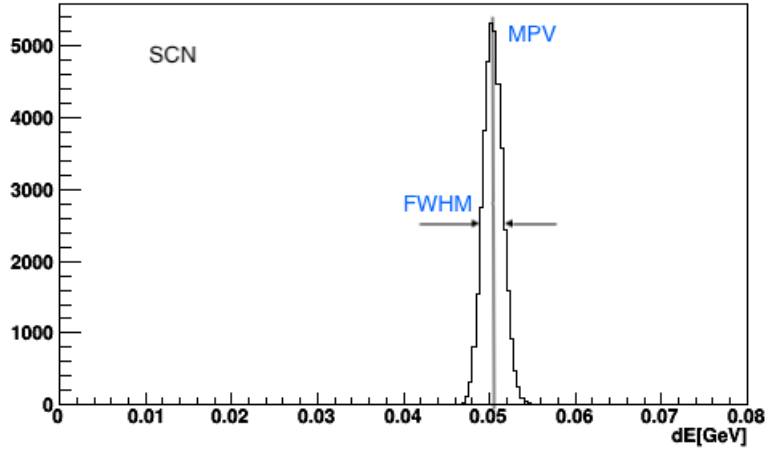
Figure 4.3: Energy deposition from different particles (^{16}O , ^{14}N , ^{12}C , ^{10}B , ^9Be , ^7Li) at 200 MeV/u (a) and 700 MeV/u (b). Lithium misidentification is highlighted in yellow.

the study, the two energy deposition dE_{SCN} and $dE_{MSD/SCN}$ are compared, as shown in Fig.4.4. The energy resolution is defined as the ratio between the Full Width at Half Maximum (FWHM) and the Most Probable Value (MPV) of the considered energy distribution:

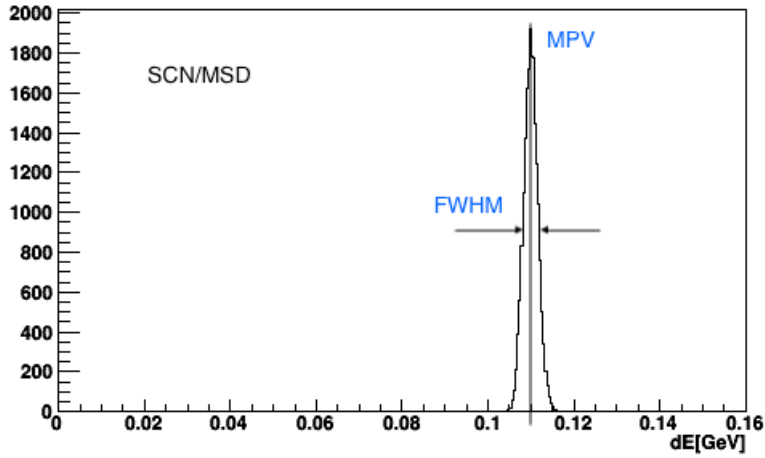
$$Resolution = \frac{FWHM}{MPV} \quad (4.1)$$

The obtained results are summarized in Tab.4.3. Looking at the Tab.4.3, it is immediately noticeable a gain in the energy loss measurement resolution when the scintillator is coupled with the microstrip detector, proving that the use of such type of detector can contribute to the energy loss measurements improving the reliability of the whole experimental setup.

If on one hand the presence of the MSD detector positively contributes to energy loss measurements, on the other hand, it increases the multiple scattering and the fragmentation effects due to the detector itself.



(a)



(b)

Figure 4.4: A simulated energy loss distribution of ^{12}C ion beam at 200 MeV/u in the Scintillator (SCN) and coupling with Microstrip Silicon Detector (SCN/MSD). The Most Probable Value (MPV) and the Full Width at Half Maximum (FWHM) are highlighted.

Table 4.3: Comparison in terms of resolution (last two columns) when the scintillator is coupled with the microstrip silicon detector. The data refer to different ion beams at 200 MeV/u for version V13.0.0. Similar results have been obtained for the other configuration under the same simulation conditions.

| Beam Particle | MPV SCN [MeV] | FWHM SCN [MeV] | MPV MSD/SCN [MeV] | FWHM MSD/SCN [MeV] | Res SCN | Res MSD/SCN |
|-----------------|---------------|----------------|-------------------|--------------------|----------|-------------|
| ^{16}O | 90.5 | 3 | 197.2 | 3 | 3.31E-02 | 1.52E-02 |
| ^{14}N | 68.7 | 3 | 150.5 | 3 | 4.36E-02 | 1.99E-02 |
| ^{12}C | 50.2 | 2.4 | 110 | 3.2 | 4.78E-02 | 2.91E-02 |
| ^{10}B | 34.6 | 2.1 | 76.4 | 2.4 | 6.06E-02 | 3.14E-02 |
| ^9Be | 22.1 | 1.5 | 48.4 | 1.6 | 6.78E-02 | 3.31E-02 |
| ^7Li | 12.3 | 1 | 27.3 | 1.8 | 8.13E-02 | 6.59E-02 |

4.3 Multiple Scattering analysis

In this Section the effect of multiple scattering on track reconstruction and on momentum measurements is introduced, showing then some relevant obtained results. Consider a particle of momentum p passing through a region of length L , with an applied uniform magnetic field B , whose direction is perpendicular to

the particle motion (Fig.4.5). The deviation from a straight line s is known as the *sagitta* of the track.

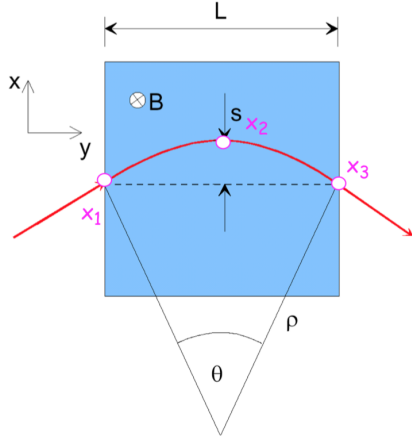


Figure 4.5: [56]

Given a small curvature angle θ , the sagitta s is given by:

$$s = \rho \left(1 - \cos \frac{\theta}{2} \right) \approx \rho \frac{\theta^2}{8} \quad (4.2)$$

where ρ is the curvature radius. Since $\theta \approx \frac{L}{\rho}$, the sagitta can be written as:

$$s \approx \frac{L^2}{8\rho} \quad (4.3)$$

A charged particle moving in a magnetic field experiences the Lorentz Force, given by:

$$F = ev \times B \quad (4.4)$$

where v is the particle velocity. Because B and v lie in perpendicular directions, this force will cause the particles to travel in circular trajectories. Hence, they are also subjected to the centripetal force:

$$m \frac{v^2}{\rho} = Bev \Rightarrow mv = Be\rho \quad (4.5)$$

Since $mv=p$, Eq.(4.5) becomes:

$$p = Be\rho \quad (4.6)$$

the unit of e is Coulomb (C), the magnetic field B is in Tesla (T) and ρ is in meters. Multiply both sides by the speed of light $c = 3 \times 10^8$ m/s. Then the units are in Joule (J). Since $1 \text{ eV} = 1.6 \times 10^{-19}$ J, Eq.(4.6) can be expressed as:

$$pc = \frac{Be\rho c}{1.6 \times 10^{-19}} [\text{eV}] \quad (4.7)$$

Since $e = 1.6 \times 10^{-19}$ C, the equation above reduces to:

$$pc = B\rho c [\text{eV}] \quad (4.8)$$

By substituting on the right hand side the value of c , the equation becomes:

$$pc = 3 \times 10^8 B\rho [\text{eV}] \quad (4.9)$$

Now, expressing the units in terms of c and considering that $1 \text{ GeV} = 10^9 \text{ eV}$:

$$p = 0.3B\rho [\text{GeV}/c] \quad (4.10)$$

The curvature radius thus depends on the magnetic field and on the momentum as follows:

$$\rho [\text{m}] = \frac{p [\text{GeV}/c]}{0.3B [\text{T}]} \quad (4.11)$$

Consider now the case of 3 measurements x_1, x_2, x_3 , as shown in Fig.4.5, obtained by means of three different detectors. In this case the measured sagitta and the associated error will be:

$$s = x_2 - \frac{x_1 + x_3}{2} \quad (4.12)$$

$$\delta s = \sqrt{\frac{3}{2}} \delta x \approx \delta x \quad (4.13)$$

where δx is the uncorrelated error associated to a single x measurement. The error on the sagitta measurement depends also on the traversed length L and on the error of the curvature radius:

$$|\delta s| = \frac{L^2}{8\rho} \frac{\delta\rho}{\rho} \approx \delta x \quad (4.14)$$

where $\delta\rho/\rho$ is the *curvature*. Since for a particle moving in a plane perpendicular to a uniform magnetic field, the momentum and the curvature radius are related as shown in Eq.(4.11), it can be derived that:

$$\frac{\delta p}{p} = \frac{\delta\rho}{\rho} \quad (4.15)$$

Deriving the expression of the curvature from Eq.(4.14) and substituting in Eq.(4.15) together with Eq.(4.11), the momentum resolution will be then given by:

$$\frac{\delta p}{p} = \frac{8\rho}{L^2} \delta x = \frac{8p}{0.3BL^2} \delta x \Rightarrow \frac{\delta p}{p^2} = \frac{8}{0.3BL^2} \delta x \quad (4.16)$$

Some important features can be derived:

- the percentage error on the momentum is proportional to the momentum itself;
- the error on the momentum is proportional to the coordinate measurement error δx ;
- the error on the momentum is inversely proportional to the applied magnetic field B ;
- the error on the momentum is inversely proportional to the traveled length L^2 ;

A good momentum resolution calls thus for a long track. Any trick that can extend the track length can produce significant improvements on the momentum resolution. On the other hand, particles moving through the detector material suffer plastic Coulomb scatterings which may alter the original particle trajectories. From this point of view, an additional layer of material could cause the particle to deviate significantly from the original direction, affecting track reconstruction and the momentum measurement itself. The optimal choice is the configuration that allows a precise track reconstruction with reducing as much as possible the loss in momentum resolution. It is therefore important to introduce an expression that shows how the momentum resolution is related with the deflection angle.

Consider 3 equidistant thin detectors, as shown in Fig.4.6 and suppose that the particle motion is largely dominated by multiple scattering. The error on coordinate measurement due to the multiple scattering is given by:

$$\delta x \approx \frac{L}{k} \delta\theta$$

where k is the number of detectors. The momentum resolution is thus given by [56]:

$$\frac{\delta p}{p^2} = \frac{\delta x}{0.3BL^2} \sqrt{4A_k} = \frac{\delta\theta}{k} \frac{1}{0.3BL} \sqrt{4A_k} \quad (4.17)$$

where A_k , for a quadratic fit, is equal to:

$$A_k = \frac{3(3k^2 + 6k - 4)}{4(k-1)(k+1)(k+3)}$$

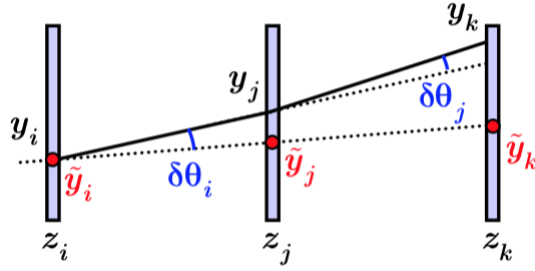


Figure 4.6: Effect of multiple scattering on track reconstruction for a particle moving through 3 thin detector layers: z_i, z_j, z_k are the measuring detectors z coordinates, while y_i, y_j, y_k are the y coordinates of the measurements [56].

The momentum resolution therefore worsens with increasing scattering angles $\delta\theta$ and improves as $1/L$, also the additional factor $1/k$ can help.

A series of simulations have been performed for all the experimental setup configurations previously presented in Tab.4.2. The scattering angle has been calculated for a single plane and without the action of the magnetic field, in order to obtain an evaluation of the deflection angle as a function of the traversed thickness only. Furthermore, to demonstrate the reliability of the results obtained from the simulations, the values have been then compared with the expression of the scattering angle derived by Molière theory, as presented in Chapter 1:

$$\sigma_\theta [\text{rad}] = \frac{13.6 \text{ MeV}}{\beta c p} Z_p \sqrt{\frac{d}{L_{\text{rad}}}} \left[1 + 0.038 \ln \left(\frac{d}{L_{\text{rad}}} \right) \right] \quad (4.18)$$

where, in our case, $d=0.015$ cm and L_{rad} for the Silicon is equal to 9.37 cm. Since the particles enter in the MSD at different angles, the total path length is greater than the plane thickness. However, at a first stage, assuming d equal to the thickness value is an acceptable approximation. Finally, the projected angle θ_{plane} and the corresponding displacement in the direction transversal to the beam axis y_{plane} (Fig.4.7) have been evaluated by means of a simulation with different ion beams at 200 MeV/u. On Tab.4.4 and Tab.4.5, the obtained values for version V13.1 (single Si layer) are resumed. Similar conclusions have been obtained for the configuration with the kapton foil.

Table 4.4: Scattering quantities for different ion species at 200 MeV/u, traversing 150 μm of Silicon: p is the average particle momentum, $\beta = v/c$, z is the particle charge, θ_{Ref} is the angle value derived from Molière theory while θ_{sim} is the angle obtained from simulation.

| V13.1 - 150 μm | | | | | |
|---------------------------|-------------|---------|-----|-----------------------------|-----------------------------|
| Beam Particle | p [GeV/u] | β | z | θ_{Ref} [deg] | θ_{sim} [deg] |
| ^{16}O | 10.27 | 0.5676 | 8 | 0.0321 | 0.0293 \pm 0.00015 |
| ^{14}N | 8.99 | 0.5677 | 7 | 0.0322 | 0.0295 \pm 0.00016 |
| ^{12}C | 7.71 | 0.5679 | 6 | 0.0322 | 0.0292 \pm 0.00015 |
| ^{10}B | 6.43 | 0.5678 | 5 | 0.0322 | 0.0291 \pm 0.00016 |
| ^9Be | 5.78 | 0.5677 | 4 | 0.0286 | 0.0260 \pm 0.00015 |
| ^7Li | 4.51 | 0.5677 | 3 | 0.0276 | 0.0245 \pm 0.00014 |
| ^4He | 1.24 | 0.3151 | 2 | 0.120 | 0.1076 \pm 0.00058 |

Looking at the results, one can firstly notice that, taking into account the associated relative errors for both θ_{Ref} and θ_{sim} , values coming from simulations

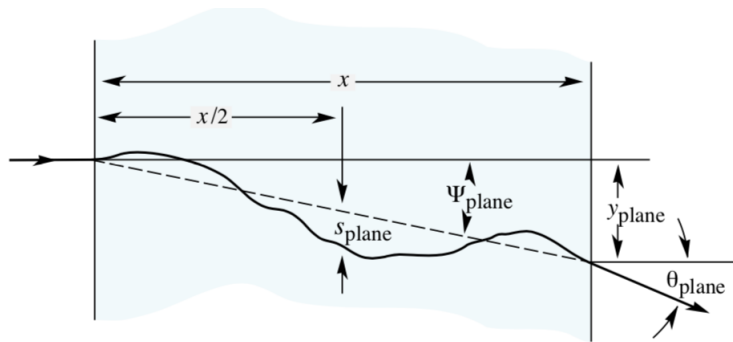


Figure 4.7: Representation of main scattering quantities [25].

Table 4.5: Scattering quantities for different ion species at 200 MeV/u, traversing 150 μm of Silicon: θ_{plane} is the scattering angle on the y-z plane and y_{plane} is the difference between the final particle position and the initial position measured along y direction.

| V13.1 - 150 μm | | |
|---------------------------|------------------------|-------------------------------|
| Beam Particle | θ_{plane} [deg] | y_{plane} [μm] |
| ^{16}O | 0.0201 ± 0.00014 | 0.0670 ± 0.00047 |
| ^{14}N | 0.0204 ± 0.00014 | 0.0673 ± 0.00048 |
| ^{12}C | 0.0213 ± 0.00015 | 0.0667 ± 0.00047 |
| ^{10}B | 0.0214 ± 0.00015 | 0.0681 ± 0.00048 |
| ^9Be | 0.0215 ± 0.00015 | 0.0641 ± 0.00045 |
| ^7Li | 0.0205 ± 0.00014 | 0.0582 ± 0.0004 |
| ^4He | 0.0826 ± 0.00058 | 0.2362 ± 0.0016 |

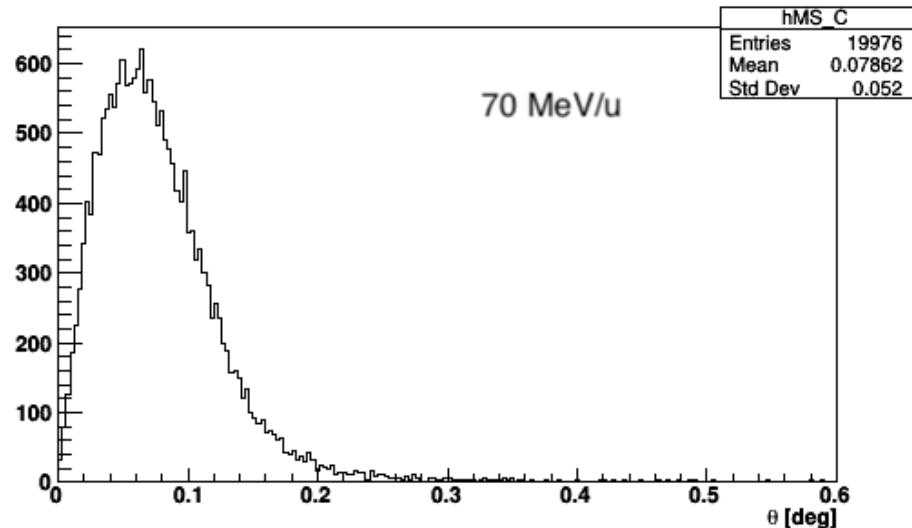
approach the values of the scattering angle calculated with Eq.(4.18), proving the reliability of the performed simulations.

To underline the dependence of the multiple scattering on the particle energy, in Fig.4.8 scattering angle distributions obtained for two different beam energies are shown. It is noticeable that for increasing energy of the incident particle, the scattering angle diminishes, according to the $1/E$ dependence of the angle introduced with the term β in the denominator of Eq.(4.18).

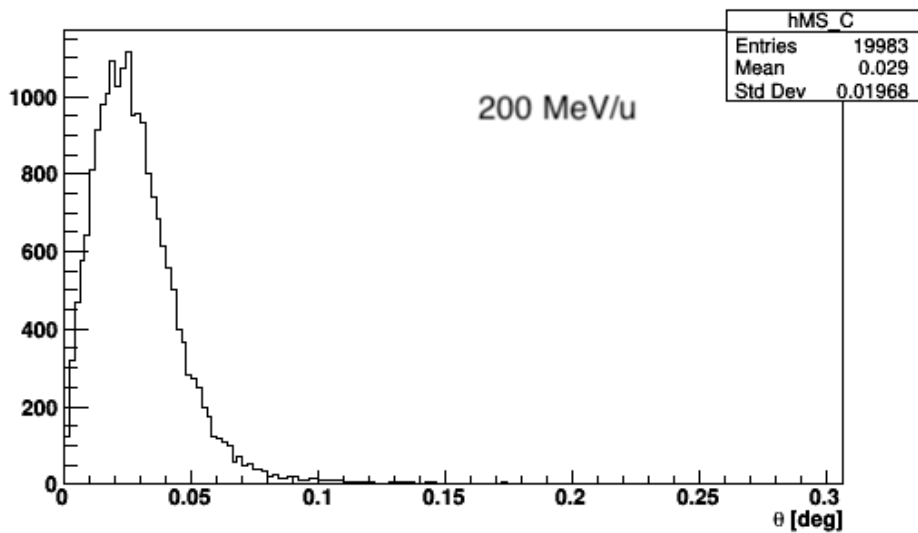
To study the influence of the addition of a fourth plane, it has been also evaluated the total scattering angle, from the entrance of the particle in the first plane of the MSD, to the exit from the last plane. On Tab.4.6 scattering angles obtained from simulations for different ion species at 200 MeV/u are resumed. Overall, it is clearly noticeable that, as expected, for increasing values of the traversed thickness, the scattering angle increases. However, the 20 μm added to each plane of configurations V13.1 (single Si plane), cause just $\approx 1\%$ of increase in the scattering angles, with respect to versions V13.0. The presence of a fourth plane does not sensitively affect the scattering angle with respect to the case in which three planes are used: for configuration V13.0 (first two columns of Tab.4.6) the presence of a fourth plane increases the effect of multiple scattering of $\approx 0.83\%$, while for the other configuration (last two columns on Tab.4.1) the phenomenon is increased of $\approx 1\%$.

4.4 Fragmentation analysis

As discussed in the previous Section, the increase in the number of planes in a tracker detector (Fig.4.6) positively contribute to the momentum resolution. However, if on one hand the addition of a fourth plane does not significantly affect



(a)



(b)

Figure 4.8: Scattering angle distributions for a ^{12}C ion beam at 70 MeV/u (a) and 200 MeV/u (b).

multiple scattering phenomena, on the other hand, it could lead to a rise in secondary fragmentation events. Since it is fundamental to match the reconstructed tracks with the hits in the scintillator and the calorimeter, fragmentations occurring in particular in the last plane must be reduced as much as possible. Looking at Fig.4.9 one can see in fact that, if a fragmentation occurs in the first planes, it is possible to individuate possible fragments by using the information coming from the hit in the following plane. When fragmentations occur in the last plane it becomes difficult to follow secondary particles produced.

The addition of a fourth plane, that will ensure a better track reconstruction and an increased momentum resolution, must not cause a considerably increase of secondary fragmentations. For this purpose the fragmentation probability has been evaluated for single plane, counting the number of fragmentation events per incident particle. New simulations has been implemented, increasing the number of primary particles up to 500000, because of the expected low value of the occurrence probability for this kind of events. Simulations has been carried

Table 4.6: Scattering angles for different ion species at 200 MeV/u traversing the whole detector. Results are shown for the four different configurations of the Microstrip Detector. The thickness of a single plane (l) and the total traveled distance (L) are highlighted.

| Scattering Angle [deg] | | | | |
|------------------------|--|--|--|--|
| Beam Particle | 3 planes l=0.013[cm] L=4.013[cm] | 4 planes l=0.013[cm] L=6.013[cm] | 3 planes l=0.015[cm] L=4.015[cm] | 4 planes l=0.015[cm] L=6.015[cm] |
| ^{16}O | $0.05 \pm 1.77E-06$ | $0.056 \pm 1.91E-06$ | $0.058 \pm 1.96E-06$ | $0.065 \pm 2.19E-06$ |
| ^{14}N | $0.049 \pm 1.76E-06$ | $0.056 \pm 1.89E-06$ | $0.058 \pm 2.9E-06$ | $0.065 \pm 2.22E-06$ |
| ^{12}C | $0.049 \pm 1.7E-06$ | $0.056 \pm 1.95E-06$ | $0.057 \pm 1.97E-06$ | $0.065 \pm 2.23E-06$ |
| ^{10}B | $0.049 \pm 1.71E-06$ | $0.055 \pm 1.92E-06$ | $0.057 \pm 2.01E-06$ | $0.064 \pm 2.21E-06$ |
| 9Be | $0.043 \pm 1.57E-06$ | $0.049 \pm 1.73E-06$ | $0.051 \pm 1.81E-06$ | $0.057 \pm 1.98E-06$ |
| 7Li | $0.041 \pm 1.47E-06$ | $0.046 \pm 1.61E-06$ | $0.049 \pm 1.73E-06$ | $0.055 \pm 1.95E-06$ |
| 4He | $0.183 \pm 6.48E-06$ | $0.204 \pm 6.96E-06$ | $0.212 \pm 7.25E-06$ | $0.24 \pm 8.12E-06$ |

out for different ion species, from 4He up to ^{16}O at 200 MeV/u, placing again the beam in front of the MSD. The results obtained for the configuration V13.0 are shown in Tab.4.7. Similar results have been obtained for version V13.1.

Observing the results, the mean fragmentation probability seems not to be so likely to occur, so the presence of a fourth plane do not significantly contribute to the increase of such phenomenon.

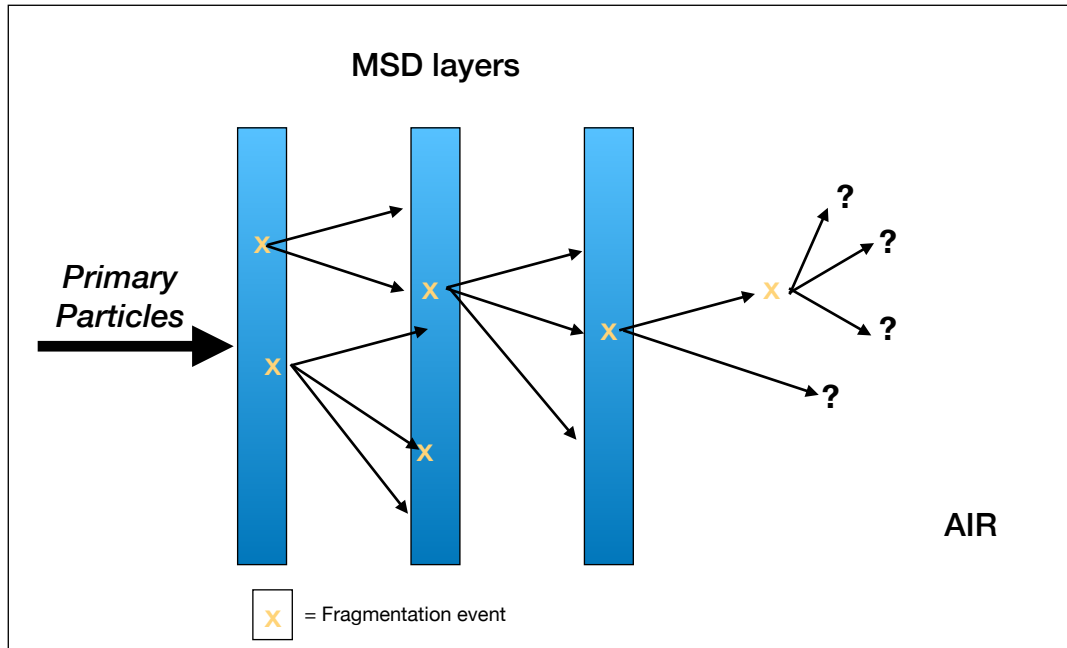


Figure 4.9: Schematic representation of fragmentation events through MSD layers. Secondary fragmentations on last plane negatively affect matching with hits in the Scintillator.

Considering the configuration that foresees two Si layers, it is useful to observe the contribute of the Kapton foil in fragmentation events. Thanks to the reconstruction software, it is possible to find the production region of the fragments, as shown in Fig.4.10. Each region, defined by means of the combinatorial geometry of the FLUKA software, is identified with a number. In this way, once the number of the region of interest is known, it is possible provide all the needed information that are relevant for the performed analysis.

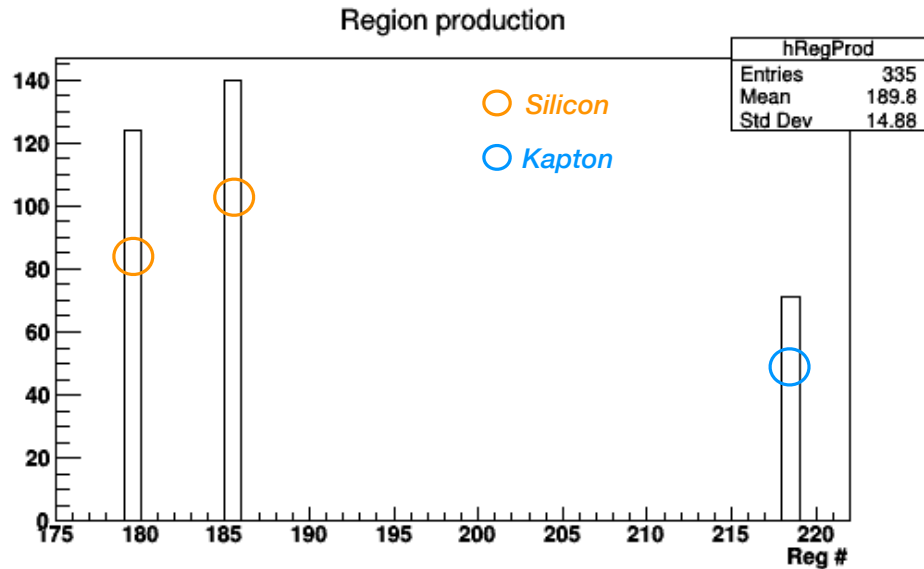


Figure 4.10: Example of the production region identification of produced fragments for configuration V13.0. The distinction between fragmentations occurring in Silicon regions (orange) and in the Kapton foil (blue) is highlighted.

Table 4.7: Fragmentation probability per incident particle for different ion species at 200 MeV/u in a single plane of microstrip detector. The thickness value of a single plane is shown on the top rule.

| V13.0.0 - 130 μm | |
|-----------------------------|---------------------------|
| Beam Particle | Fragmentation Probability |
| ^{16}O | 0.074% |
| ^{14}N | 0.072% |
| ^{12}C | 0.076% |
| ^{10}B | 0.067% |
| ^9Be | 0.063% |
| ^7Li | 0.047% |
| ^4He | 0.015% |

In Tab.4.8 the percentage of fragmentation events occurring in the kapton foil for each particle type is shown. Overall, less than 1/4 of fragmentations take place in the kapton foil. However, this is another important aspect that must be taken into account in the choice of the definitive layout.

Table 4.8: Fragmentation probability in 30 μm thick kapton foil for different ion species at 200 MeV/u.

| Kapton foil - 30 μm | |
|--------------------------------|------------------------|
| Beam Particle | Fragmentation $_{kap}$ |
| ^{16}O | 16% |
| ^{14}N | 11% |
| ^{12}C | 24% |
| ^{10}B | 21% |
| ^9Be | 29% |
| ^7Li | 23% |
| ^4He | 23% |

Conclusions

Heavy charged particle therapy has already evolved from physics research laboratories to clinical practice. There is clear evidence from physics that dose distributions from particles are more favorable compared to photon or electron treatments. Some of the uncertainties in the Charged Particle Therapy are directly related to the lack of knowledge in particle interactions with tissues, e.g. nuclear interaction cross sections at therapeutic energies. In this sense, the FOOT (FragmentatiON Of Target) experiment has been conceived to perform a series of measurements of target nuclear fragmentation cross sections for protons and projectile nuclear fragmentation cross sections for heavy ions. These data will be useful for the development of a new generation of Treatment Planning Systems (TPS).

This thesis is performed in the framework of the design study of the FOOT experimental setup, with a particular attention to aspects concerning the Microstrip Silicon Detector (MSD). The main purpose of such detector is the tracking of fragments downstream the magnetic volumes, that is essential for the momentum measurement and it is also fundamental to match the reconstructed tracks with the hits in the scintillator and the calorimeter. The work described in this thesis aims at giving some preliminary results on the strip detector performances, allowing to optimize its design and to find the optimal configuration that satisfies the requirements of the experiment. At the present there are not enough available experimental data for this detector and to study its properties various simulations have been performed by means of the FLUKA Monte Carlo code. The first stage of the analysis aimed to prove that the MSD positively contributes to the energy loss measurements. Indeed, the analysis shown that ion identification is possible with less than 20% confusion for beam energies of 200 MeV/u. Increasing the beam energy up to 700 MeV/u, that is of interest in the astrophysical sector, the overlap among adjacent ions reaches a percentage of the order of 30%. However, the use of the Low Gain Amplification Diode (LGAD) mechanism, that can be adopted for this detector, would help in separating ion species and in recovering at least partially the small overlapping area obtainable with lower energies. A clear proof of the MSD contribution in the energy loss measurement comes from the analysis of the coupling with the scintillator detector, that shown a gain in resolution when comparing energy losses in the scintillator and the energy distributions obtained when this detector is coupled with the MSD. The successive phase of the analysis has been devoted to study the effects of the multiple scattering and of the secondary fragmentations through the detector thickness, in order to investigate the possibility of adding a further Silicon layer to the MSD. The original configuration foresees the use of three planes, the benefit of adding a fourth plane is dictated by the necessity of improving track reconstruction and therefore the performances of the whole experimental setup. For what concerns the multiple scattering, the obtained results shown that the addition of a further plane does not considerably affect the particle trajectory, since the comparison of the evaluated scattering angles between the different configurations did not show substantial differences. Secondary fragmentations has shown not to be so likely to occur, the fragmentation probability for each single plane of the detector is

lower than 0.08% for all the considered ion species. Both the two stages of the study has been carried out for two different MSD layers configurations, one of which foresees the use of two Silicon (Si) layers for each plane. Such layers are orthogonal to each other and are glued together by means of a Kapton foil. This solution, with respect to that one that foresees one single Si layer, is characterized by the presence of Si inactive regions. Even if the analysis showed no considerable differences between the two solutions, the presence of these inactive regions leads therefore to prefer the configuration for which one single Si layer is foreseen. On December 2017, a test beam has been carried out in the Trento Proton Therapy Centre. The experimental devices used for such test included a model of Silicon strip detector. Although the used Si detector presents different characteristics with respect to the configurations foreseen for the FOOT setup, it has been useful to observe its performances. It has been in particular shown that the detector is able to reconstruct both X and Y coordinates of the beam, allowing a precise beam profile reconstruction.

The preliminary results achieved in this thesis support the possibility of introducing an additional plane to the detector and prove moreover its capability of identifying different ion species through the energy deposited in it. However, comparison with experimental data it is necessary, in order to confirm the reliability of the obtained results.

Bibliography

- [1] Faiz M. Khan, *The Physics of Radiation Therapy*, Third Edition, University of Minnesota Medical School, ISBN 0.7817-3065-1, 2003.
- [2] Daniel Cussol, *Nuclear Physics and Hadrontherapy*, LPC Caen, ENSICAEN, Université de Caen Basse-Normandie, IN2P3/CNRS.
- [3] F. Azaiez, A. Bracco, J. Dobes, A. Jokinen, G. E. Korner, A. Maj, A. Murphy, P. Van Duppen, *Nuclear Physics for Medicine*, Nuclear Physics European Collaboration Committee, ISBN 978-2-36873-008-9.
- [4] U. Amaldi, *Hadrontherapy in the world*, University of Milano Bicocca and TERA Foundation, Italy.
- [5] S. N. Ahmed, *Physics and Engineering of Radiation Detection*, First Edition, Elsevier, 2007.
- [6] O.Jakel, *Radiotherapy with protons and ion beams*, AIP Conference Proceedings, 1231(1), pp 3-40, 2010.
- [7] M. Durante and H. Paganetti, *Nuclear physics in particle therapy: a review*, Rep. Prog. Phys., vol. 79, no. 9, p. 096702, 2016.
- [8] H. Paganetti and T. Bortfeld, *Proton Beam Radiotherapy - The State of the Art*, New Tech. in Rad. Onc., ISBN 3-540-00321-5, 2005.
- [9] “www.shi.co.jp/quantum/eng/product/proton/proton.”
- [10] Michael G. Stabin, *Radiation protection and Dosimetry. An Introduction to Health Physics*, Springer.
- [11] L. Yi-Bao and W. Ling, *Radiation Interactions with Matter*, School of Nuclear Engineering and Technology, China.
- [12] Glenn F. Knoll, *Radiation Detection and Measurement*, Third Edition, Jhon Wiley & Sons, Inc.
- [13] M. Durante and Jay S. Joeffrey, *Charged particle in radiation oncology*, Nat. Rev. Clin. Oncol., vol. 7, pp 37-43, 2010.
- [14] E. B. Podgorsak *et al.*, *Radiation Oncology Physics*, ISBN 92-0-107304-6, IAEA, Vienna, 2005.
- [15] R. R. Wilson, *Radiological Use of fast Protons*, Med. Journal Radiology, 47:487-91, 1946.
- [16] D. Schulz, D. Schardt, T. Elsasser, *Heavy Ion in tumor therapy: Physical and radiobiological benefits*, Reviews of Modern Phys., vol. 82, 2010.
- [17] J. Anthony Seibert and John M. Boone, *X-Ray Imaging Physics for Nuclear Medicine Technologists. Part 2: X-Ray Interactions and Image Formation*, Nucl. Med. Technol., vol. 33, pp 3-18, 2005.

- [18] K. borkenstein, S. Levergrun, P. Peschke, *Modelling and Computer Simulations of Tumor Growth and Tumor Response to Radiotherapy*, Radiat. Res. 162, pp 71-83, 2004.
- [19] P. Sigmund, *Low-Speed Limit of Bhor's Stopping Power Formula*, Phys. Rev. A. 54, 3113, 1996.
- [20] J. De Witt, *Stopping Power Theory*, Phys. 5533, 2011.
- [21] L.E. Porter and H. Lin, *Methods of calculating the Barkas effect correction to Bethe-Bloch stopping power*, Journal of Applied Physics, vol. 67, 6613, 1990.
- [22] A. C. Kraan, *Range verification methods in particle therapy: underlying physics and Monte Carlo modeling*, vol.5, Article 150, 2015.
- [23] Simon Schnake, *Material-mapping with multiple scattering of the CMS Pixel Detector*, University of Hamburg, Germany, 2015.
- [24] L. Urbán, *Simulation of Multiple Coulomb scattering in GEANT4*, KFKI, Budapest, 2002.
- [25] C. Patrignani *et al.*, *Particle Data Group*, Chin. Phys. C, 40, 100001, 2016.
- [26] Lenzi and Thomas, *Development and Study of Different Muon Track Reconstruction Algorithms for the Level-1*, CERN-THESIS-2013-042.
- [27] K. Gunzert-Marx *et al*, *Secondary beam fragments produced by 200 MeV u^{-1} ^{12}C ions in water and their dose contributions in carbon ion radiotherapy*, New J. Phys., 10 075003, 2008.
- [28] J. Dudouet *et al.*, *Double-differential fragmentation cross-section measurements of 95 MeV/u ^{12}C beams on thin targets for hadrontherapy*, Phys. Rev. C, vol.88/89, p. 024606/069904, 2013.
- [29] M.Toppi *et al.*, *Measurements of fragmentation cross section of ^{12}C ions on a thin gold target with the FIRST apparatus*, Phys. Rev. C, vol.93, no.6, p. 064601, 2016.
- [30] L. Zhao, D. Mi, B. Hu, Y. Sun, *A generalized target theory and its applications*, Scientific Reports, 5:14568, 2015.
- [31] H. W. Nias, *An Introduction to Radiobiology*, Second Edition, Wiley, 1998.
- [32] IAEA, *Relative Biological Effectiveness in Ion beam therapy*, ISSN 0074-1914, no. 461, 2008.
- [33] M. Scholz, *The Increased Biological Effectiveness of Heavy Charged Particle Radiation: from Cell Culture Experiments to Biophysical Modelling*, vol. 2, no. 5, pp. 427-436, GSI, Darmstadt, 2003.
- [34] “www.chem.libretexts.org/Exemplars-and-Case-Studies/Case-Studies/Nuclear-Energy-for-Today/Effects-of-Radiation.”
- [35] A. E. Blakely, *Inactivation of human kidney cells by high-energy monoenergetic heavy-ion beams*, Lawrence Berkeley national Laboratory, California, 1979.
- [36] J. Tang *et al.*, *Comparison of radiobiological effective depths in 65MeV modulated proton beams*, Brit. J. Cancer, vol.76, no.2, p. 220, 1997.
- [37] E. L. Alpen, *In Radiation Biophysics*, Second Edition, pp 104–131, Academic Press, 1998.

-
- [38] U. Amaldi and M. Silari, *Hadron accelerators in cancer therapy*, CERN/TIS-RP/97-16/CF, 1997.
- [39] H. Owen *et al.*, *Hadron accelerators for radiotherapy*, CERN-ACC-0056, 2014.
- [40] M. Kramer *et al.*, *Treatment planning for heavy-ion radiotherapy: physical beam model and dose optimization*, Phys. Med. Biol. 45 3299, 2000.
- [41] *FOOT Conceptual Design Report*, 2017.
- [42] L. Greiner *et al.*, *A MAPS based vertex detector for the STAR experiment at RHIC*, Nucl. Instrum. Meth. A, vol. 650, no. 1, pp. 68-72, 2011.
- [43] I. Valin *et al.*, *A reticle size CMOS pixel sensor dedicated to the STAR HFT*, J. Instrum., vol. 7, no. 01, p. C01102, 2012.
- [44] H. Spieler, *Semiconductor Detector Systems*, Phys. Division, Lawrence Berkeley national Laboratory, ISBN 0-19-852784-5, 2005.
- [45] B. Kolbinger, *Simulation of a Silicon-Strip Detector*, HEPHY, Institute of High Energy Physics, 2012.
- [46] M. Krammer, *Silicon Detectors*, HEPHY, Institute of High Energy Physics, Praktikum, 2011.
- [47] C. Lechanoine-Leluc, *The AMS-02 Tracker*, International Cosmic Ray Conference Pune , 9, 299-302, 2005.
- [48] F. Tommasino, *et al.*, *Proton beam characterization in the experimental room of the Trento Proton Therapy facility*, Nuclear Inst. and Methods in Physics Research, A 869, 15-20, 2017.
- [49] “www.tifpa.infn.it/sc-init/med-tech/p-beam-research.”
- [50] A. Ferrari, P. R. Sala, A. Fassò, J. Ranft, *FLUKA: A Multi-Particle Transport Code*, CERN-2005-010, INFN Tc 05/11, SLAC-R-773, 2005.
- [51] G. Battistoni, T.T. Bohlen, F. Cerutti, P.W. Chin, L.S. Esposito, A. Fassò, A. Ferrari, A. Lechner, A. Empl, A. Mairani, A. Mereghetti, P.G. Ortega, J. Ranft, S. Roesler, P.R. Sala, G. Smirnov, V. Vlachoudis, *Overview of the FLUKA code*, Annals of Nuclear Energy, 82:10, 2015.
- [52] J. Rauch and T. Schluter, *GENFIT - a generic Track-Fitting Toolkit*, J. Phys. Conf. Ser., vol. 608, p. 012042, 2015.
- [53] A. C. Kraan, *Range verification methods in particle therapy: underlying physics and Monte Carlo modeling.*, Front. Oncol., 5:150, 2015.
- [54] A. Ferrari , P. R. Sala, R. Guaraldi, F. Padoani, *An improved multiple scattering model for charged particle transport*, Nucl. Instrum. Methods Phys. Res. B 71, 412–26, doi:10.1016/0168- 583X(92)95359- Y, 1992.
- [55] A. Capella, U. Sukhatme, C. I. Tan, J. Tran Thanh Van, *Dual Parton Model*, Phys. Rep., vol. 236, pp. 225-329, 1994.
- [56] F. Ragusa, *An Introduction to Charged Particle Tracking*, Italo-Hellenic School of Physics, 2006.

Ringraziamenti

Ringrazio il mio relatore, il Professor Gianni Coppa, per avermi dato l'opportunità di svolgere il mio lavoro di tesi a Milano. Seppur lontano, la disponibilità che ha sempre mostrato è stata incoraggiante.

Ringrazio in particolar modo il Professor Giuseppe Battistoni che mi ha accolto con entusiasmo nel suo team. Lo ringrazio per la pazienza e la saggezza con cui mi ha guidato in questo importante percorso. Lo ringrazio per la fiducia che ha riposto in me in diverse occasioni, senza la quale non sarei riuscita a superare diversi ostacoli.

Grazie di cuore a Serena, Ilaria, Alessia, Silvia e Mauro che mi hanno sempre fatta sentire parte del team. I momenti passati insieme hanno reso questa esperienza unica. Grazie soprattutto a Yun che mi ha supportato e sopportato nei momenti più critici.

Grazie al mio meraviglioso papà che nel suo silenzio riesce sempre a comunicarmi il suo amore e il suo sostegno. Grazie a te mamma, la mia roccia. Senza te non sarei diventata la ragazza determinata che sono oggi. La forza e la passione con cui affronti la vita sono fonte d'ispirazione per me. Grazie per tutti i sacrifici che avete fatto per farmi arrivare fin qui e per avermi sostenuta in tutte le mie scelte di vita.

Grazie al mio fratellone, il mio punto di riferimento. Grazie perchè riesci sempre a capire quando ho bisogno di te. Grazie perchè oltre ad essere un fratello sei il mio migliore amico. Grazie perchè riesci sempre a darmi la grinta e la serenità per non mollare mai.

Grazie a Fabio, per l'amore che mi dimostra ogni giorno. Sai sempre trovare il modo giusto di starmi accanto. Mi sproni ogni giorno a diventare una persona migliore e a non smettere di pormi obiettivi sempre più ambiziosi e per questo sono grata di averti al mio fianco.

Grazie a Chiara, Cristina, Peppe, Tociò, Agostino, Leo e Luca, compagni universitari e ormai compagni di vita. Non riesco ad immaginare come sarebbe stato questo percorso senza voi. Avete reso ogni singola giornata, ogni singolo esame e ogni singola bevuta unici. Vi amo.

Grazie infine a tutti i miei amici e alla mia famiglia che dalla Sicilia riescono sempre a farmi sentire il loro calore e a tirarmi su nelle giornate più impegnative.